NASA CR-180858
EDR 12815

NONDESTRUCTIVE EVALUATION OF STRUCTURAL CERAMICS BY PHOTOACOUSTIC MICROSCOPY FINAL REPORT

by PRAMOD K. KHANDELWAL

ALLISON GAS TURBINE DIVISION
General Motors Corporation

PREPARED

for

NATIONAL AERONAUTICS
AND
SPACE ADMINISTRATION

NASA

NASA LEWIS RESEARCH CENTER
CONTRACT NAS3-24390

1. Report No.	2. Government Accession No.	3. Recipient's Catalog No.
NASA CR - 180858		

4. Title and Subtitle	5. Report Date
Nondestructive Evaluation of Structural Ceramics by Photoacoustic Microscopy	June, 1987
	6. Performing Organization Code
7. Author(s)	8. Performing Organization Report No.
P. K. Khandelwal	12815
	10. Work Unit No.
9. Performing Organization Name and Address	11. Contract or Grant No.
Allison Gas Turbine Division General Motors Corporation P.O. Box 420 Indianapolis, IN 46206-0420	NAS3-24390
	13. Type of Report and Period Covered
12. Sponsoring Agency Name and Address	Contractor Report
National Aeronautics and Space Administration Lewis Research Center 21000 Brookpark Road, Cleveland, Ohio 44135	14. Sponsoring Agency Code

15. Supplementary Notes

PAM Program Manager: Stanley J. Klima
NASA-Lewis Research Center, Cleveland, Ohio

16. Abstract

Allison Gas Turbine Division of General Motors Corporation has successfully developed and utilized a photoacoustic microscopy (PAM) digital imaging system to characterize silicon nitride material at the various stages of the ceramic fabrication process.

Correlation studies revealed that photoacoustic microscopy detected failure initiating defects in substantially more specimens than microradiography and ultrasonic techniques. Photoacoustic microscopy detected 10 to 100 micro size surface and subsurface pores and inclusions, respectively, up to 80 micron below the interrogating surface in machined sintered silicon nitride. Microradiography detected 50 micron diameter fracture controlling pores and inclusions.

Subsurface holes were detected up to a depth of 570 micron and 1.00 mm in sintered silicon nitride and sintered silicon carbide, respectively. Seeded voids of 20-30 micron diameter at the surface and 50 micron below the interrogating surface were detected by photoacoustic microscopy and microradiography with 1% x-ray thickness sensitivity. Tight surface cracks of 96 micron length X 48 micron depth were detected by photoacoustic microscopy.

PAM volatalized and removed material in the green state which resulted in linear shallow micromacks after sintering. This significantly limits the use of PAM as an in-process NDE technique

17. Key Words (Suggested by Author(s))	18. Distribution Statement
Photoacoustic microscopy, microradiography, silicon nitride, fractography, correlation, imaging	

19. Security Classif. (of this report)	20. Security Classif. (of this page)	21. No. of Pages	22. Price*
Unclassified	Unclassified	105	

* For sale by the National Technical Information Service, Springfield, Virginia 22151

FOREWORD

This is the final technical report of the Nondestructive Evaluation of Structural Ceramics by Photoacoustic Microscopy (PAM) program funded by the NASA-Lewis Research Center, Cleveland, Ohio under contract NAS3-24390. The program manager was Mr. Stanley J. Klima.

The author would like to thank Dr. Peter W. Heitman, Section Chief, Materials Development Laboratory, for his continuous support and encouragement. Thanks are due to Mr. D. L. Vaccari, Supervisor, Ceramic Component Design, for constructive review of this report and valuable suggestions. Special thanks are due to Dr. Jenn Chang who performed the failure and microscopic analysis and Mr. A. Whittemore for conducting all the experiments. The author is also graciously thankful to Mrs. Carolyn Glowner for her assistance in preparing this report.

TABLE OF CONTENTS

LIST OF ILLUSTRATIONS

LIST OF ILLUSTRATIONS (cont)

LIST OF ILLUSTRATIONS (cont)

LIST OF TABLES

LIST OF ACRONYMS

a	- flaw depth
A/D	- analog-to-digital
CATE	- ceramic applications in turbine engines
2c	- measured flaw length
CRT	- cathode ray tube
2-D	- two-dimensional
3-D	- three-dimensional
D_x	- PAM measured flaw width in x-direction equivalent to photoacoustic signal width
D_y	- PAM measured flaw length in the y-incremental direction equivalent to 2C
D_a	- actual hole diameter
d	- distance between two flaws
FPI	- fluorescent penetrant inspection
HPSN	- hot-pressed silicon nitride
MOR	- modulus of rupture
NDE	- nondestructive evaluation
PAM	- photoacoustic microscopy
RBSN	- reaction bonded silicon nitride
rms	- root mean square
SDB	- styrene divinyl benzene
SDH	- side drilled holes
SNR	- signal-to-noise ratio
TDH	- top drilled holes
μ_s	- thermal diffusion length
y	- subsurface location of the flaw from the top interrogating surface of the specimen

I. SUMMARY

Successful utilization of structural ceramic materials in heat engines depends on reliable failure and life prediction schemes, both of which require detection and characterization of minute strength-controlling surface and subsurface flaws of 10-250 micron size. Photoacoustic microscopy (PAM) has been shown to detect such failure initiating defects in silicon base materials. The objective of the NASA funded Nondestructive Evaluation of Structural Ceramics by Photoacoustic Microscopy (PAM) program was (1) to develop a photoacoustic microscopy imaging system, (2) to sequentially characterize silicon nitride material in green, as-fired, and machined stages of ceramic fabrication process, and (3) to detect and predict failure initiating defects in silicon nitride.

A PAM digital data acquisition, imaging, and analysis system was successfully developed and used during this program. Menu driven algorithms were developed in machine language and implemented for rapid data acquisition and image processing. The system is capable of creating 16 color images with magnification, scroll images in all four directions on the CRT screen, and threshold acquired PAM signals. In addition, flaw location, size, and the detected PAM signal can be quantified.

Reference standards of silicon nitride material were fabricated at the various stages of processing and examined to optimize experimental PAM parameters to detect surface and subsurface flaws in unknown specimens. The results are the following:

- o The photoacoustic characterization of the green material revealed that the material is volatilized and removed by the laser energy, thus significantly limiting the use of PAM as an in-process nondestructive evaluation technique. Surface holes of 100 micron nominal diameter were detected. Subsurface holes were undetected even within one thermal diffusion length indicating that the thermal waves are rapidly dampened and attenuated by the open microstructure of the green material.
- o Simulated surface holes of 130 μm diameter x 28 μm depth were readily detected and discerned with a resolution of 8 μm in machined

sintered silicon nitride. The magnitude of the PAM signal increased linearly up to a surface flaw depth of one thermal diffusion length. The PAM measured flaw size was comparable to the actual flaw size in both the x- and y-directions with an offset.

- o It was demonstrated that subsurface holes of up to 440 micron diameter were detected up to a depth of 570 micron below the interrogating surface in sintered silicon nitride. Seeded voids of 20-30 micron size located at the surface and 50 micron below the interrogating surface were detected in sintered silicon nitride both by PAM and microradiography with 1% x-ray thickness sensitivity. Tight surface cracks 96 micron length x 48 micron depth were detected in machined silicon nitride.

Subsurface holes 250 micron diameter 1.00 mm below the interrogating surface were detected in as-fired sintered silicon carbide.

Green, as-fired, and machined silicon nitride specimens were characterized using the optimized PAM parameters. The material was volatilized in green specimens suggesting that PAM is not a viable technique in the green state. Examination of the sintered as-fired specimen surfaces disclosed the presence of linear shallow microcracks in the photoacoustically examined region suggesting that the material was damaged by PAM characterization in the green state. Photoacoustic microscopy detected 10 to 100 micron size surface and subsurface pores and inclusions, respectively, up to 80 micron below the interrogating surface in machined sintered silicon nitride. The failure controlling sites could not be predicted apriori because a large number of competing PAM signals of equal or greater magnitude from other flaws were also present. The room temperature flexural strength of machined sintered silicon nitride was 685.3 MPa with a Weibull modulus (m) of 6.5. Fracture was controlled by surface and subsurface pores and inclusions.

Correlation studies revealed that flaw characteristics have a significant affect on flaw detection by various NDE techniques. Photoacoustic microscopy detected fracture controlling flaws in substantially more specimens than microradiography and ultrasonic techniques. The magnitude of the photoacoustic signal varied randomly for a given flaw depth, length, aspect ratio, and flexural

strength with no trend. The flaw size was overpredicted by PAM in the x-direction with mixed results in the y-direction.

Overall, the goals of the program for sintered material were successfully attained. A PAM imaging system was developed and implemented to detect fracture controlling flaws of 10 to 250 microns in size. Additional theoretical and quantitative work is needed to develop a better understanding of the relationship between the PAM signal and fracture controlling flaw characteristics before defects can be identified apriori. This work has provided a firm basis and direction for future efforts to further develop photoacoustic microscopy and other thermal wave imaging methods for structural ceramic materials.

II. INTRODUCTION

Polycrystalline silicon base structural ceramic materials are currently being used to develop hot flow-path components in vehicular/industrial gas turbine engines. It was recognized early in the Ceramic Applications in Turbine Engines (CATE) program that the successful use of these brittle ceramics can only be achieved with the advent of reliable failure and life prediction schemes, both of which require detection and characterization of minute strength-controlling surface and subsurface flaws (e.g., voids, cracks, and inclusions) of 10-250 micron size. These inherent flaws, which are normally introduced during the various stages of the fabrication process, are generally responsible for the wide variability in flexural strength. Nondestructive detection of these flaws can screen out defective parts and substantially reduce variability, offering the potential for increased operating stresses. The problem was addressed both under the CATE (Ref 1) and AGT 100 programs. Advanced nondestructive evaluation (NDE) techniques, such as high frequency ultrasonics (Ref 2), projection microradiography, ultrasonic velocity (Ref 3), and photoacoustic microscopy (PAM) were used to characterize structural ceramic materials and components. Many workers have shown that photoacoustic microscopy is one of the most sensitive NDE techniques for detecting tight surface cracks (Ref 4 and 5) in flat structural ceramic specimens. It was demonstrated (Ref. 6) that 20 to 50 micron size surface and near subsurface fracture controlling natural pores can be detected in injection molded alpha silicon carbide ceramic turbine blades by PAM. These flaws precipitated the failure of blades during burst testing.

The photoacoustic effect (Ref 7) is dependent not only on the material optical properties, but also on its thermal characteristics. When a beam of intense energy such as a laser is focused, modulated and scanned across a sample, it is absorbed at or near the surface, and periodic surface heating results at the modulation frequency. This periodic heating produces highly damped and diffusive thermal waves in the heated region of the material and causes surface temperature oscillations. In gas-cell PAM, these oscillations on the sample surface cause variations in the gas pressure inside the closed cell, which are detected by a microphone as an acoustic signal. Gas-cell photoacoustic microscopy is a thermal wave imaging method.

Flaw detection and depth of penetration of the thermal waves in photoacoustic microscopy depends on the thermal diffusivity (α) of the material and the modulation frequency (f) of the optical source, such as a laser, both of which affect the thermal diffusion length (μ_s) as given below:

$$\mu_s = \left(\frac{\alpha}{\pi f}\right)^{1/2} \quad (1)$$

The photoacoustic signal is a complex signal and has both magnitude and phase. The depth of penetration in the magnitude mode is approximately 1 to 1.5 times the thermal diffusion length and twice that in the phase mode. The spatial (lateral) resolution at the surface is controlled by the focal spot diameter of the laser beam and in the subsurface region is limited by the size, depth, and spacing between the flaws relative to the thermal diffusion length. In the extreme near field, however, the intrinsic resolution is a function of flaw characteristics and independent of the thermal diffusion length (Ref 8).

The purpose of this program was to further the state-of-the-art of photoacoustic microscopy technology and apply it at the various stages of the fabrication process of structural ceramic materials to detect defects that can cause low strength and premature failure. The specific goals of the program were the following:

- o develop a computerized photoacoustic microscopy data acquisition, imaging, and analysis system
- o develop a capability for detecting voids and inclusions ranging in size from 10 μm to 250 μm at depths ranging from 40 μm to 1 mm, respectively, from the specimen surface being interrogated
- o develop a capability for detecting surface connected cracks
- o demonstrate the ability of NDE to predict the failure site on MOR bars containing natural flaws

These broad objectives were addressed in a sequential approach as shown in Figure 1 by characterizing silicon nitride material in green, as-fired, and machined states to determine the effectiveness of photoacoustic microscopy as an in-process NDE technique and to detect failure initiating flaws. The technical work conducted under this program is described in detail in the following sections.

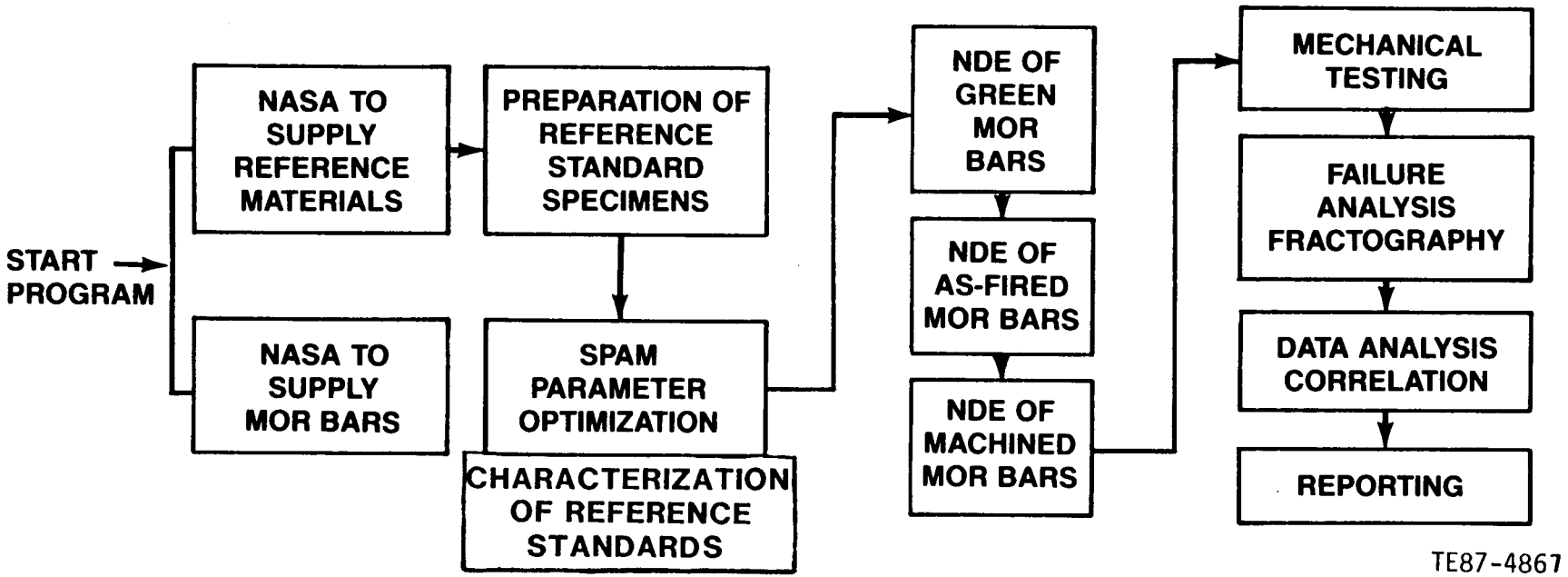

Figure 1. Program flow chart showing in-process characterization of silicon nitride material.

III. MATERIALS

The sintered silicon nitride specimens examined in this study were fabricated by NASA-Lewis Research Center. The starting AME high purity Si_3N_4 powder was first sifted with ethanol through a 20 micrometer sieve. The Si_3N_4 was then combined with Y_2O_3 and SiO_2 powder additions, and 100 g charges were milled for 100 hr in reaction bonded silicon nitride (RBSN) mills using hot-pressed silicon nitride (HPSN) media and ethanol. The ground slurry was sifted through a 10 micrometer sieve and then dried in a drying apparatus employing a heated water bath and a vacuum connection for removal of ethanol vapor. The softly agglomerated powders were further dried in a vacuum oven at 110°C, crushed with an agate mortar and pestle, and sifted through a 149 micrometer sieve. The specific surface area determined by the BET method was 19.0 m^2/g. This powder was then die-pressed into bars at 21 MPa. The die-pressed bars measured 3.81 x 0.79 x 0.52 cm and weighed 2.6 g each. The bars were then vacuum sealed in latex tubing and isostatically cold pressed at 414 MPa.

Forty-five green silicon nitride bars were fabricated by NASA and sent to Allison. The average dimensions and dry weight of the specimens were 3.6 cm x 0.75 cm x 0.5 cm and 2.56 gm, respectively. Subsequent to Allison evaluation of the green bars, they were sintered at 2150°C for 2 hr under 5.0 MPa nitrogen pressure. Forty-four sintered silicon nitride bars with as-fired surfaces were returned by NASA. The average dimensions of the specimens were 3.0 cm x 0.62 cm x 0.42 cm and the density was 3.25 gms/cc. The as-fired specimens were examined by Allison. Forty-four bars were sent for machining to BOMAS Machining, Somerville, Massachusetts. The nominal size of the specimens was 3 cm x 0.56 cm x 0.28 cm with a surface finish of 0.2 μm (8 μin.) rms. The average density was 3.243 gms/cc. The edges of all the machined specimens were beveled.

IV. THERMAL DIFFUSIVITY MEASUREMENT

Photoacoustic characterization of materials requires measurement of their thermal diffusivity (α) to determine the thermal diffusion length (μ_s) at a given laser modulation frequency and to calculate the depth of penetration by photoacoustic microscopy (PAM). Thermal diffusivity was measured by laser flash technique at Fiber Materials, Inc, Biddeford, Maine. In this method, one face of a circular disk-shaped specimen is subjected to a short duration heat pulse, and the thermal response on the opposite face is analyzed in terms of time and disk thickness to provide the diffusivity value. The measurements were conducted from room temperature to about 300°C in green sintered silicon nitride and sintered silicon carbide. The green specimen was hand formed to 1.27 cm diameter x 0.0625 cm thickness. Specimens of the sintered silicon nitride, and carbide were ground to 1.27 cm diameter x 0.150 cm thickness by BOMAS Machining, Somerville, Maine. Figure 2 shows the thermal diffusivity of the three specimens. The diffusivity of the green material dropped slightly from 0.003 cm^2/sec at room temperature to 0.0024 cm^2/sec at 203°C. Also, the room temperature diffusivity of sintered silicon nitride and carbide decreased from 0.181 cm^2/sec and 0.568 cm^2/sec to .0098 cm^2/sec and 0.255 cm^2/sec, respectively, at 300°C. The repeatability of measurement was $\pm$5% absolute based on measurements of National Bureau of Standards (NBS) reference standard materials.

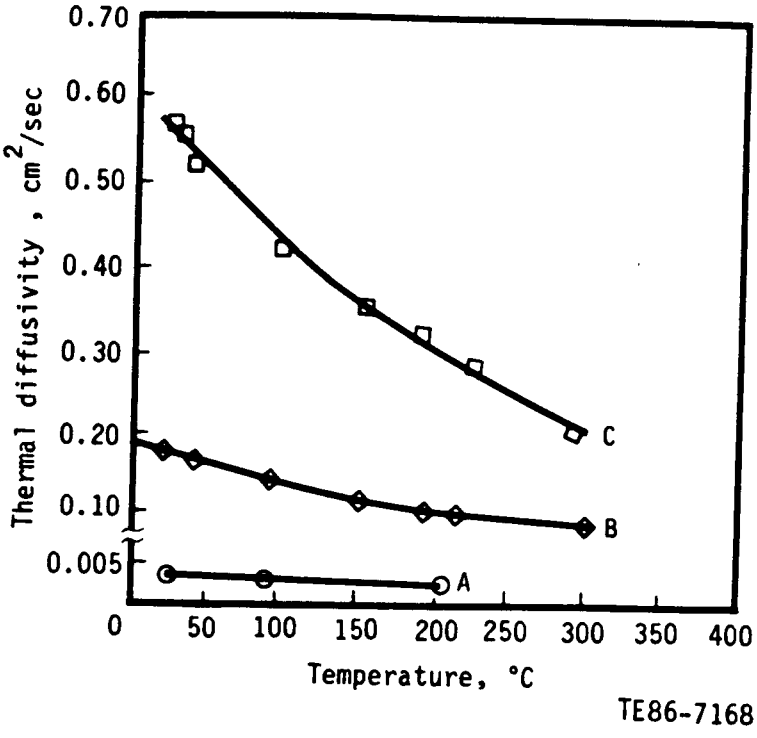

Figure 2. Thermal diffusivity of green silicon nitride (A), sintered silicon nitride (B), and sintered silicon carbide (C).

V. FABRICATION OF REFERENCE STANDARDS

Optimization of photoacoustic parameters to detect surface and subsurface flaws requires fabrication of reference standard specimens with artificially induced flaws. Standards were prepared to simulate voids at the surface with top drilled holes (TDH) and at the subsurface with side drilled holes (SDH) and seeded voids. All the holes were drilled by ultrasonic machining at Bullen Ultrasonics, Eaton, Ohio. Tight surface cracks were introduced by a Knoop indenter. The following subsections describe the fabrication of various reference standards of silicon nitride and silicon carbide materials.

5.1 GREEN SILICON NITRIDE

The isopressed green silicon nitride material had 40-50% porosity and was very fragile. The open structure of the material leads to the poor detection of small surface and subsurface flaws. In green materials, only gross variations in material microstructure can be detected. Figure 3 shows that TDHs of 106 to 183 μm diameter were machined to depths ranging from 0 to 875 μm to simulate surface voids. The specimen was severely chipped in the vicinity of hole No. 6 during the machining operation. Subsurface SDHs (Figure 4) of 375 μm diameter were machined at 25 to 250 μm depth below the top interrogating surface. This specimen broke in transit in the area of hole No. 8.

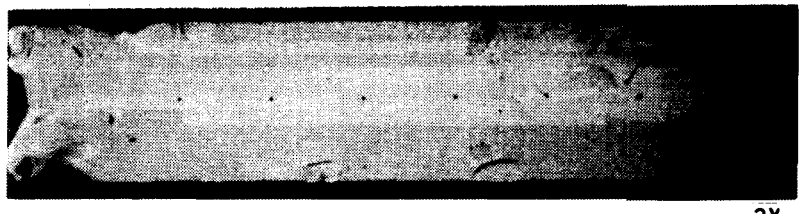

Hole no. 1 2 3 4 5 6 7 8 3X

Hole no.	1	2	3	4	5	6	7	8
Diameter*, μm	106	106	106	132	183	183	183	157
Depth**, μm	NM	200	275	325	425	500	625	875

NM--too shallow to measure
*Measured using optical micrography
**Measured using X-ray radiography

TE87-2186

Figure 3. Layout of top drilled holes (TDH) in green silicon nitride bar.

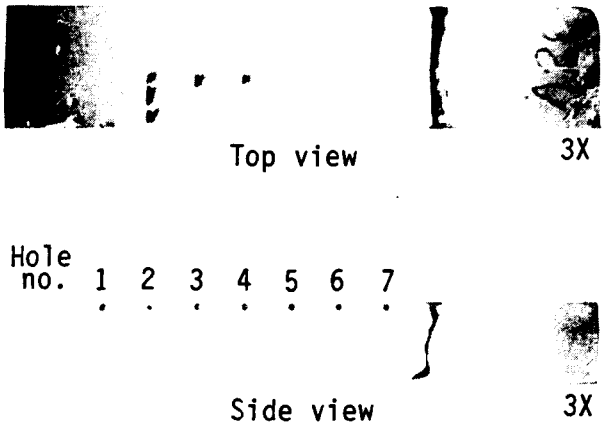

Hole no.	Location from top surface, μm
1	183
2	157
3	132
4	160
5	157
6	155
7	236
8	Specimen broke in transit

Nominal diameter of holes ~ 375 μm

TE87-2185

Figure 4. Layout of the subsurface side drilled holes (SDH) in green silicon nitride bar.

5.2 AS-FIRED SILICON NITRIDE

The green silicon nitride material was sintered and characterized for the presence of subsurface flaws in the as-fired state. The detection of subsurface volume flaws depends on the thermal diffusivity of the material and the laser modulation frequency. SDHs of 375 μm nominal diameter (Figure 5) were machined at various locations ranging from 0 to 1015 μm below the interrogating surface. The location of the holes was measured from the specimen edge to the top of the hole.

5.3 MACHINED SILICON NITRIDE

The as-fired modulus of rupture (MOR) bars were machined to a surface finish of 8 μm in. root mean square (rms). The depth of thermal wave penetration and flaw detection was determined using a specimen with SDHs (Figure 6) of 440 μm nominal diameter machined ultrasonically from 88 to 890 μm below the surface. In addition, three holes of 300, 840, and 1100 μm diameter were drilled to study the detection of larger flaws at a depth of 1.0 mm below the surface.

Subsurface resolution in photoacoustic microscopy (PAM) depends on the flaw size, location, and distance between two flaws as a function of thermal

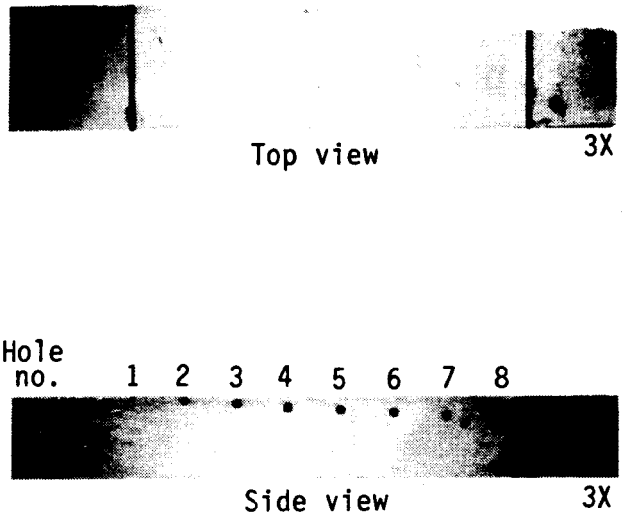

Hole no.	Hole location from top surface μm
1	Open to surface
2	Very near to surface but not open
3	156
4	390
5	547
6	665
7	825
8	1015

Nominal diameter ≃ 375 μm
Nominal distance between holes ≃ 2.5 mm
Approximate depth ≃ 3.125 mm

TE87-2184

Figure 5. Layout of the side drilled holes in as-fired sintered silicon nitride.

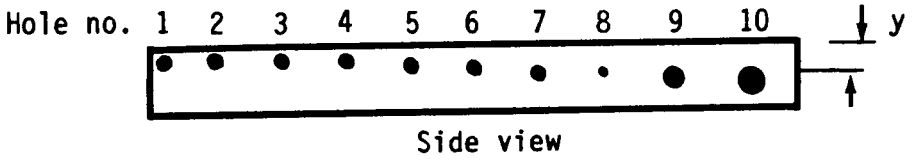

Hole no.	Hole diameter, μm	Hole depth (y), μm
1	441	88
2	441	176
3	441	352
4	441	485
5	441	573
6	441	662
7	441	882
8	309	970
9	838	970
10	1102	1014

TE86-7162

Figure 6. Layout of side drilled holes in machined sintered silicon nitride.

diffusion length. A reference specimen (Figure 7) with 400 μm nominal diameter SDHs at about 130 μm below the surface was machined. The distance between the holes was varied from 130 to 650 μm to find the discernable limit of the flaw spacing.

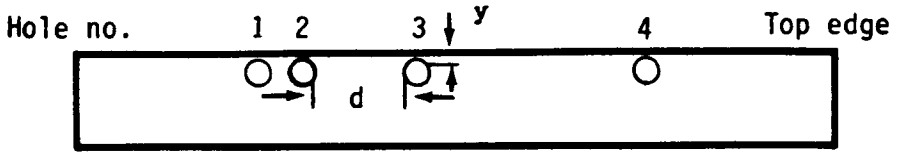

Side view

Hole no.	Depth of holes (y), μm	Distance between Holes	d, μm
1	88		
2	132	1 - 2	132
3	132	2 - 3	345
4	132	3 - 4	650

Nominal diameter of holes ≈ 400μm.

TE86-7163

Figure 7. Layout of subsurface side drilled holes in machined sintered silicon nitride.

Resolution of surface flaws by PAM depends primarily on the focal spot size of the laser beam. A specimen with seven TDHs (Figure 8) was prepared by ultrasonic machining to measure the spatial surface resolution of the laser. The holes had a different diameter, depth, and distance between them. The largest spacing between the holes was 953 μm and the smallest was about 8 μm.

Tight surface cracks were simulated by a Knoop indenter in the machined surface of sintered silicon nitride to optimize PAM parameters for evaluating unknown specimens. Indentations of 1, 2, and 5 kg load were introduced on the interrogating surface (Figure 9) corresponding to crack lengths of 100, 143, and 234 μm respectively. The specimen was examined before and after removing the indentor induced surface damage. The flaw produced by the Knoop indentor consists of a half-penny-shaped median crack (Ref. 9) below the major axis of the indentation. In addition, lateral and radial microcracks also occur (Ref 10). The extent of microcracking and subsurface damage depends on the hardness and fracture toughness of the material and also on the interaction between the indentor at the given load and the local microstructure. The depth (a) of the crack is approximately half the surface crack length (2c).

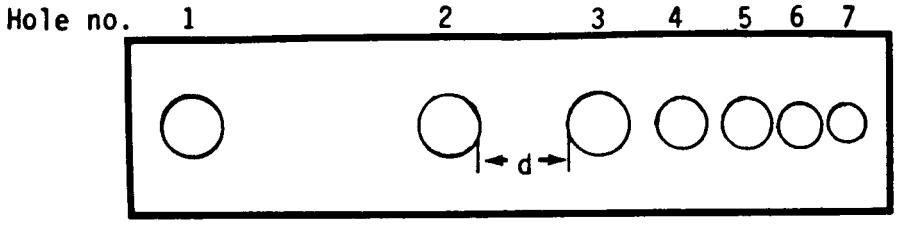

Hole no.	Diameter µm	Depth µm	Distance between Holes d, µm	
1	265	470		
2	265	366	1 - 2	953
3	265	234	2 - 3	445
4	221	213	3 - 4	143
5	221	94	4 - 5	40
6	176	56	5 - 6	12
7	132	28	6 - 7	8

TE86-7164

Figure 8. Layout and measured dimensions of top drilled holes (TDH) in machined sintered silicon nitride.

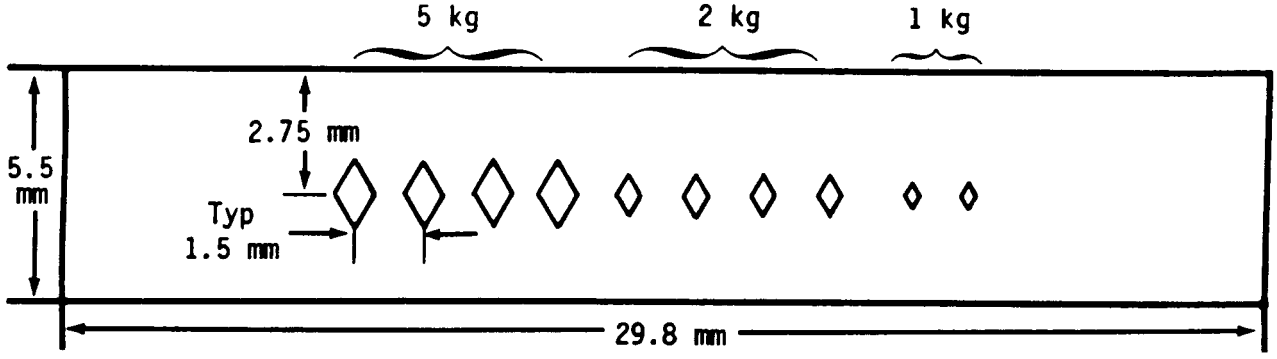

Load (kg)	Crack Length (2c) µm	Crack Depth* (a) µm
5	234	117
2	143	71
1	100	50

*Assuming semicircular flaw, a = c

TE86-7165

Figure 9. Layout of Knoop indentations in a machined specimen of sintered silicon nitride. Crack length was measured optically.

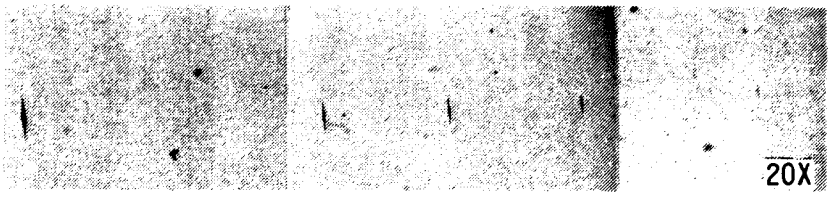

Crack no. 1 2 3 4 5 6

Optical

Crack no.	Load (Kg)	Crack Length (2c)	Depth* (a)
1	12	401	200
2	10	323	162
3	5	234	117
4	4	205	102
5	2	140	70
6	1	96	48

*Assuming semicircular flaw, a = c

TE86-7166

Figure 10. Layout of Knoop indentations in hot-pressed silicon nitride (NC132). Crack length was measured optically.

5.4 HOT PRESSED SILICON NITRIDE (NC132)

Tight surface cracks were introduced in the machined surface of an NC132 bar by Knoop indentation to determine the detectability of surface cracks by PAM and to compare these findings with the results of the machined sintered silicon nitride obtained under identical optimum PAM conditions. This specimen was also used to conduct a PAM parametric study to optimize scanning speed, modulation frequency, and sensitivity for maximum single-to-noise ratio. Knoop indentations from 1 to 12 kg were made. Figure 10 shows the layout and the optically measured dimensions of the surface cracks in hot pressed silicon nitride. The smallest crack was 96 μm long and the largest was 400 μm in size. The indentor induced surface damage was not removed.

5.5 AS-FIRED SILICON CARBIDE

Subsurface hole detection studies were conducted in a sintered silicon carbide specimen with as-fired surface. SDHs of 250, 500, 750, and 1000 μm diameter were drilled at 1.0 mm depth below the interrogating surface, as shown in Figure 11.

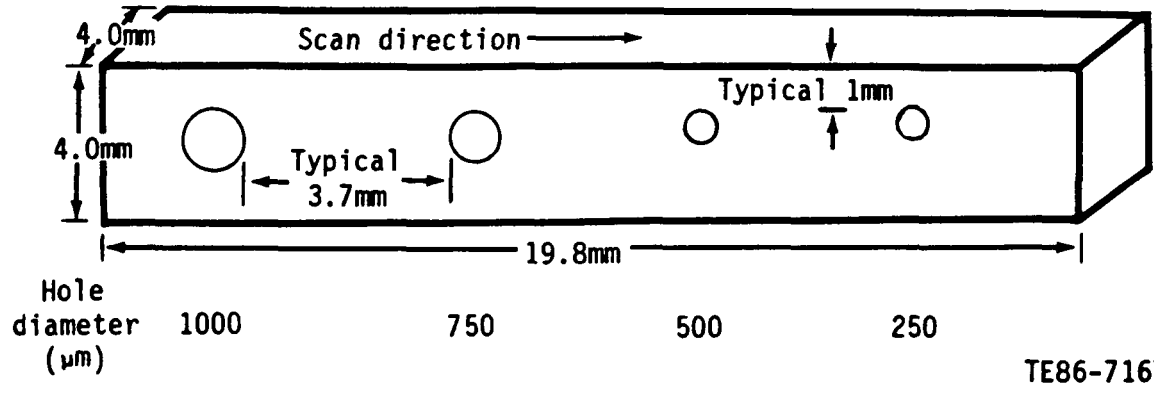

Figure 11. Layout of side drilled holes in as-fired sintered silicon carbide specimen.

5.6 INTERNALLY SEEDED VOID SPECIMENS

Three seeded specimens--two of sintered silicon nitride and one of sintered silicon carbide--were prepared by NASA-Lewis Research Center. The rectangular MOR specimens were prepared by pouring a selected amount of powder composition into a double action tungsten-lined die and leveling the powder. Then, a selected number of styrene divinyl benzene (SDB) microspheres of the same size were placed on the surface of the powder layer. Thereafter, more powder of the same composition was placed in the die, and the whole green layer was pressed at 120 MPa to form a green specimen. The specimen was removed from the die, and its surfaces were dusted. Final compaction of the green specimen was accomplished by vacuum sealing the seeded test bar in thin wall latex tubing and cold isopressing it at 420 MPa. After compaction the seeded specimens were heated under vacuum to approximately 550°C (45-60 min hold at maximum temperature) to decompose the SDB microspheres. The green silicon nitride test bars were sintered at 2140°C for 2 hr under a static nitrogen pressure of 5 MPa. The green silicon carbide specimen was sintered at 2200°C for 30 min under an argon pressure of 0.1 MPa.

Two silicon nitride specimens were seeded with voids: one with 150 to 300 μm diameter voids located 550 to 1600 μm below the surface and the second with 20 to 50 μm diameter, shown in Figure 12, voids located 20 to 50 μm below the surface. One silicon carbide specimen was fabricated with 180 to 450 μm voids located 270 to 1300 μm below the interrogating surface.

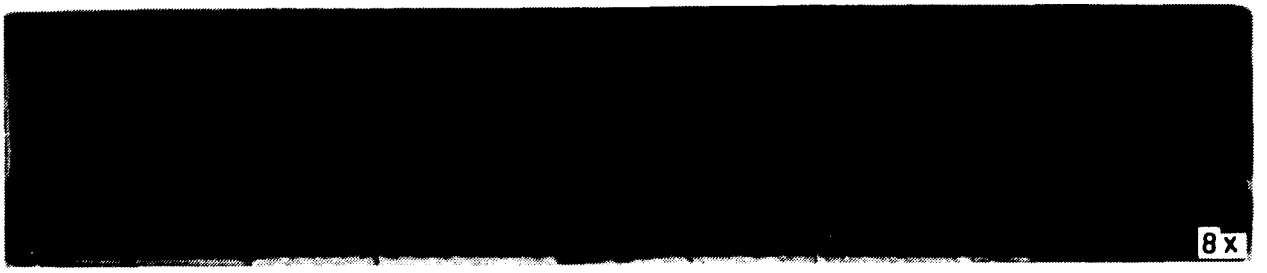

Optical micrograph

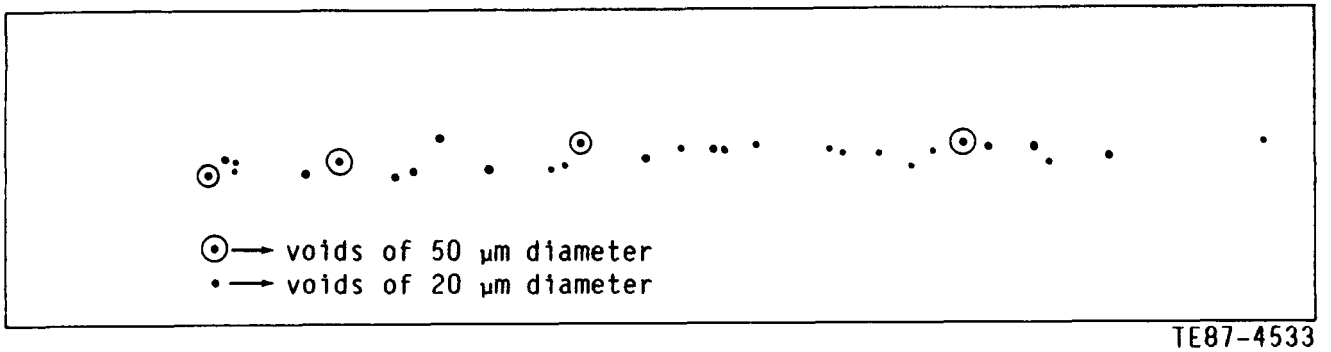

(Layout provided by NASA-LeRC)

Figure 12. Layout of seeded voids in sintered silicon nitride reference specimen.

VI. EXPERIMENTAL PROCEDURE

6.1 ULTRASONIC VELOCITY

The ultrasonic velocity of waves through linear elastic isotropic materials is related to the density and elastic modulus by the following equations:

$$V_L = \left(\frac{E}{\rho}\frac{(1-\nu)}{(1+\nu)(1-2\nu)}\right)^{1/2} = \frac{2\eta L}{t} \tag{2}$$

$$V_T = \left(\frac{G}{\rho}\right)^{1/2} = \left(\frac{E}{\rho}\frac{1}{2(1+\nu)}\right)^{1/2} = \frac{2\eta L}{t} \tag{3}$$

$$\nu = \frac{1-2\,(V_T/V_L)^2}{2-2\,(V_T/V_L)^2} \tag{4}$$

where

- V_L = longitudinal wave velocity
- V_T = shear or transverse wave velocity
- E = elastic modulus
- G = shear modulus
- L = thickness of specimen
- t = wave transit time between two selected back surface echoes
- η = 1 when transit time between first and second back surface echoes
- η = 2 when transit time between first and third back surface echoes
- ρ = density of the material
- ν = Poisson's ratio

By measuring the specimen thickness and transit time of the acoustic wave through the medium, the preceding relationships provide a means of determining the ultrasonic velocity, moduli, and Poisson's ratio of the material.

Both longitudinal and shear wave velocity of machined specimens were determined using a computer-aided transit time (t) measurement system developed at Allison. Figure 13 shows schematically the experimental system assembled at Allison for measuring the ultrasonic velocity of material. The system consists of a Tektronix WP 1310 signal processing system, a Panametrics 75 MHz Model 5052PRX-75 pulser/receiver, and flat delay line (fused silica) transducers--

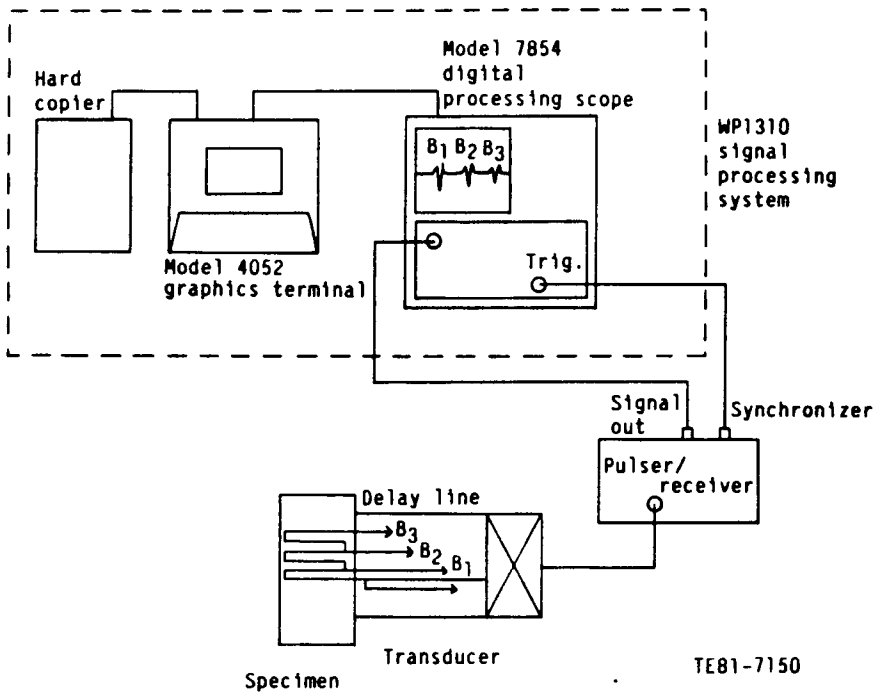

Figure 13. Schematic of ultrasonic velocity measurement apparatus.

30 MHz for the longitudinal (L) wave and 20.0 MHz for the shear (S) wave for flat specimens. The thickness of the specimens is measured using a micrometer with 0.0001 in. accuracy.

The transit time (t) between the echoes is measured under software control from the keyboard, using algorithms developed at Allison. Optimum reflected ultrasonic signals are digitized to the maximum resolution (1024 bits) available with the scope. The oscilloscope sweep rate is adjusted so that only the echoes of interest are visible on the cathode ray tube (CRT) screen. The oscilloscope is programmed to (1) average the signals 20 times; (2) measure the travel time between the echoes of interest by program-controlled cursors; (3) store the time in constant memory registers; and (4) repeat steps 1 through 3 ten times to minimize the random variations in the digitization of the signals. The accuracy of time-of-flight measurement is within 1 nanosecond.

The time of flight (t) for a specimen is the arithmetic average of the 10 measurements. The ultrasonic velocity for each specimen is calculated using the measured thickness (L) and wave travel time (t) in the previously cited equations. A hard copy with specimen number, density, and measured velocity is then made for permanent record. The elastic and shear moduli, as well as the Poisson's ratio of the material, can be calculated.

6.2 ULTRASONIC FLAW DETECTION

Because of the necessity for detection of small flaws of 25-200 μm in structural ceramics, frequencies much higher than those in conventional use have to be employed. A 50.0 MHz computer-assisted ultrasonic imaging system, shown in Figure 14, was used to evaluate the machined surface of the modulus of rupture (MOR) specimens. This system consists of a programmable x-y scanner, a 75 MHz broadband pulser/receiver, a gated peak detector, a 16-gray scale image recorder, and a 50 MHz nominal frequency 1.27 cm (0.5 in.) focal length focused transducer. The reflected radio frequency (rf) signal is gated, peak detected, and converted into a dc signal. This signal is displayed on a 16-gray scale recorder. The images can be magnified easily to 20x or more.

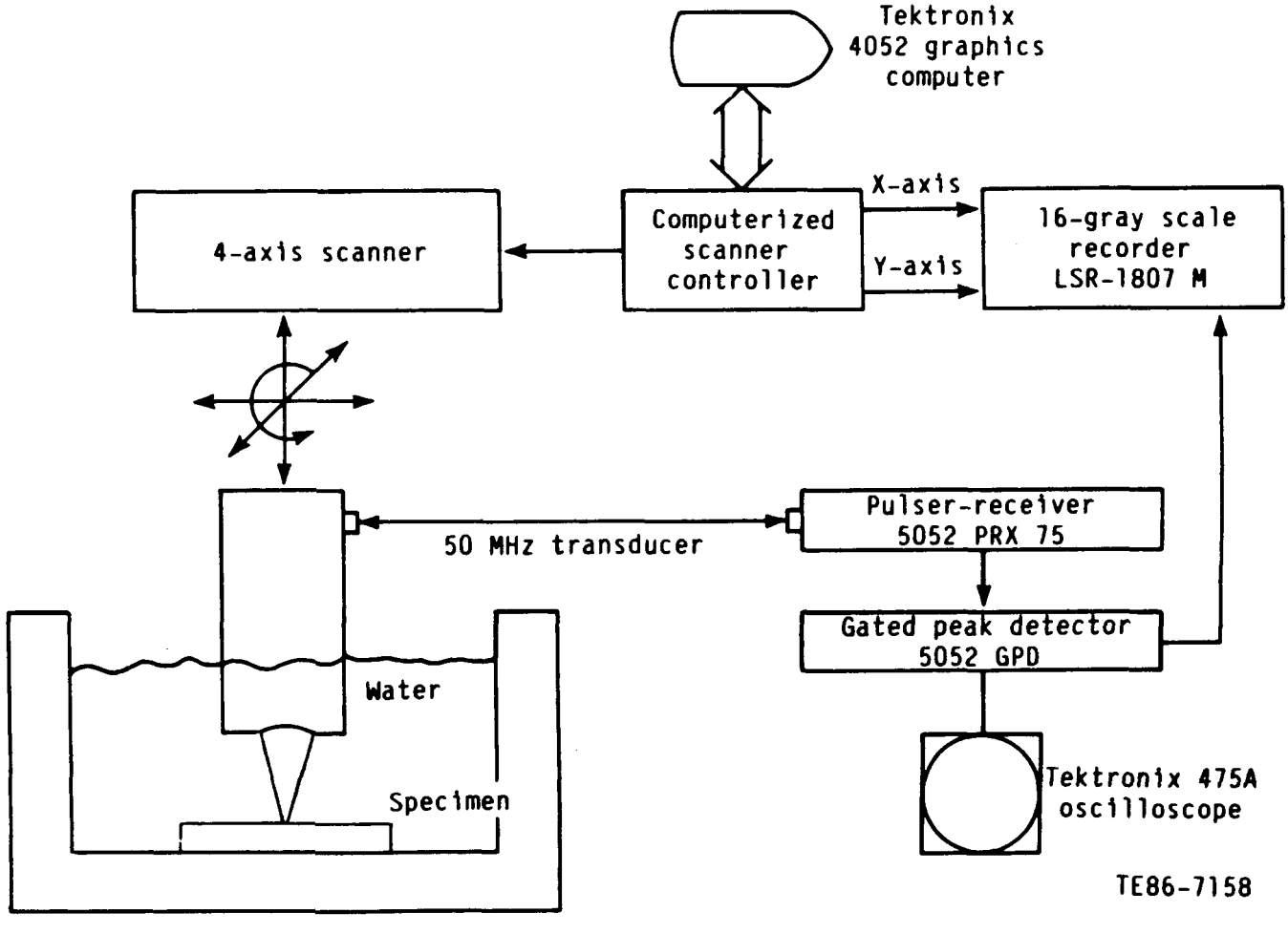

Figure 14. Ultrasonic flaw detection and imaging system.

The transducer was focused on the front surface of each machined MOR bar for maximum sensitivity. This surface was selected to be subjected to tensile stresses in subsequent mechanical testing. The reflected front surface echo was gated and the peak detected signal was imaged on the gray scale recorder. A 10x acoustic image of the tensile surface of each bar was recorded. A silicon carbide specimen with about 40 μm simulated surface void was used as the reference standard. This specimen was imaged with all the bars to ascertain the repeatability of surface flaw detection.

6.3 MICROFOCUS RADIOGRAPHY

X-ray radiography is an effective nondestructive evaluation technique to detect critical flaws in structural ceramic materials. Optimum flaw detection requires both good spatial resolution and high image contrast. Resolution in x-ray radiography is dependent on the focal spot diameter of tube, which controls the geometric unsharpness (U_g) by the equation

$$U_g = F_s * \frac{a}{d} \qquad (5)$$

where F_s is the focal spot diameter of the X-ray tube, d the source-to-object distance, and a the object-to-film distance. Conventional systems with a large focal spot diameter have excessive geometric unsharpness resulting in poor spatial resolution. Microfocus X-ray tubes with small focal spot diameters (1-100 μm) have negligible U_g and are essential to resolve critical flaws in ceramic materials. Final image contrast (C) in the microfocus X-ray system can be given by

$$C = K \cdot Wm \cdot X \qquad (6)$$

where K is the image medium constant, Wm is the difference in the X-ray absorption of the defect and parent material at a given voltage, and X is the defect size in the direction of the X-ray beam.

A real-time FeinFocus microfocus X-ray system, shown in Figure 15, was used to detect flaws in silicon nitride specimens. The system consists of a microfocus X-ray tube, a parts handling system, dual field (4 in./6 in.) intensifier,

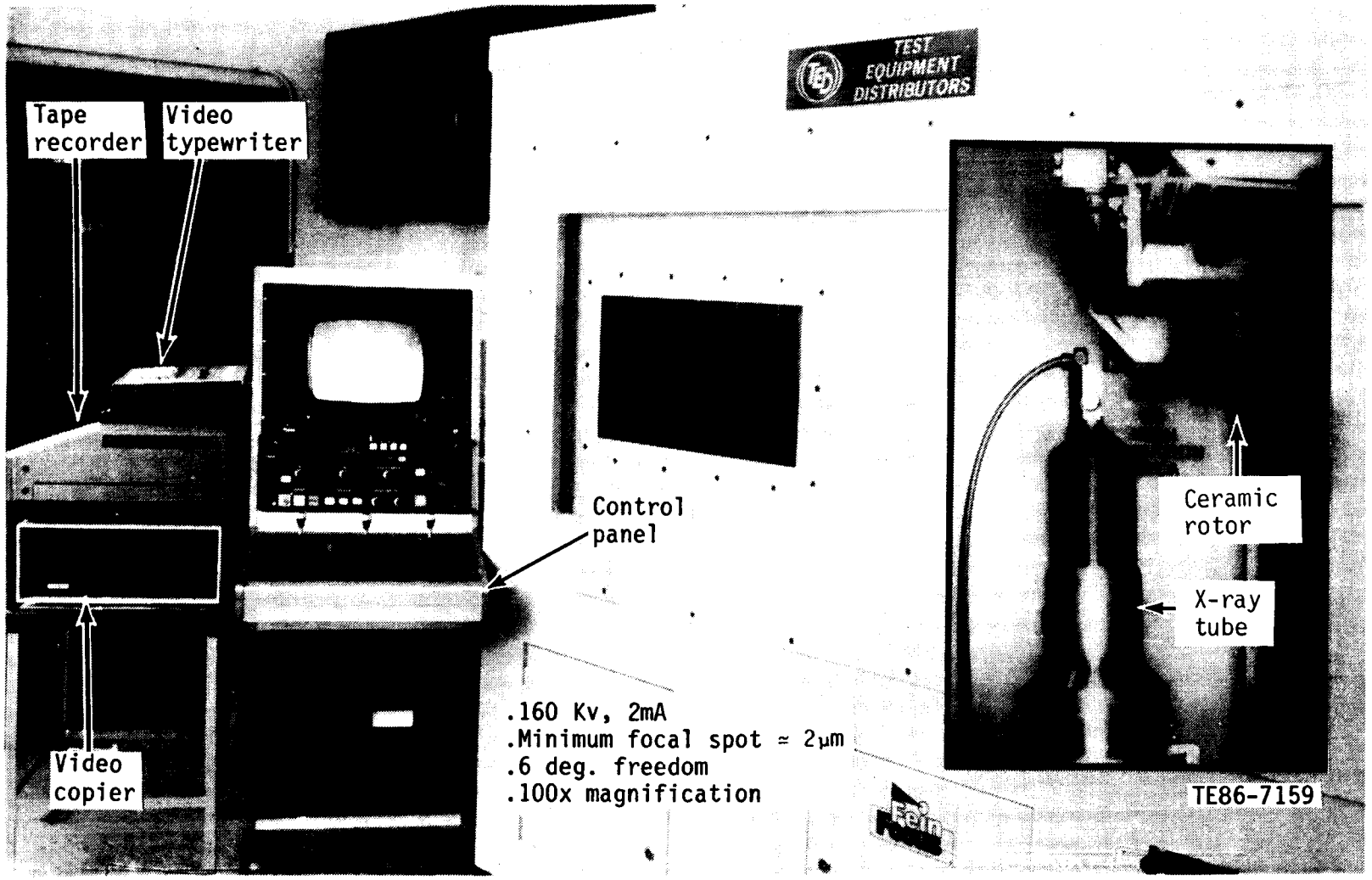

Figure 15. Real-time microfocus X-ray system at Allison Gas Turbine.

video camera (Vidicon or Plumbicon), control panel, 3/4 in. tape recorder, video typewriter, and a video copier. This system is capable of operating up to 160 K_eV voltage and 2 mA current with maximum incident photon energy of 320 W. The focal spot of the X-ray beam can be varied from 1 to 100 μm providing an extremely sharp image of the detected flaws. The X-ray tube, parts handling system, and the X-ray recording medium (film or intensifier/camera assembly) are enclosed in a leaded radiation proof cabinet (Figure 16). The system has 6 deg of freedom that can be controlled by joysticks. The parts-handling system has 5 deg of freedom for optimum component orientation and flaw detection. Intensifier/camera assembly can also be moved along the X-ray beam axis. Control on the distance of the X-ray source from the part and intensifier/camera assembly, respectively, along the beam axis enables optimum flaw detection and magnification, which is critical for small flaw detection in ceramic materials.

All the green, as-fired, and machined specimens were evaluated by microfocus radiography. The X-ray parameters were established using specimens with simulated defects. The source-to-film distance was 61 cm and source-to-object distance was 12.0 cm for all the specimens. Four specimens at a time were placed immediately next to each other in a plastic holder and were radiographed. Each specimen was radiographed from the top and the side revealing the three-dimensional (3-D) location of detected defects.

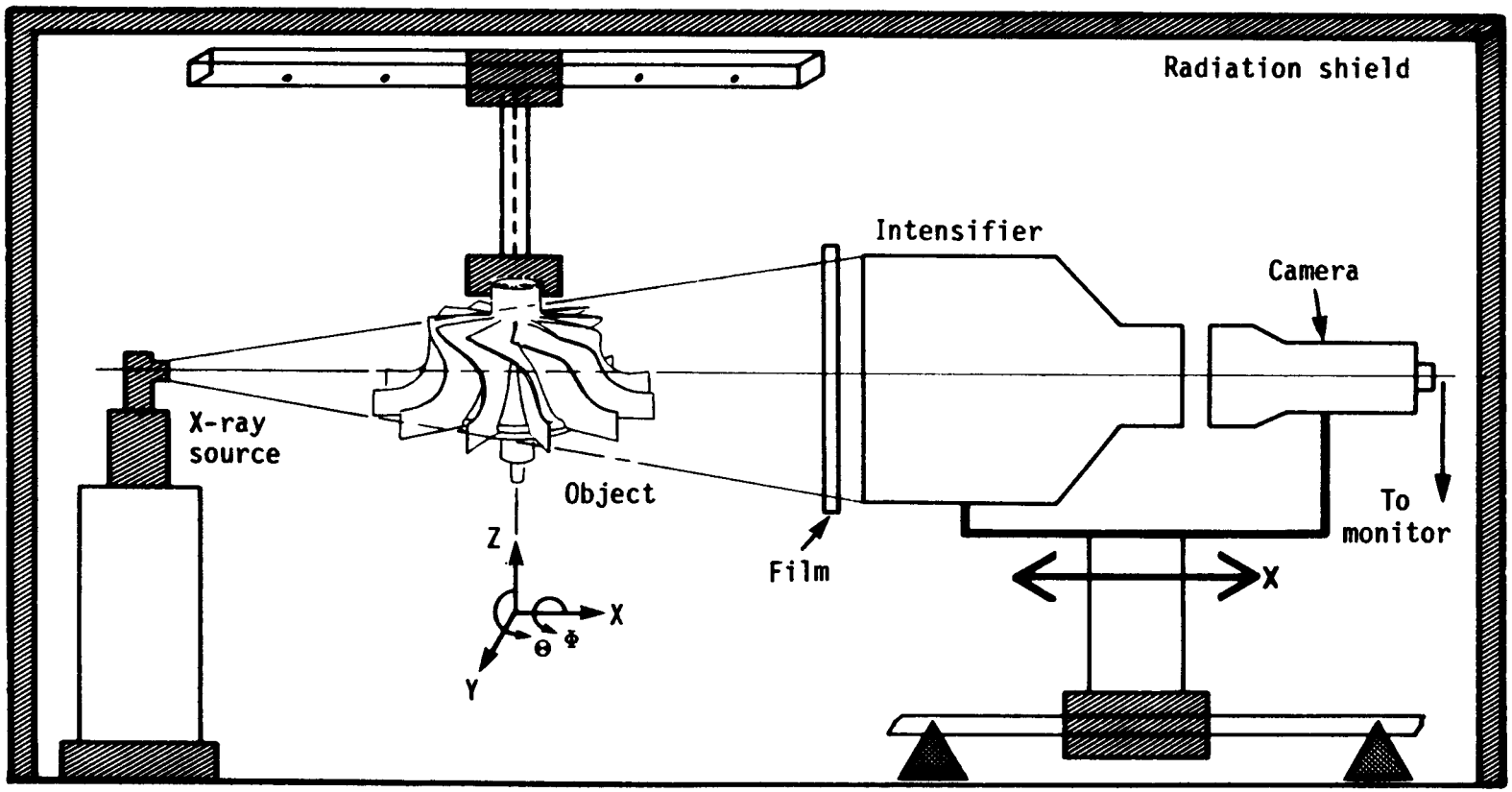

Figure 16. Schematic of component inspection technique by projection microradiography using FeinFocus X-ray system.

6.4 SCANNING PHOTOACOUSTIC MICROSCOPY

Experimental Arrangement

The photoacoustic microscopy (PAM) arrangement at Allison, shown in Figure 17, uses a 2.0 W argon laser. The laser light is modulated by an electromechanical chopper and guided by two mirrors and a beam steerer toward an objective lens, which focuses the light onto the specimen surface. The diameter of the focal spot is less than or equal to 25 microns. The specimen is positioned in a PAM cell, which is mounted on a two-dimensional (2-D), servo-controlled translational stage. The specimen/cell assembly is translated in the x-direction and incremented in the y-direction. The entire system is situated on a honeycomb suspension table, which is mounted on four vibration isolation legs. A programmable microprocessor-based controller synchronizes all the motions (direction, speed, increment, etc) of the 2-D stage. Stage location is continuously displayed as a front panel digital readout. The PAM signal is detected by a miniature microphone and lock-in amplifier. The lock-in amplifier is capable of detecting both the phase and the amplitude of the PAM signal. Scanning speed can be varied from 2.0 micron/sec to about 30 mm/sec. Finally, minimum increment is 2.0 microns for each axis.

Figure 17 shows that the x, y, and PAM detected analog signals are sent to the PAM data acquisition and color imaging system. This system includes Vector Graphics VSX-5000 dual (8 and 16 bit) microprocessor, 800K of 8 MHz RAM, 8087 math coprocessor, 12 bit data acquisition analog to digital (A/D) card, and a graphics card. The acquired data can be stored on a 36-megabyte hard disk, a 10-megabyte magnetic tape, or an 800K floppy disk. The digital image can be displayed on the green and color monitor concurrently, or a hard copy can be made on the eight-color plotter.

Digital Imaging Software

The data acquisition, imaging, and data analysis algorithms were developed in 8086 machine language at Allison and are menu driven. The hardware and software have the following features and capabilities:

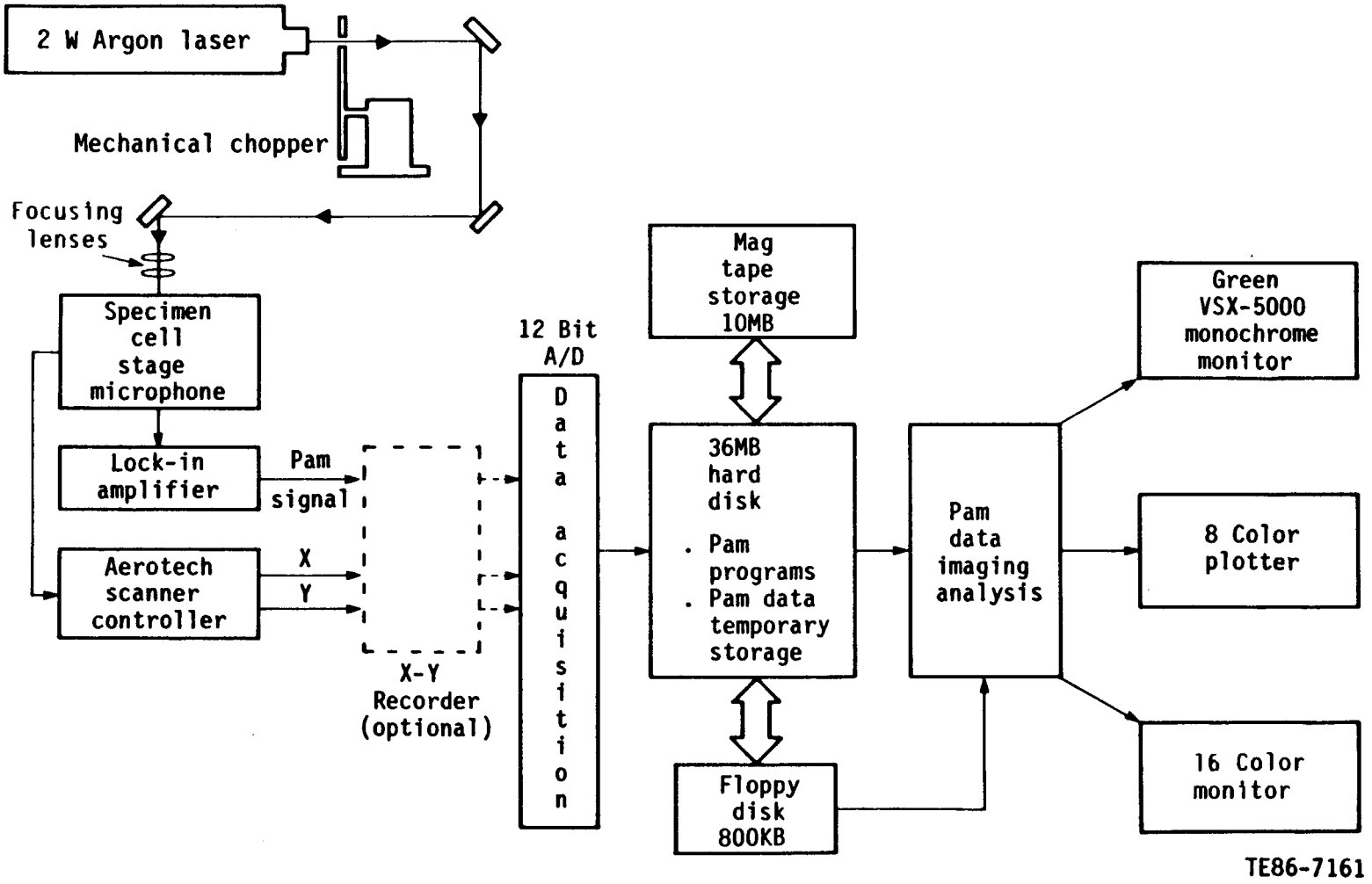

Figure 17. PAM flaw detection, data acquisition, and imaging system.

- o Acquisition and storage of data with 12 bit resolution.
- o Monochrome and color CRT display of images.
- o Eight-color hard copy plot--Three types of plots can be made of any PAM image acquired: continuous line plots, which are similar to the CRT image; analog signal plot simulating x-y recorder; and a histogram that reveals the distribution of PAM signals from the flaws.
- o Magnification--Four levels of magnification are available from 10x to 80x in multiples of 2, 4, and 8. With higher magnification one can accurately locate the flaw, size it, and determine the PAM signal.
- o Pan--The pan function allows scrolling up and down and side to side. This function is very useful in viewing areas of scans that may not be on the screen.
- o Flaw location--This function allows the placement of a flaw with specific coordinates at the center of the CRT screen at any time. This feature facilitates correlation of PAM detected flaws with fracture controlling defects in mechanical testing.
- o Flaw/PAM signal sizing--An ellipse or a rectangular shape can be created to size flaws. The ellipse or rectangle can be expanded and contracted in both the x-direction and y-direction for accurate sizing; the size of the rectangle or ellipse is displayed on the screen in real time. The maximum PAM signal from the flaw is detected along with its size. A hard copy of the flaw size and the PAM signal can then be obtained.
- o Thresholding--The raw digital image consists of an excessive number of PAM signals from small microstructure variations and flaws. Thresholds from 0 to 99% can be used to suppress the PAM signals from the raw image data for better flaw location and image penetration.
- o Hard copy--A hard copy of the data related to the test specimen can be made at any time during the viewing of a PAM image. The data include dimensions of the scan area, the speed of the scan, increment, sampling rate, magnification, threshold percentage, flaw location, size, and PAM signal. The distribution of PAM signals can be obtained also in a tabular form.

PAM Cell

Modular photoacoustic cells, as shown in Figure 18, were designed and fabricated for the characterization of the specimens in green, as-fired, and machined stages. Typically, the cell has three parts: (1) an aluminum outer

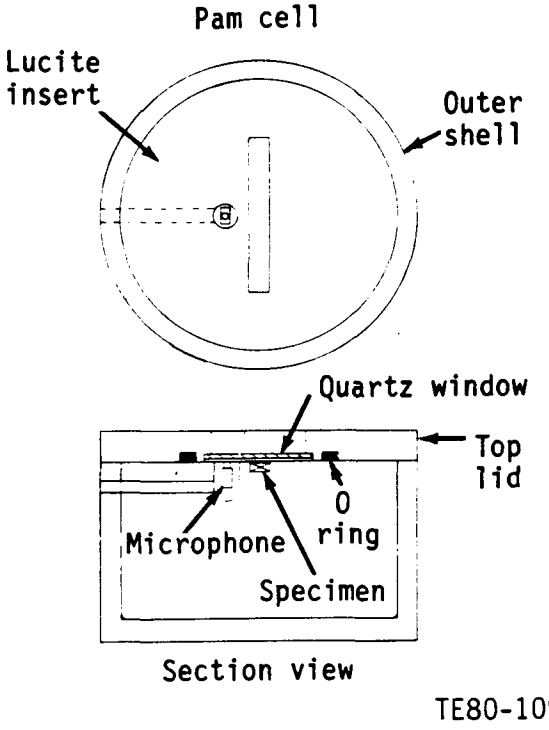

Figure 18. Schematic of photoacoustic cell for MOR specimen.

shell, (2) a Lucite insert with a cavity in which to place the MOR specimen, and (3) an aluminum lid with a window of optically polished fused silica. The lid is attached to the outer shell with three allen screws. An O-ring is used in the top lid to make an airtight seal, which prevents the loss of the photoacoustic signal. The air gap between the surface of the specimen and the window is about 0.5 mm. The total volume of the air within the cell is approximately 0.2 cm^3. The microphone is located in the insert.

Evaluation of Specimens

The procedure to characterize the green, as-fired, and machined specimens by photoacoustic microscopy was as follows: The specimen was placed in the gas-cell, and the Aerotech controller was programmed to raster scan the rectangular MOR bars in the x-direction and to increment in the y-direction to a predetermined surface area of the bar. The lock-in-amplifier parameters used were optimized on reference standard specimens.

The data acquisition program has five user inputs that synchronize the program with the controller: scanning speed, x travel distance, y travel distance,

sampling rate, and y increment. Other information, such as material description, specimen number, equipment settings, and specimen area inspected, is also input into the program. After all inputs have been completed, a file name is assigned and the data acquisition is initiated. All the x, y, and PAM digital data are temporarily stored on the hard disk. PAM digital images are then created and image processing is performed. The PAM digital data from each specimen is permanently stored on a magnetic tape or a floppy disk.

VII. RESULTS AND DISCUSSION

7.1 CHARACTERIZATION OF SILICON NITRIDE REFERENCE STANDARDS

Green Silicon Nitride

Photoacoustic microscopy and microradiography were used as an in-process nondestructive evaluation (NDE) technique to detect discrete flaws and microstructural modulations in green modulus of rupture (MOR) bars. Surface and subsurface hole reference specimens, Figure 3 and 4, were used to optimize the parameters to characterize the unknown green bars.

The top drilled hole specimen, Figure 3, was interrogated by microfocus x-ray at 80 KeV, 0.34 mA, and 100-sec film exposure at 5x magnification. The positive of the microradiograph, Figure 19, shows that seven holes were detected with x-ray thickness sensitivity of 2%. The smallest detected hole was 200 μm diameter and 106 μm deep. Hole no. 1 was undetected because of the irregular shape of the hole and the variable shallow depth of less than 50 μm which could not be measured by projection microradiography. The green specimens were evaluated at the above x-ray parameters.

All eight top drilled holes were detected by photoacoustic microscopy as shown in Figure 20. The smallest detected flaw was 106 μm in diameter. However, it was observed that the specimen was discolored in the scanned region and a thin, powder layer was deposited on the surface of the window glass. The discoloration varied across the length of the bar indicating nonuniform compaction and microstructural variability in the material.

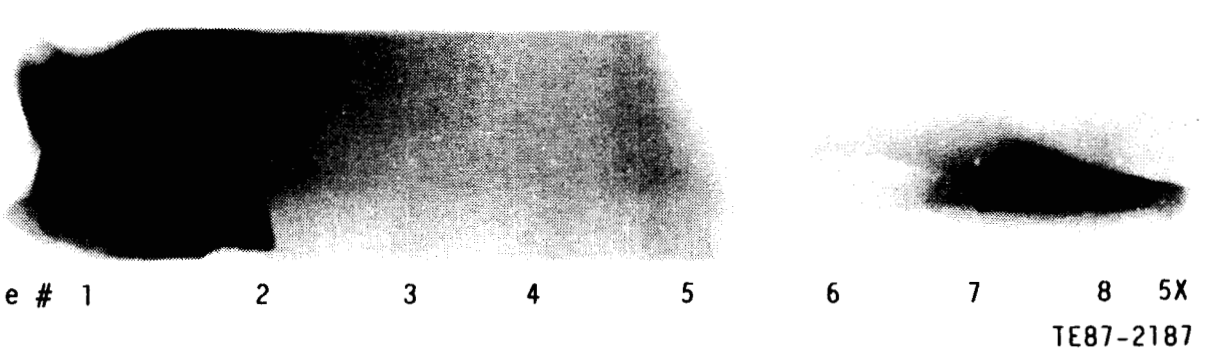

Figure 19. Detection of surface holes in green silicon nitride by projection microradiography.

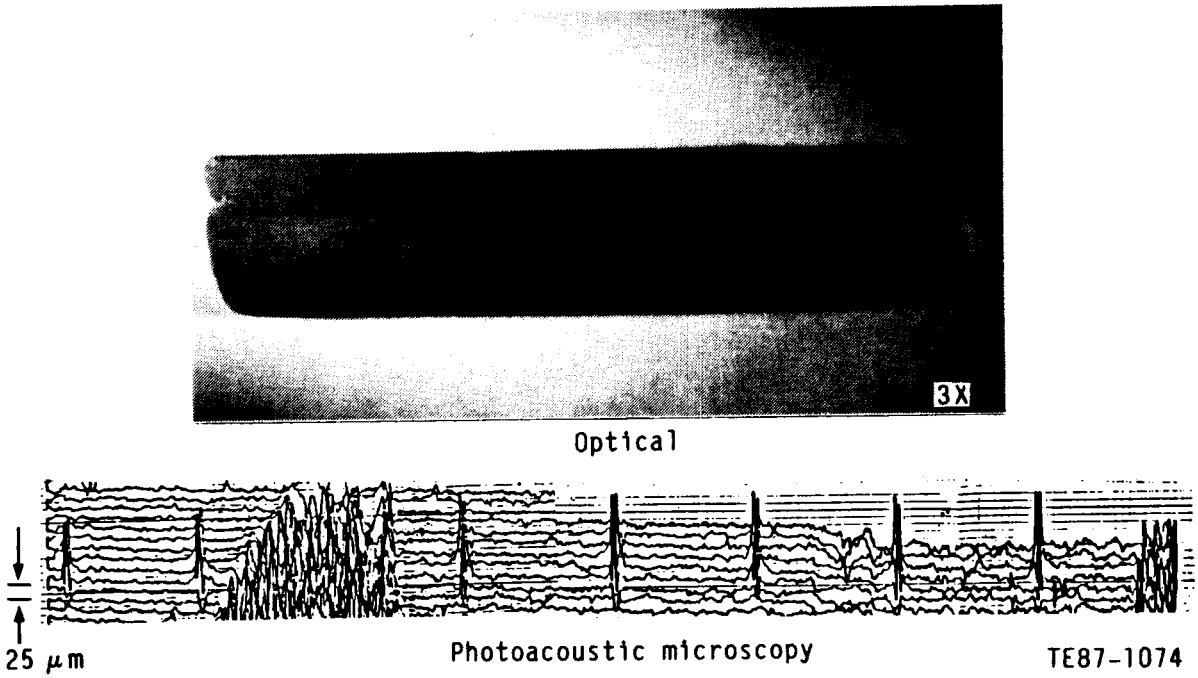

Figure 20. Detection of surface holes in green silicon nitride by photoacoustic microscopy.

A systematic parametric study was conducted to optimize the PAM experimental parameters for subsurface flaw detection and materials characterization. The side-drilled hole specimen shown in Figure 4 was examined by PAM at various experimental parameters as follows: laser power - 20 mW to 0.5 W; focal spot diameter (μm) - 25, 100, 200; modulation frequency - 40 Hz: lock-in amplifier sensitivity - 0.1 mV to 1.0 volt. The material volatilized and left a perman- ent hard discolored line on the specimen surface under all the experimental conditions as shown in Figure 21. A powder layer deposited on the cell window was readily removed by a finger without force. Material removal from the bar was attributed to the relatively open microstructure of the green body. The surface of the specimen hardened in the scanned area. The surface in the unscanned region could be scratched by a fingernail, but not in the scanned area. This suggests that the material structure was transformed and compacted near the surface by the focused laser beam resulting in permanent topographical change. No cracks were visible on the surface and none of the subsurface holes were detected.

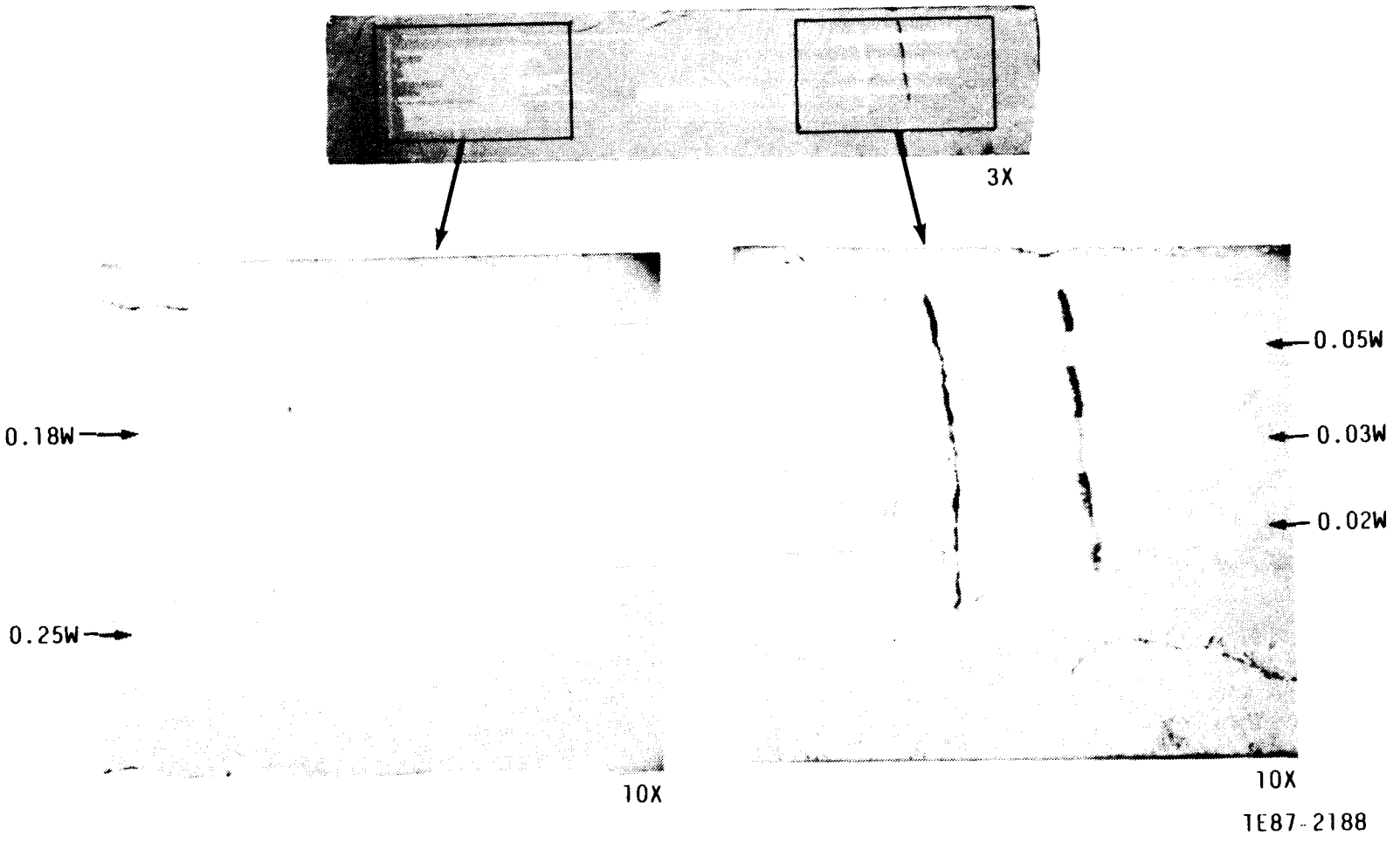

Figure 21. Effect of laser power on the surface of the green silicon nitride specimen.

The specimen was subsequently lightly ground using a 600 grit silicon carbide paper to decrease the hole depth from the top surface and further study the detectability of holes by PAM. The grinding operation did not affect the previously scanned area. Subsequently, sufficient manual pressure was applied during grinding for material removal in the scanned region. Table I shows the measured location of the holes after grinding. A variable amount of material was removed at each hole location because of the difficulty in the handling of the green bar during the grinding operation. The specimen was reexamined by PAM at a laser power of 0.5 W focused to 200 μm diameter at 40 Hz modulation frequency. None of the eight holes were detected in the phase detection mode. At 40 Hz, the thermal diffusion length (μ_s) is about 50 μm. The sensitivity in phase mode is generally about 2 μ_s. Even holes 50 μm deep were not observed, indicating that the thermal waves are highly dampened and significantly scattered even within 1.0 μ_s in green material. Both the material removal and rapid dampening of the thermal waves severely limits the use of photoacoustic microscopy as an in-process NDE tool to examine the subsurface structure of the material in the green state. The modifications in the surface topography also may be detrimental to the performance of the material after sintering.

Table I.
Green silicon nitride bar with side-drilled holes.

Hole No.	Location from top surface, μm measured after	
	Fabrication	Grinding
1	183	130
2	157	50
3	132	63
4	160	100
5	157	122
6	155	50
7	236	100
8	Specimen broke in transit	

Nominal distance between holes = 2.5 mm

A decision, based on the observations made on the reference standard specimens, was made to characterize only half the unknown green bars by PAM to study the effect of surface material removal on sintering. The PAM experimental parameters used were as follows: laser power--0.5W, scan speed--250 μm/sec, focal spot--200 μm, modulation frequency--40 Hz.

As-Fired Silicon Nitride

Flaw population and their characteristics are substantially altered on sintering a green compact to the as-fired state. Also, a sintered dense material has a different microstructure and properties. PAM parameters were optimized using the side drilled hole specimen shown in Figure 5 to determine the depth of penetration of thermal waves in as sintered material.

Figure 22 is a PAM line scan in the magnitude mode at 40 Hz that shows the 375 μm diameter 3.12 mm long subsurface side drilled holes were detected at least up to a depth of 547 μm with excellent signal-to-noise ratio (SNR). This depth is equivalent to 1.5 μ_s. Deeper holes were detected with poor SNR. Figure 23 shows PAM phase mode detection of side-drilled holes at 40 Hz. All of the eight holes were detected to a depth of 1014 μm. Phase reversal and interference were observed in the PAM signals from all the holes because of variable time delay interaction of thermal waves with the holes. The phase change and the corresponding signal from the simulated holes do not appear to have a good signal-to-noise ratio for reliable flaw detection and imaging even though material is being interrogated to larger subsurface depth. Comparison of Figures 22 and 23 show that SNR of the PAM signal in magnitude mode is much better than in phase mode for holes with depth up to 547 μm. The detectability of deeper holes appears to be similar in both magnitude and phase mode. Therefore, all the as-fired Si_3N_4 bars were characterized in the magnitude mode.

A seeded void specimen was examined by microradiography and PAM. Figure 24 shows that all nine seeded flaws were detected with x-ray thickness sensitivity of 2.5%. Optimum microradiographs were obtained at 93K_eV, 0.34mA and 100 sec film exposure. The smallest detected void was 150 μm. All the as-fired and machined bars were characterized at the aforementioned conditions. Photo

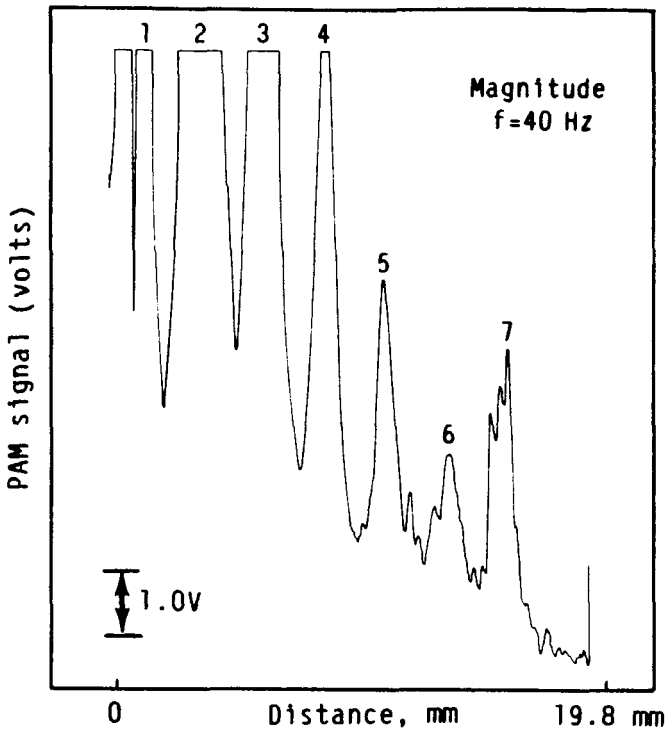

TE87-2189

Figure 22. PAM magnitude detection of side drilled holes in as-fired sintered silicon nitride.

acoustic microscopy did not detect any seeded voids because their size was much smaller and depth greater than one thermal diffusion length.

Machined Surface Specimens

Machining introduces surface flaws, e.g. cracks, and/or exposes subsurface flaws, e.g. voids, inclusions, and cracks in ceramic specimens. Simulated surface and subsurface flaws, Figures 5 to 11, and seeded specimens, including the one shown in Figure 12, were investigated to optimize PAM parameters to characterize machined specimens.

Surface Hole Detection and Resolution

Top drilled holes (TDH), shown in the specimen in Figure 8, were detected and spatially resolved at 40 Hz and 300 Hz chopping frequencies as shown in Figure 25, indicating that the surface resolution is controlled by laser focal spot size and not by the thermal diffusion length. Distance between holes 6 and 7 is about 8 μm suggesting that the laser spot size is less than 8 μm which is in good agreement with optically calculated spot size of 6.5 μm.

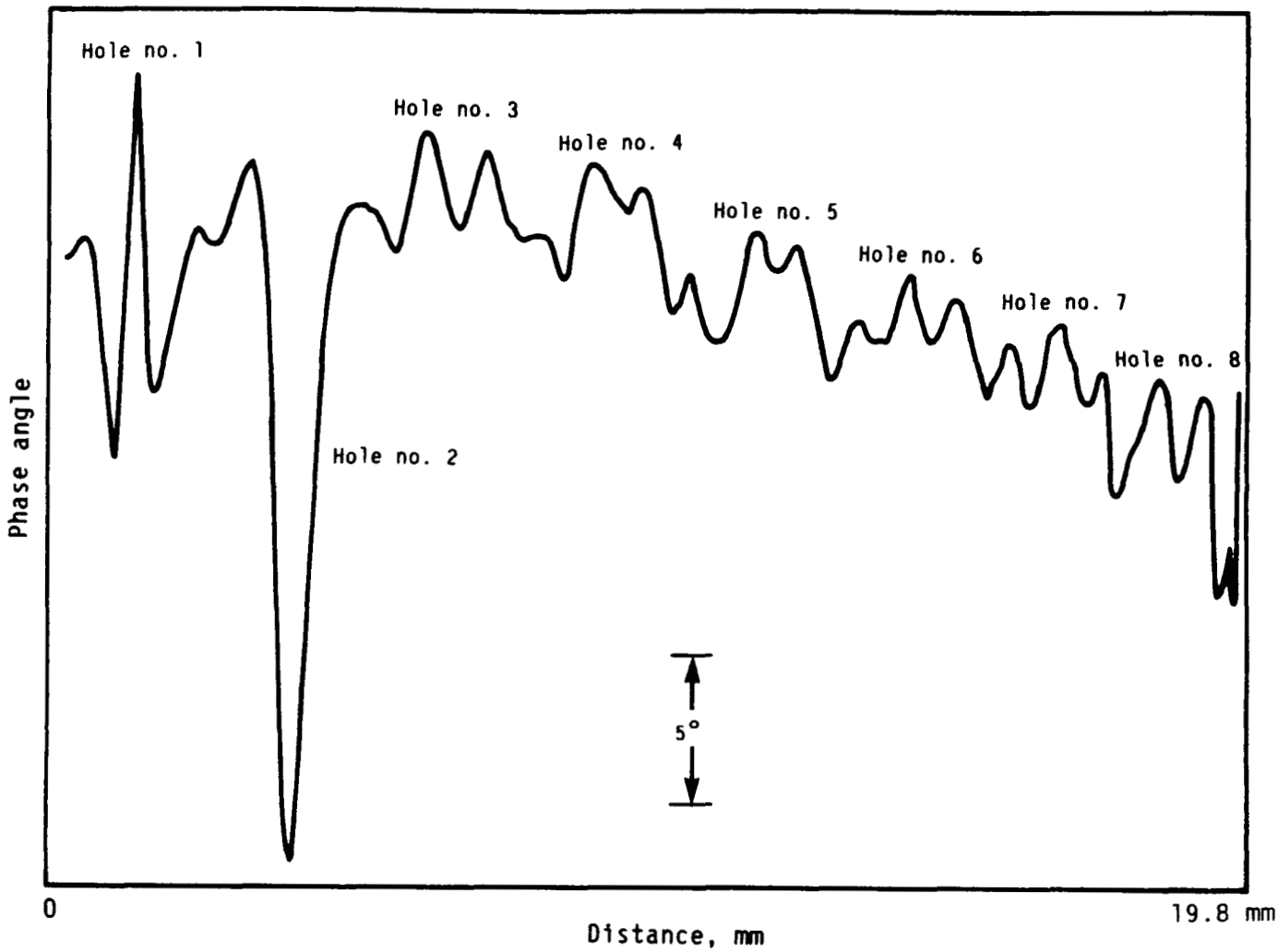

TE87-1075

Figure 23. PAM phase detection of side drilled holes in sintered Si_3N_4 at 40 Hz.

Figure 26 shows that PAM signal increases linearly when the hole depth (y) is less than or equal to about one thermal diffusion length (μ_s). At 40 Hz, μ_s = 400 μm. The signal from all the holes fall on a straight line since both the depth and diameter are less than or equal to 1.0 μ_s. At 300 Hz, μ_s = 140 μm. The signal initially varies linearly at approximately 1.0 μ_s for shallow holes (thermally thin condition) and subsequently yields the same PAM signal for all the deeper holes (thermally thick condition), clearly indicating that they behave like a crack of infinite depth (Ref 5). The thermal wave does not interact with the bottom of the deep holes but is scattered, reflected, and attenuated by the inner side walls of the hole.

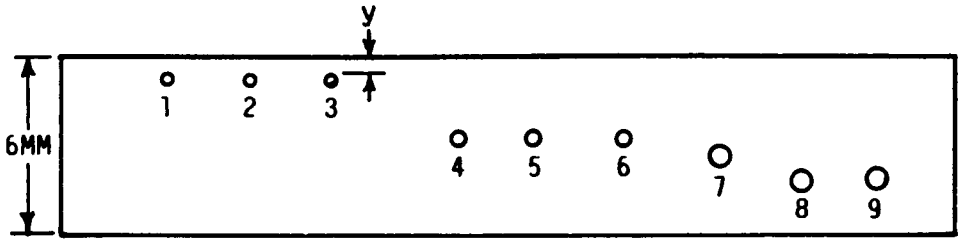

Flaw no	Detected Flaw size, μm	Location (y)	X-ray % sensitivity
1	150	550	2.5
2	150	500	2.5
3	150	500	2.5
4	200	1050	3.3
5	200	1100	3.3
6	200	1000	3.3
7	300	1400	5.0
8	300	1600	5.0
9	300	1600	5.0

TE87-1076

Figure 24. X-ray detection of internally seeded voids in as-fired sintered silicon nitride.

Figure 27 shows the actual and the PAM measured size of the holes in both the scanning and incremental directions. The specimen was scanned in the x-direction and incremented in the y-direction. It was observed that there is a linear correlation between the actual hole diameter and PAM measured diameter in both the scanning and incremental directions. The holes are oversized by an offset of about 50 μm in the x-direction, whereas they are correctly sized 1 to 1 in the incremental direction. The PAM measured apparent hole diameter in the x-direction is affected by the laser spot size, chopping frequency, and lock in amplifier parameters. The PAM measured dimensions in the y-direction are dominantly controlled by the resolution of the incremental indexing of the specimen (25 μm in the present case) and the laser spot size. The size of the flaw in the x-direction is $D_x = D_a + 50$ microns and in the y-direction by $D_y = D_a$, where D_a is the actual flaw diameter.

Figure 27 shows that the PAM measured hole depth appears to initially increase linearly to a hole depth up to about 140 μm and remains constant above it. This depth is equivalent to about 1.0 μ_s at 300 Hz. PAM signal also saturates, as shown in Figure 26, for holes deeper than about one thermal diffusion length. These results agree with Arnold and coworkers (Ref 11) who found that

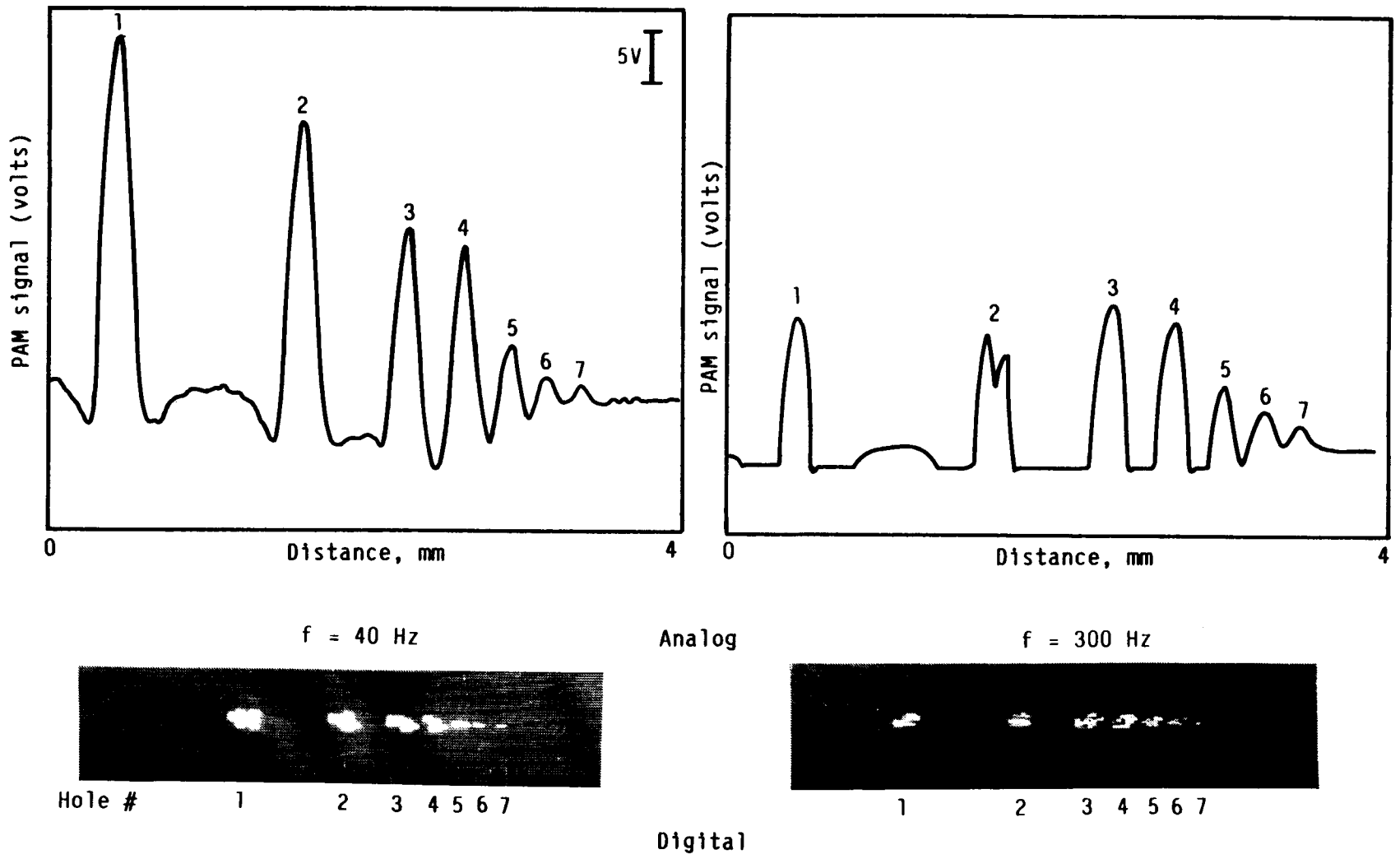

Figure 25. Detection and resolution of surface holes by photoacoustic microscopy.

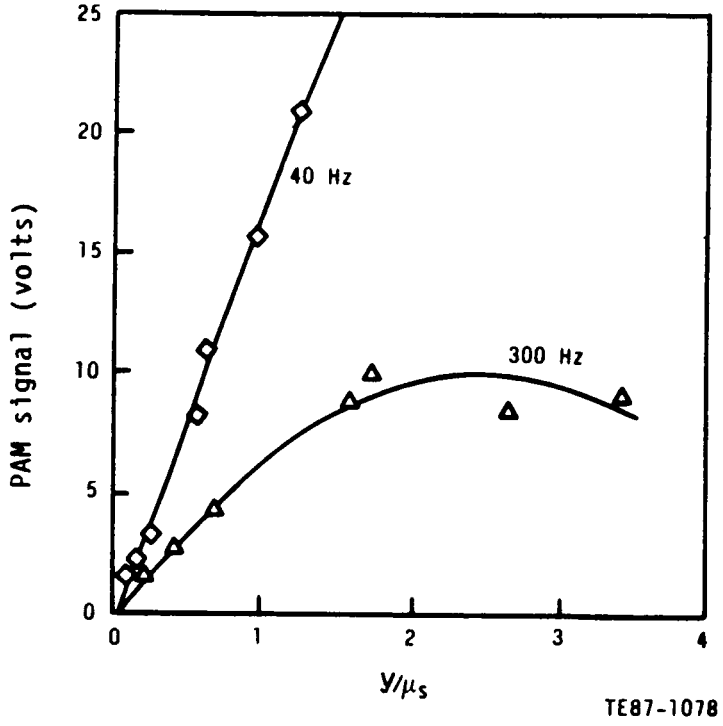

Figure 26. Effect of laser chopping frequency and depth on the magnitude of the PAM signal from the top drilled holes.

in the thermally thin condition, the PAM signal width in the x-direction is linearly proportional to the flaw depth. Holes up to 140 μm deep in this study are within the thermally thin region at the 300 Hz chopping frequency.

Subsurface Hole Detection and Resolution

Figure 28 shows that PAM can detect 441 μm diameter side drilled holes in machined silicon nitride specimen, as shown in Figure 6, up to a depth of 573 μm similar to as-fired material. Other flaws up to 1.1 mm diameter were not detected at a depth of 1.0 mm below the surface at 40 Hz.

A side-drilled hole specimen, as shown in Figure 7, was examined to determine the spatial subsurface resolution. Figure 29 shows that the four holes were detected both at 40 Hz and 300 Hz in the analog and digital PAM modes. The depth of the holes was between 88 to 132 μm. This depth is less than one half the thermal diffusion length (μ_s) at 40 Hz and less than or equal to 1.0 μ_s at 300 Hz. The distance between the holes at the modulation frequencies ranged between 1 to 5 μ_s at 300 Hz and from 0.3 to 1.5 μ_s at 40 Hz. Holes 132 μm apart could not be resolved but holes 345 μm apart, (approximately 1.0 μ_s), were spatially separated by PAM detection at 40 Hz.

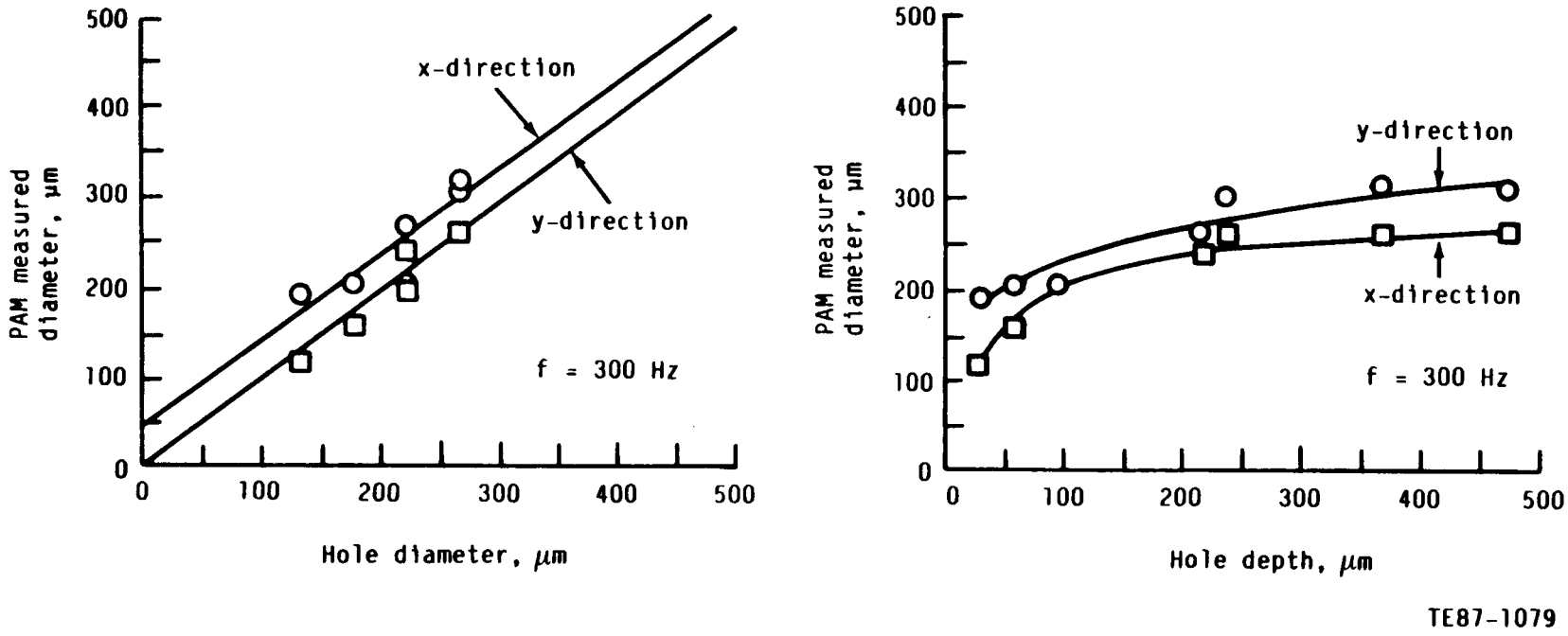

Figure 27. PAM measured dimensions of top drilled holes as a function of hole diameter and depth.

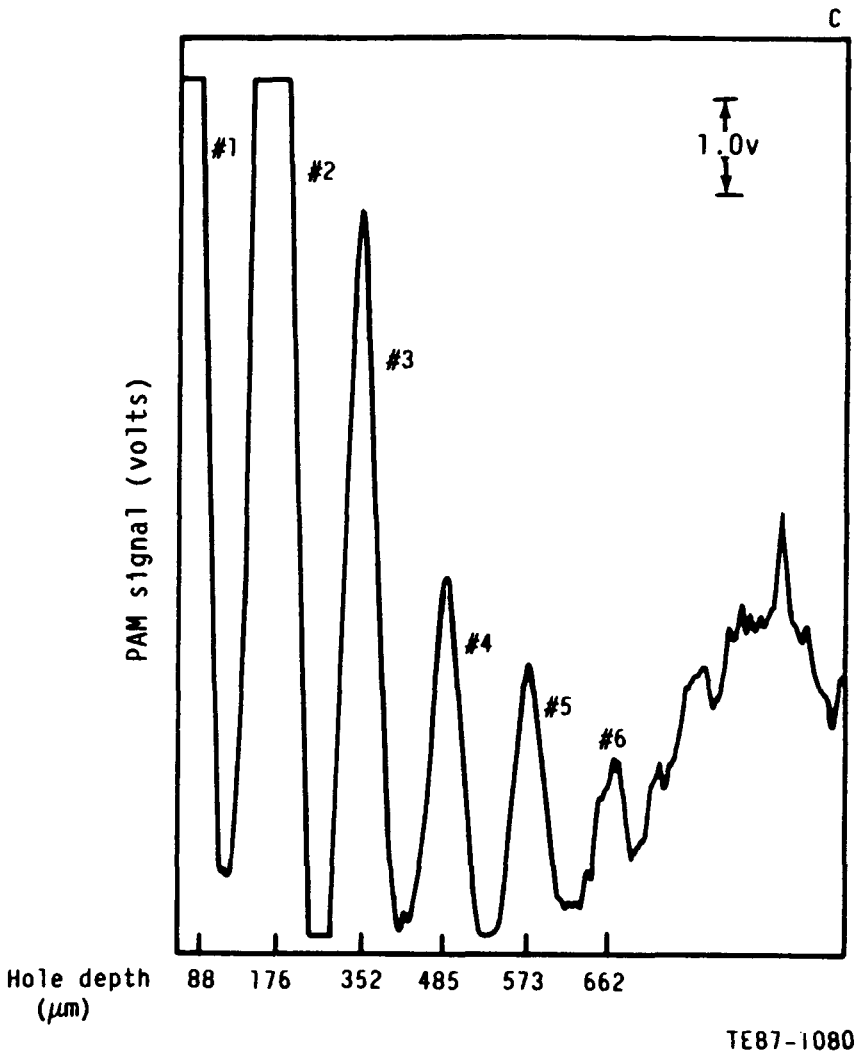

Figure 28. PAM detection of subsurface side-drilled holes in machined surface of sintered silicon nitride specimen at 40 Hz.

The digital image shows some overlapping of holes due to the rough side walls of the holes and other nonuniformities present as a result of the drilling operation. The diameter of the holes is 400 μm that is equal to 1.0 μ_s at 40 Hz, suggesting that the two defects one thermal diffusion length in size and apart (holes 2 and 3) can be detected and resolved. All the holes were detected and resolved (shown in Figure 29) at 300 Hz. The distance between holes no. 1 and no. 2 is 132 μm that is 1.0 μ_s at 300 Hz. It should be noted that these holes were not resolved at 40 Hz, revealing that subsurface resolution can be improved by increasing the modulation frequency. At higher frequencies, however, thermal wave penetration depth decreases rapidly because the waves attenuate exponentially.

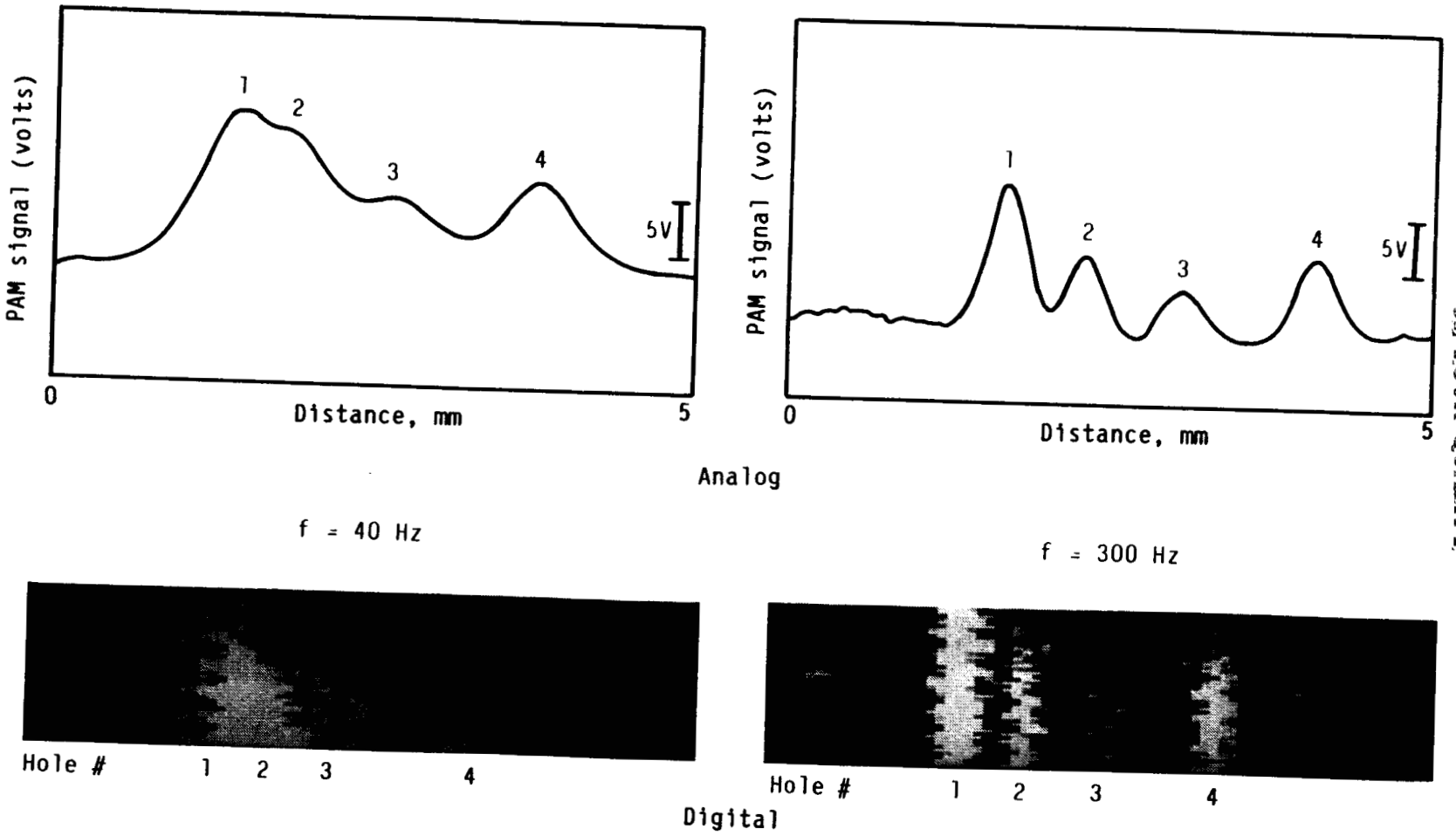

Figure 29. Detection and resolution of subsurface holes by photoacoustic microscopy.

Surface Crack Detection

PAM parameter optimization studies were conducted to detect tight surface cracks in hot pressed silicon nitride (NC132). Six cracks were induced by a diamond Knoop indentor, shown in Figure 10, on the polished surface of the specimen and the surface damage was not removed. Three PAM parameters, namely modulation frequency, scan speed, and sensitivity, were varied. Table II summarizes the signal-to-noise ratio of PAM signals from the cracks. All six simulated flaws were detected at 40 Hz and 50 μm/sec scan speed but only four were found at 250 μm/sec scan speed. The smallest detected crack at 50 μm/sec was 96 μm long x 48 μm deep and at 250 μm/sec was 205 μm long x 102 μm deep in size. Cracks no. 5 and no. 6 could not be discerned at 40 Hz and 250 μm/sec from the background signal because of the large number of naturally occurring defects of the similar size and/or orientation present in the specimen. Figure 30 shows that the 48 μm deep crack can be detected at 50 μm/sec but not at 250 μm/sec, clearly showing that shallow tight cracks cannot be discerned at rapid scanning speeds from the microstructural variations. Results at 300 Hz shown in Table II show that all six cracks were detected at 50 μm/sec but only five at 250 μm/sec. Furthermore, the signal-to-noise ratio of the PAM signal is better at the lock-in amplifier full scale sensitivity of 50 μV than at 200 μV at 250 μm/sec. The smallest detected crack was 140 μm long x 70 μm deep. Figure 31 shows the PAM detection of five tight surface cracks under optimum experimental conditions.

Simulated tight surface cracks in the machined surface of sintered silicon nitride, shown in Figure 9, were characterized by optimum PAM parameters. Figures 32 and 33 show that all of the eight as-indented cracks, four each of 143 μm (2 kg) and 234 μm (5 kg) length, were readily detected with signal-to-noise ratio of 1.9 and 2.3, respectively. The specimen was subsequently ground on 15 μm, 9 μm, and 3 μm, sequentially, diamond polishing paper and 5 μm material removed. The 2.0 Kg indentations could not be discerned from the surrounding microstructure and natural flaws. Figure 33 shows that the length (2c) of 5.0 Kg indentation decreased from 234 μm to 138 μm and all four cracks were detected by PAM with SNR of 1.5. The 5.0 Kg indentations could not be resolved by PAM after removing a total of 15 μm surface material. Obviously, the subsurface microfracture and the lateral cracks associated with the indentation responsible for the majority of the PAM signal are being

Table II.
Summary of signal-to-noise ratio for surface crack detection in HP Si_3N_4.

	Crack		40 Hz		300 Hz		
Crack #	Length (2c) μm	Depth (a) μm	50 μm/sec. 200 μV*	250 μm/sec. 200 μV	50 μm/sec. 200 μV	250 μm/sec 50 μV	250 μm/sec 200 μV
1	401	200	Saturated	Saturated	Saturated	Saturated	Saturated
2	323	162	7.75	9.0	13.5	13.5	11.5
3	234	117	6.75	2.0	5.5	4.5	3.0
4	205	102	8.75	3.0	4.0	5.5	2.5
5	140	70	3.75	N.D.	2.5	2.0	1.5
6	96	48	1.5	N.D.	1.1	N.D.	N.D.

N.D. - Signal-to-noise ratio of 1
Difficult to separate the flaw signal from the background

* - Signal from the flaws saturated the lock-in-amplifier at 50 μV.
Therefore, only 200 μV full-scale sensitivity was evaluated.

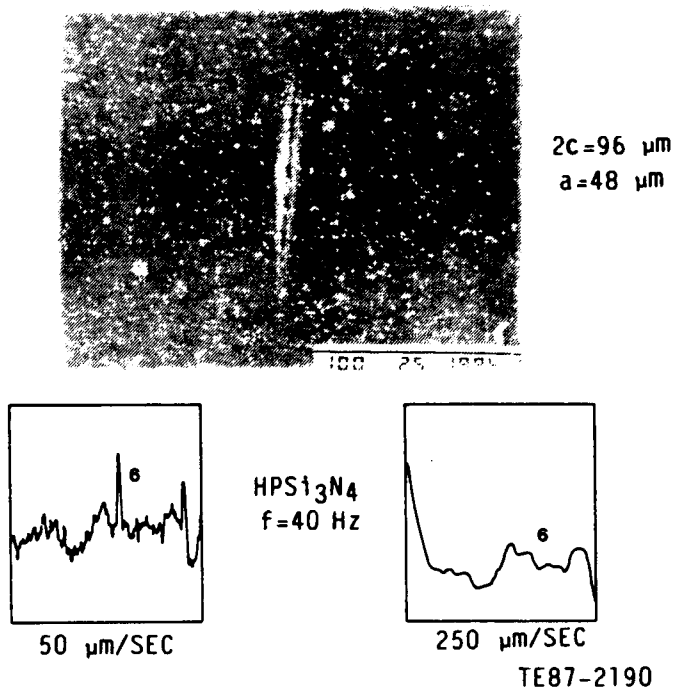

Figure 30. PAM detection of surface crack no. 6 in hot-pressed Si_3N_4.

eliminated during grinding, resulting in poor detectability of cracks. Figure 34 shows that the as-indented 2.0 and 5.0 Kg cracks were readily detected by PAM digital imaging.

Detection of Surface and Subsurface Seeded Voids

Surface and internal voids of 20 to 100 micron size, shown in Figure 35, were detected by microradiography and PAM (shown in Table III) in machined sintered silicon nitride. Microradiography detected 13 flaws both at 45 K_eV and 93 K_eV, shown in Table IV. However, both the contrast and detectability are better at lower voltage and larger magnification. At lower energy, soft long wavelength x-rays are generated which improve the subject contrast because of larger differences in the absorption coefficients of the host material and the flaw. Also, at larger magnifications the time of film exposure is longer in order to achieve the same film density. The visualization of the flaws smaller than 100 μm was much better at 20X than at 5X magnification. The smallest detected surface and internal void was 25 μm in size that corresponds to 1% x-ray thickness sensitivity.

Table III.
Detection of seeded voids in machined sintered silicon nitride.

Flaw No.	Flaw Location	Detected Flaw size (μm) PAM	X-ray	Optical
1	I	20	ND	-
2	I	40	ND	-
3	S	100	100	92
4	S	ND	40	30
5	I	100	100	-
6	I	70	ND	-
7	I	20	30	-
8	I	40	80	-
9	I	20	40	-
10	I	30	40	-
11	I	20	60	-
12	I	30	25	-
13	S	100	119	100
14	S	30	28	40
15	S	60	119	53
16	S	30	28	40

S - Surface
I - Internal
ND - Not detected

It is believed that flaws no. 1, no. 2, and no. 6 internal voids were not detected because the effective flaw dimension parallel to the x-ray beam propagation was much less than 25 μm.

Photoacoustic microscopy detected 20 μm to 100 μm size surface and internal voids as shown in Figure 36. The subsurface depth of all the internal voids is within 50 μm which is significantly less than the thermal diffusion length of 138 μm at 300 Hz. This image was made at 50% threshold. A large number of additional flaws were detected along with the known seeded flaws. Table V shows that less flaws were detected as the signal threshold is increased and vice-versa. At 20% threshold, sixteen flaws are detected whereas at 90% threshold, only five flaws are detected. In addition, 20 μm size flaws were visualized at 20% threshold but only 80 μm or bigger size flaws were observed at 90% threshold except the internal flaw no. 11 of 30 μm in size. This particular defect must be located very close to the surface and possess a well defined flaw boundary for thermal wave reflection and a large PAM signal.

Table IV.
Detection of seeded voids by microradiography.

Flaw no.	Flaw Location	45KV Exp. 550 sec Mag. 20X	0.20mA Exp 200 sec Mag. 5X	93KV Exp. 80 sec Mag. 20X	0.34mA Exp. 20 sec Mag. 5X
1	I	ND	ND	ND	ND
2	I	ND	ND	ND	ND
3	S	D	D	D	D
4	S	D	D	D	D
5	I	D	D	D	D
6	I	ND	ND	ND	ND
7	I	D	D	D	D
8	I	D	ND	D	D
9	I	D	ND	D	D
10	I	D	D	D	D
11	I	D	D	D	D
12	I	D	D	D	D
13	S	D	D	D	D
14	S	D	ND	D	D
15	S	D	D	D	D
16	S	D	D	D	ND

I - Internal
S - Surface
D - Detected
ND - Not detected

In general, at lower thresholds the PAM images were cluttered with signals of unseeded detected anomolies, microstructural variations, etc that caused severe difficulties in the interpretation of the PAM images. This is analogous to the detection and resolution of small flaws of similar size by ultrasonic and acoustic microscopy. PAM measured flaw size was smaller than or equal to the size determined from microradiography and optical micrography. This may be due to three reasons: (1) poor flaw boundary definition causing error in flaw size measurement; (2) effect of laser focal spot diameter and raster scan increment; and (3) three-dimensional nature and location of the flaw.

7.2 CHARACTERIZATION OF SILICON CARBIDE REFERENCE STANDARDS

The objective of this study was to ascertain the limit of subsurface thermal wave penetration and flaw detection in sintered silicon carbide. Figure 37

Table V.
Effect of PAM signal threshold on void detection.

Flaw no.	Flaw location	PAM flaw size (μm)	% threshold 20	50	75	90
1	I	20	D	D	ND	ND
2	I	40	D	D	ND	ND
3	S	100	D	D	D	D
4	S	ND	ND	ND	ND	ND
5	I	100	D	D	D	D
6	I	70	D	D	ND	ND
7	I	20	D	ND	ND	ND
8	I	40	D	D	D	ND
9	I	20	D	D	ND	ND
10	I	30	D	D	D	D
11	I	20	D	ND	ND	ND
12	I	30	D	D	ND	ND
13	S	100	D	D	D	D
14	S	30	D	D	ND	ND
15	S	60	D	D	ND	ND
16	S	30	D	D	ND	ND

S - surface
D - detected
ND - not detected

shows that all four holes 1.0 mm below the interrogating surface were detected at 40 Hz (μ_s = 685 μm) and 250 μm/sec both in the analog and digital imaging modes. The PAM signal increases exponentially with the hole diameter indicating that larger flaws or gross material variations may be discerned from the host material. The signal-to-noise ratio, however, decreases rapidly as the flaw size becomes smaller than the thermal diffusion length, resulting in poor discernability from the surrounding microstructure. Figure 38 shows the diameter and subsurface depth of the x-ray detected seeded voids in sintered silicon carbide. The smallest detected flaw was 180 μm in diameter that was equivalent to 5.2% x-ray thickness sensitivity. PAM detected 450 μm diameter voids at 270 μm depth below the interrogating surface, as shown in Figure 39. This depth was equivalent to 0.4 μ_s at f_c = 40 Hz. Other seeded voids were much deeper and smaller in size than 1.0 μ_s and could not be detected by PAM.

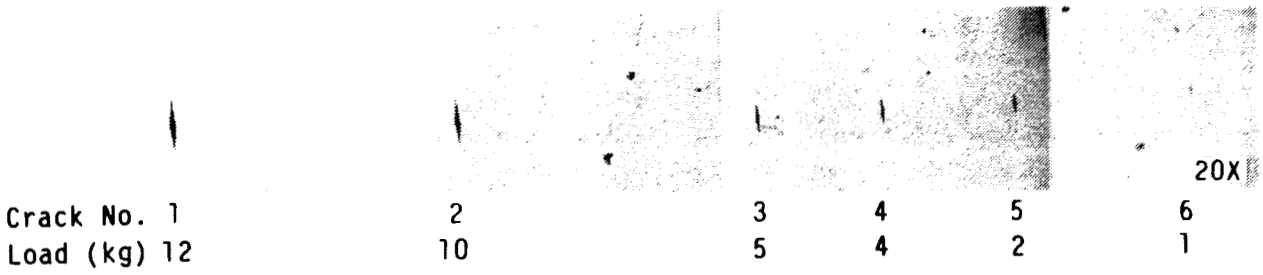

Optical

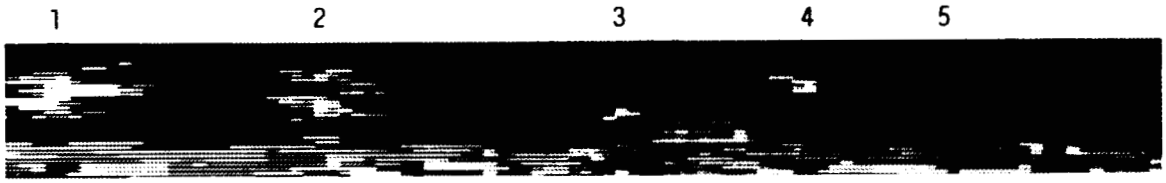

300 Hz
Digital image

Analog

TE87-1082

Figure 31. PAM detection of surface cracks in hot-pressed silicon nitride (NC132). Separate scans were made across the middle of each indentation.

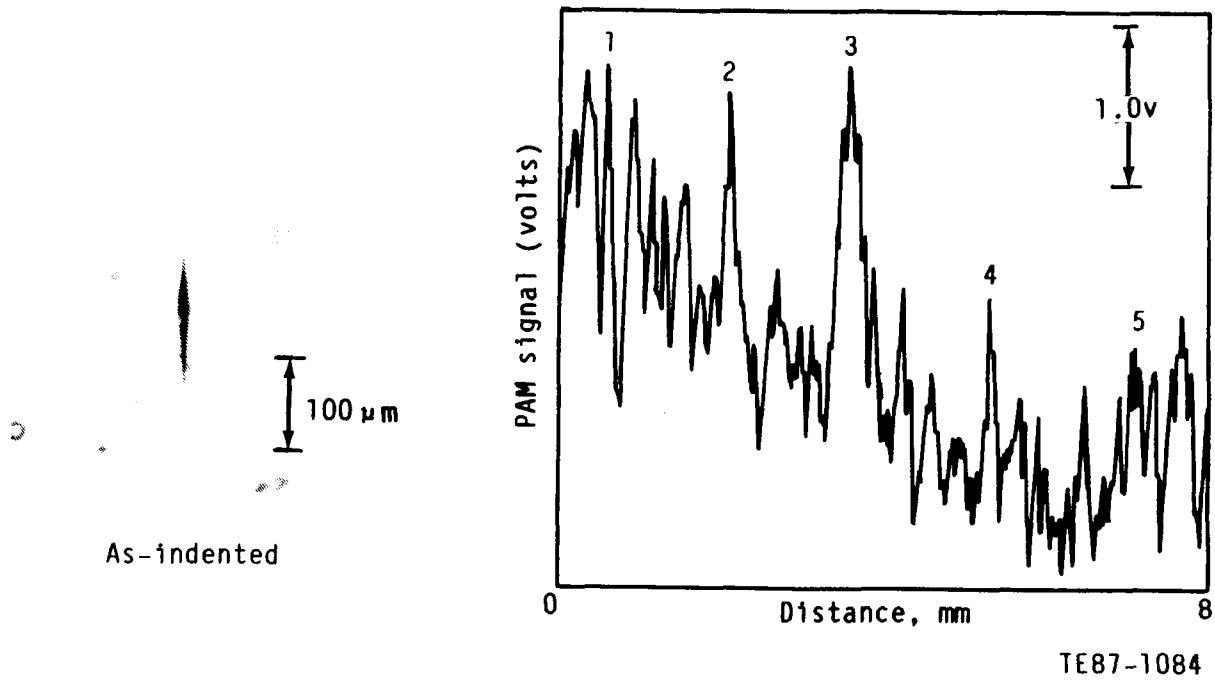

Figure 32. PAM detection of 2.0 Kg Knoop indentations in the machined surface of sintered silicon nitride.

It is concluded that 250 µm diameter side drilled holes can be detected 1.0 mm below the interrogating surface in sintered silicon carbide. However, spherical seeded voids of 450 µm diameter were only detected up to 270 µm depth below the interrogating surface indicating that flaw characteristics have a significant affect on subsurface flaw detectability.

7.3 NONDESTRUCTIVE EVALUATION OF GREEN SPECIMENS

Forty-five bars were characterized by visual inspection and microfocus x-ray. Results of the visual examination (10-30X) revealed the presence of chips (corner and edge), holes, cracks, and mounds of extra material over the specimen surface. X-radiography examination of the specimens detected inclusions in some specimens.

Twenty-three bars were photoacoustically examined. The photoacoustic examination resulted in material removal, discoloration, and surface hardening. The remaining specimens were not characterized by PAM to compare the effect of the above surface changes on the sintering behavior of the material. In general, the microstructure of the bars produced large PAM signals. Some discrete flaws

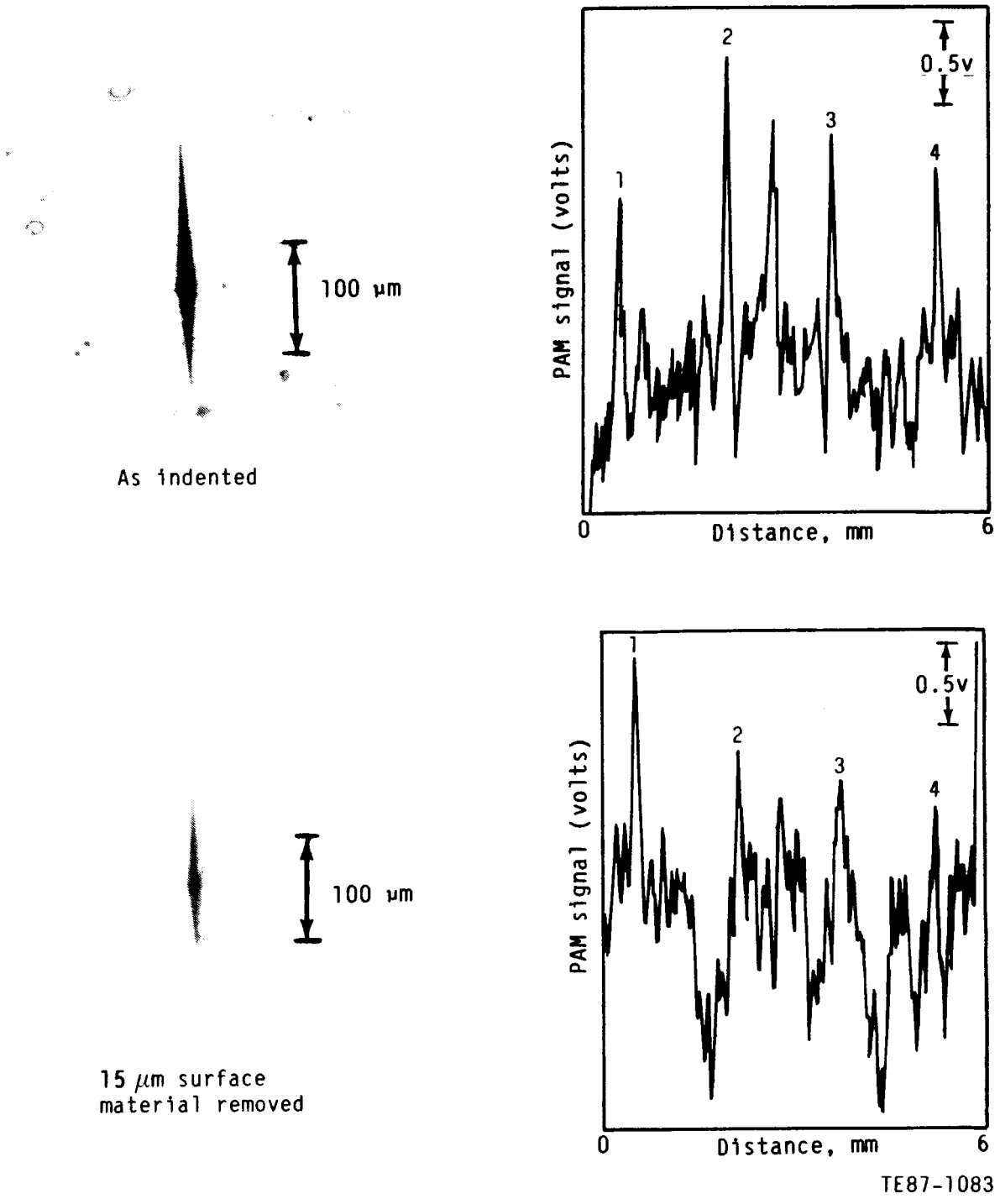

Figure 33. PAM detection of 5.0 Kg Knoop indentations in the machined surface of sintered silicon nitride.

TE87-1085

Figure 34. PAM digital image of as-indented Knoop cracks in the machined surface of sintered silicon nitride.

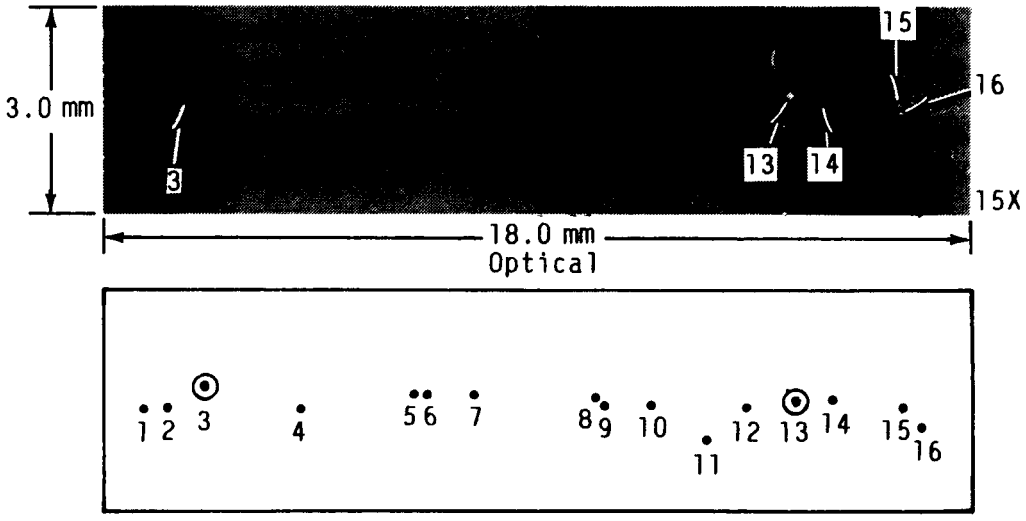

TE87-1086

Figure 35. Layout of seeded voids in machined sintered silicon nitride.

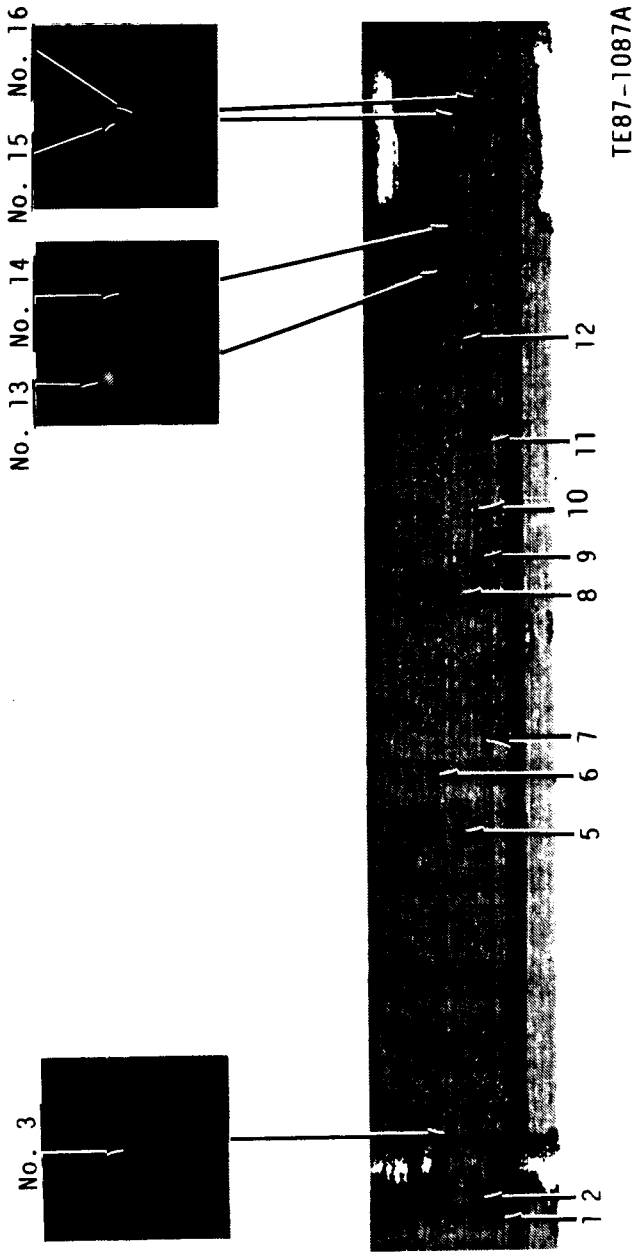

Figure 36. PAM detection of seeded voids in sintered silicon nitride.

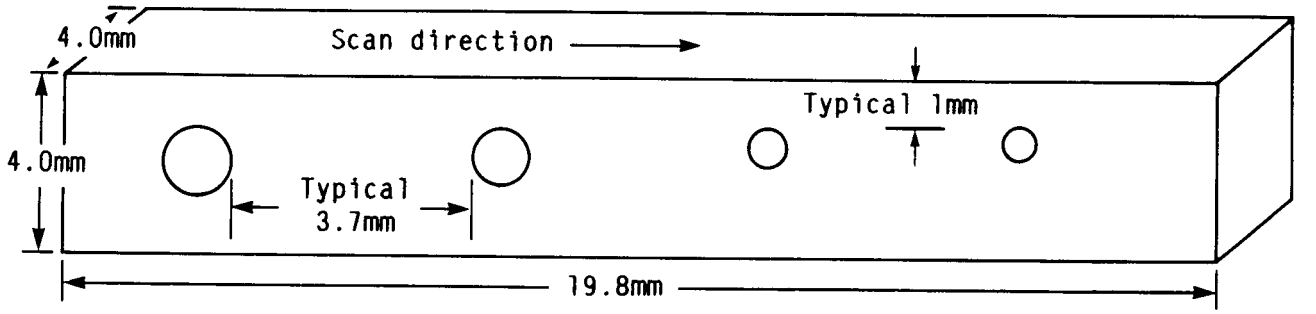

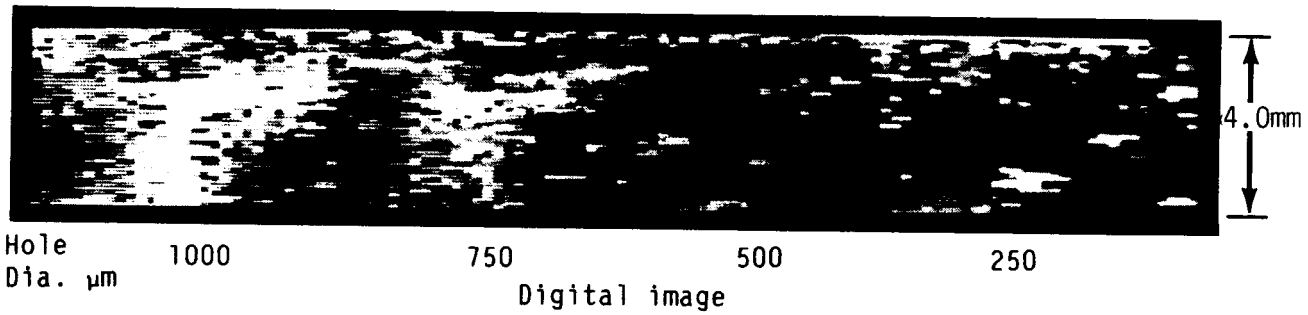

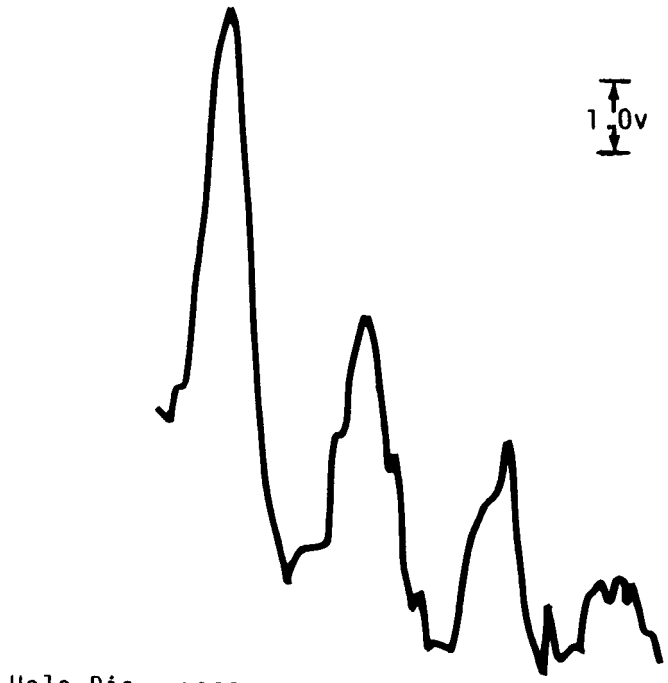

TE87-1088

Figure 37. PAM detection of subsurface side-drilled holes at 1.0 mm below the interrogating surface in sintered silicon carbide as-fired specimen.

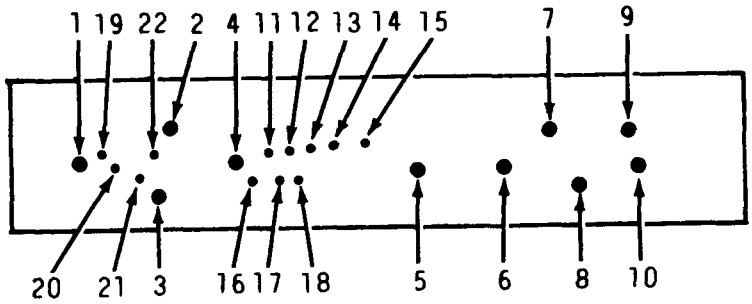

Flaw #	Flaw Dimensions, μm Diameter	Depth	X-ray Detection
1	451	270	D
2	451	270	D
3	451	270	D
4	451	812	D
5	451	812	D
6	451	1263	D
7	451	1263	D
8	451	1173	D
9	451	1263	D
10	451	1263	D
11	270	812	D
12	270	812	D
13	270	722	D
14	270	722	D
15	270	722	D
16	270	722	D
17	270	722	D
18	270	722	D
19	180	-	D
20	180	-	D
21	180	-	D
22	180	-	D

D-Detected TE87-1089

Figure 38. Detection of seeded voids in sintered silicon carbide by microradiography.

were also detected. An excessive amount of material was removed from the specimen surfaces and the topography of the scanned region varied significantly between specimens, indicating variability in the material microstructure.

7.4 NONDESTRUCTIVE EVALUATION OF AS-FIRED SPECIMENS

Forty-four sintered bars were characterized by visual inspection and microfocus radiography. Results of the visual examination revealed the presence of chips and excessive mounds of material over the specimen surface. Minute cracks were observed on the surface in the area where the green bars were examined by PAM and material volatilized prior to sintering. Some bars showed no cracking, as shown in Figure 40, while others had excessive cracking, as shown in Figure 41. The crack lines and spacing between the lines occurred due to raster and incremental scanning in the green state. Nonuniform shrinkage and stresses on sintering opened the shallow cracks. The cracks were generally oriented

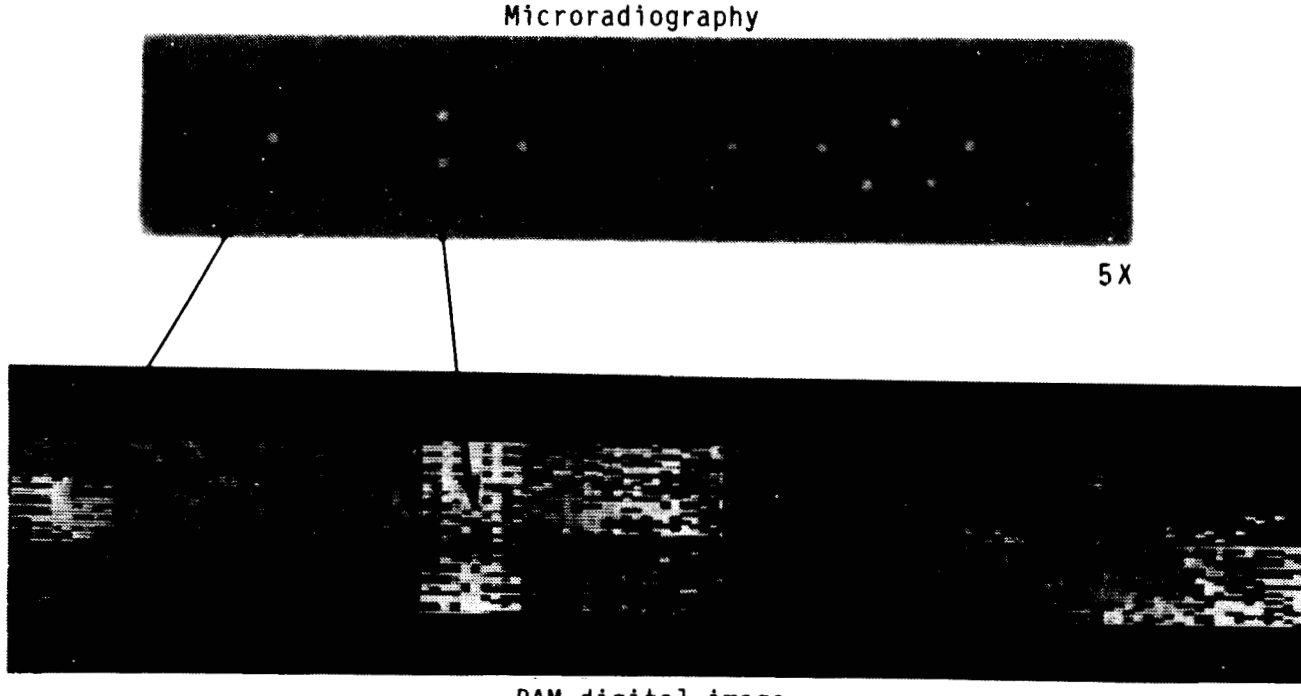

Figure 39. Detection of subsurface seeds voids in as-fired sintered silicon carbide.

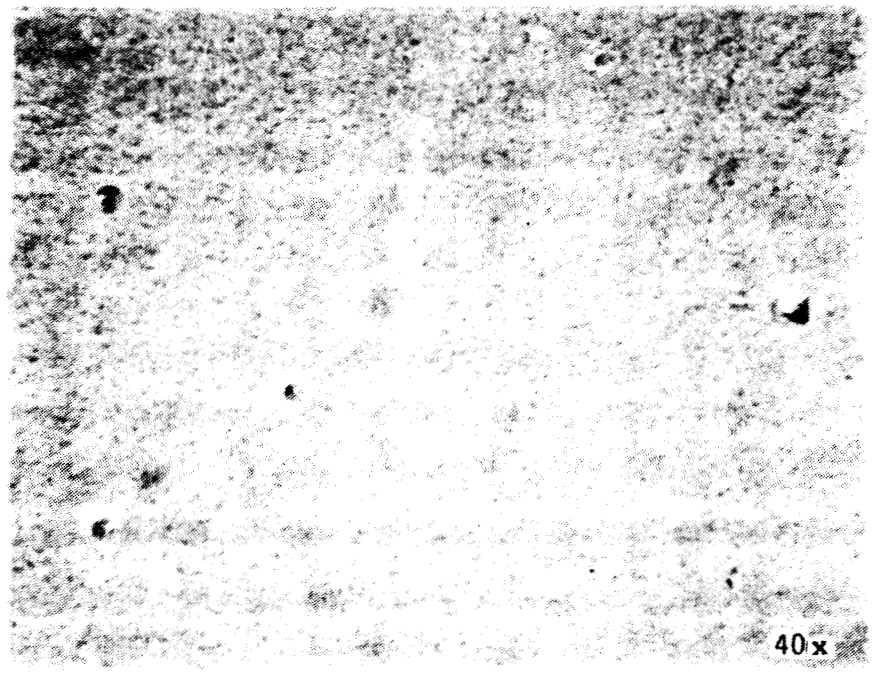

Figure 40. PAM scanned region of specimen no. A32 of silicon nitride after sintering.

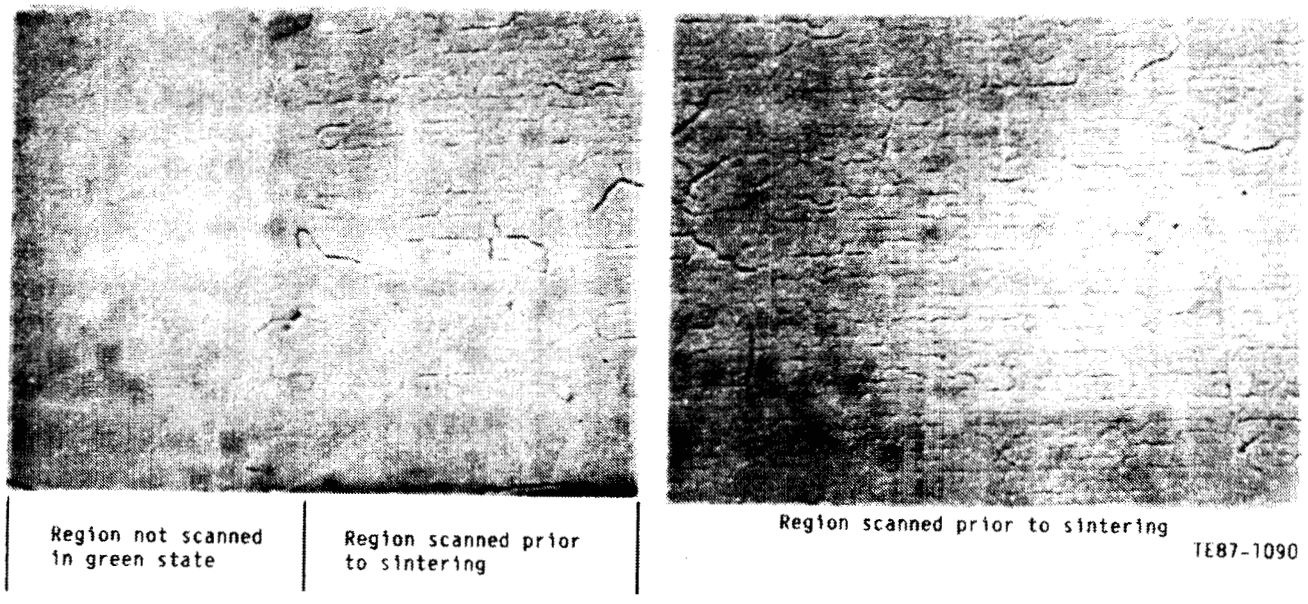

Figure 41. PAM scanned and unscanned region of a sintered silicon nitride specimen (no. A1).

parallel to the scanning and stressing direction in flexural testing. The cracks will be eliminated during machining and are not expected to have any detrimental affect on the strength. X-radiography examination detected density variations reflecting the effect of extra mounds of material.

Two surfaces of each bar were evaluated using optimized PAM parameters. The PAM digital image of all the specimens revealed large number of flaws even after 50% signal thresholding. The as-fired surface had an excessive amount of mounds of material that significantly affected the PAM signal. No correlation between the PAM data and optical data was observed.

7.5 NONDESTRUCTIVE EVALUATION OF MACHINED SPECIMENS

Machining of ceramic materials removes a large number of flaws from the as-fired surface and introduces new surface flaws and/or exposes subsurface flaws in MOR specimens. These flaws could be voids, inclusions, and machining damage as tight surface cracks. Machined specimens were characterized by ultrasonic velocity, fluorescent penetrant, visual inspection, microfocus radiography,

ultrasonic C-scan imaging, and photoacoustic microscopy to detect critical failure controlling flaws.

Table VI shows the measured dimensions, density, and ultrasonic wave velocity. The average longitudinal wave velocity was 10,726 meters/sec and shear wave velocity was 6,010 meters/sec. The Poisson's ratio using equation (4) was calculated to be 0.271. These measurements are consistent with the properties of the commercially available sintered silicon nitride materials. The fluorescent penetrant inspection (FPI) and visual examination revealed similar kinds of microscopic distribution of scattered surface porosity over the surface area of the bars. Also, about 75% of the specimens had one surface (length x width) with less natural flaws compared with the opposite surface. The surface with the least number of flaw indications was selected for ultrasonic and photoacoustic evaluation as shown in Table VII. The same surface was put in tension during subsequent flexural testing. Optical micrographs (7X) of the selected surface of each specimen is shown in Appendix I. Machining marks parallel to the specimen length and white specular areas, shown in Figure 42A, were present over the specimen surfaces and could not be removed by ultrasonic cleaning in acetone. In addition, randomly distributed pores of 30 to 70 microns in size were observed, shown in Figure 42B, in some specimens largely outside the PAM scanning region. The as-fired specimens were machined. Therefore, it is believed that microporosity must be present through the thickness of the specimens which must have resulted because of poor quality raw materials and/or inadequate process control. The entire surface area within the two black lines on each photograph in Appendix I up to the beveled edge was characterized by PAM.

Table VI.
Measurement of properties of machined sintered Si_3N_4.

	Average	Standard deviation
Length, cm (in.)	2.9812 (1.174)	0.0105 (0.004)
Width, cm (in.)	0.5598 (0.220)	0.0015 (0.0006)
Thickness, cm (in.)	0.2771 (0.109)	0.0008 (0.0003)
Density, gms/cc	3.243	0.0182
Velocity, meters/sec		
Longitudinal	10,726	48
Shear	6,010	30
Poisson's ratio	0.271	

Table VII.
Selection of machined specimen surfaces for nondestructive evaluation characterization.

Specimen no.	Surface selected	Specimen no.	Surface selected
A2	μ-structure* analysis	A29	B
A4	Ref standard*	A30	T
A5	T	A31	T
A6	T	A32	T
A7	T	A33	B
A8	T	A34	T
A9	Ref standard*	A35	Ref standard*
A10	T	A37	T
A12	T	A38	B
A13	T	A39	B
A14	B	A41	B
A15	B	A42	B
A16	B	A43	T
A17	T	A46	T
A18	T	A47	T
A20	T	A51	T
A21	T	A54	T
A22	T	A55	T
A23	B	A57	T
A25	Ref standard*	A58	T
A26	T	A59	T
A27	B	A65	T

T--top surface
B--bottom surface
*These specimens were used to fabricate reference standards for PAM parameter optimization studies or microstructure analysis.

Microradiography revealed (as shown in Table VIII) pores, high density inclusions, and scattered low density variations. Iron impurity in the starting powder was probably responsible for the presence of most of the inclusions. The low density variations were generally outside the 19.0 mm outer span region of the 4 point loading positions of the MOR bar, and in general, correlated qualitatively with the porosity distribution observed in FPI and visual and optical examinations. Individual flaws were detected in 12 specimens within the 9.53 mm inner span of the 4 point flexural test specimen. The measured diameter of the smallest flaw was 50 μm which is equivalent to 1.8% of x-ray thickness sensitivity. The radiography data does not contain information regarding the location of the defects relative to the tensile surface of the bend test specimens.

Table VIII.
Flaw detection by microradiography in machined sintered silicon nitride.

Spec no.	Description of flaw detection
A2, A5, A6	No flaw detected
A7	Incl, OS, 50 μm diameter
A8, A9, A10	No flaw detected
A12	Incl, OS, 200 μm x 100 μm
A13	Incl, IS, 50 μm diameter
A14	3 Incls; 2 - 200 μm diameter, IS; 1 - 50 μm dia, OS
A15, A16, A17, A18, A20, A21, A22, A23, A15, A26	No flaw detected
A27	Scattered low density variations pore, IS, 100 μm x 150 μm
A29	2 Incls; 200 μm dia, OS; 50 μm x 100 μm, IS
A30	No flaw detected
A31	Pore, IS, 50 μm dia
A32	Scattered low density variations
A33	Incl, IS, 200 μm dia
A34	Pore, IS, 50 μm x 100 μm
A35	Scattered low density variations
A37	No flaw detected
A38	Incl, IS, 50 μm x 100 μm
A39, A41, A42	No flaw detected
A43	Incl, IS, 50 μm x 100 μm
A46, A47	No flaw detected
A51	Scattered low density variations--pore, IS, 100 μm x 200 μm
A54	Incl, IS, 50 μm x 100 μm
A55, A57	Scattered low density variations, OS
A58	Scattered low density variations, OS--pore, IS, 75 μm dia
A59, A65	Scattered low density variations, OS

Incl--High density inclusion
IS--inside the 9.53 mm inner span of the 4 point loading positions
OS--outside the 9.53 mm inner span of the 4 point loading positions

---

Figure 43 shows that seven natural and simulated surface voids in a sintered silicon carbide reference standard were detected by ultrasonic C-scan imaging. Table IX shows the measured flaw sizes by optical micrography (50 to 200X) and acoustic grey scale images. The smallest simulated hole was 38 μm deep and clearly shows that shallow surface flaws can be resolved from the surface topographical variations. The smallest detected natural surface pore was 40 μm x 64 μm in size measured in the plane of the surface. Grey scale modulations in the ultrasonic image were observed across the surface of the specimen, indicating that subtle, less definitive microstructural changes and flaws com-

Table IX.
Comparison of optical and ultrasonic measured surface pore size.

Flaw no.	Type of pore	Optical flaw size--μm			Ultrasonic flaw size--μm	
		Direction x	Direction y	Depth	Direction x	Direction y
1	Simulated	468	468	113	505	577
2	Natural	40	64	--	108	144
3	Natural	103	120	--	144	180
4	Simulated	238	238	89	253	289
5	Natural	40	95	--	108	144
6	Natural	71	95	--	144	144
7	Simulated	159	159	38	216	216

pared to the aforementioned defect were being detected. Optical examination showed random distribution of a large number of very small pores on the surface but no correlation with the C-scan image was possible. The larger flaw size determined from the acoustic images, as shown in Table IX, compared to the optical images is predominantly affected by the transducer focal spot diameter that is about 144 μm. The reference standard specimen was imaged by ultrasonic with all the unknown specimens to ascertain the repeatability of surface flaw detection. Ultrasonics detected surface machining marks, discrete flaws, and other surface anomolies in the machined silicon nitride specimens. For example, Figure 44A shows that the grey scale variation in the C-scan image is due to the machining marks. Figure 44B reveals detection of discrete surface pore and grey scale variations due to scattered porosity of 30 to 70 micron in size on the surface .

Photoacoustic examination of the selected tensile surface of the specimens was conducted using the optimized experimental parameters for the detection of tight surface crack and internal/surface voids of 20 to 30 μm size in machined sintered silicon nitride reference standards using these conditions. The total surface area of 75.5 sq cm, 15.4 cm length, and 4.9 cm width of each specimen was characterized by PAM and the digital image data accumulated on a floppy disk. The analysis of the PAM images revealed that photoacoustic microscopy is an extremely sensitive technique which detects minute microstructural variations. The PAM raw data image had an excessive number of low level random signals that resulted in an extremely cluttered picture. Discrete flaw visualization, resolution, and quantification required signal thresholding

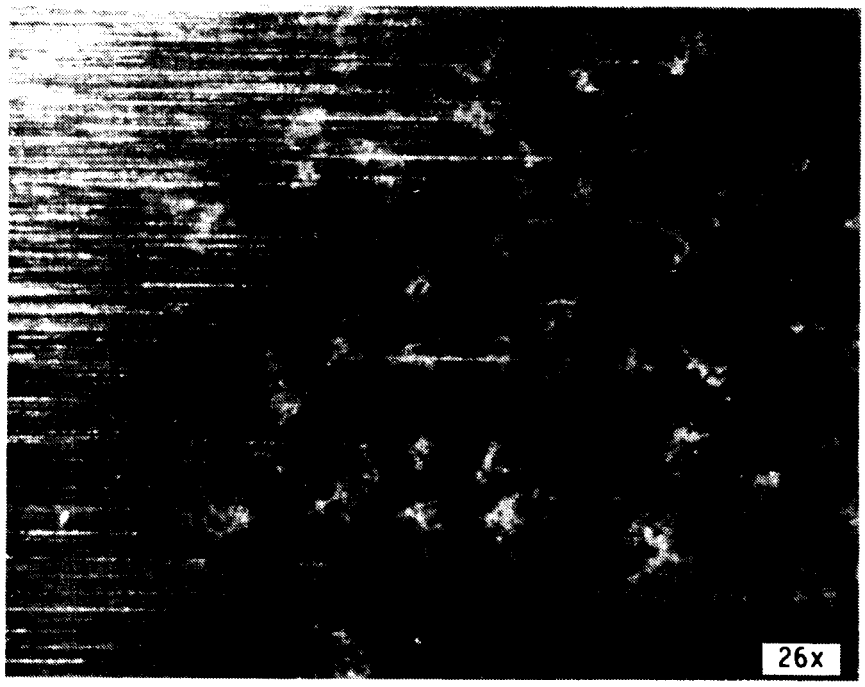

(A)

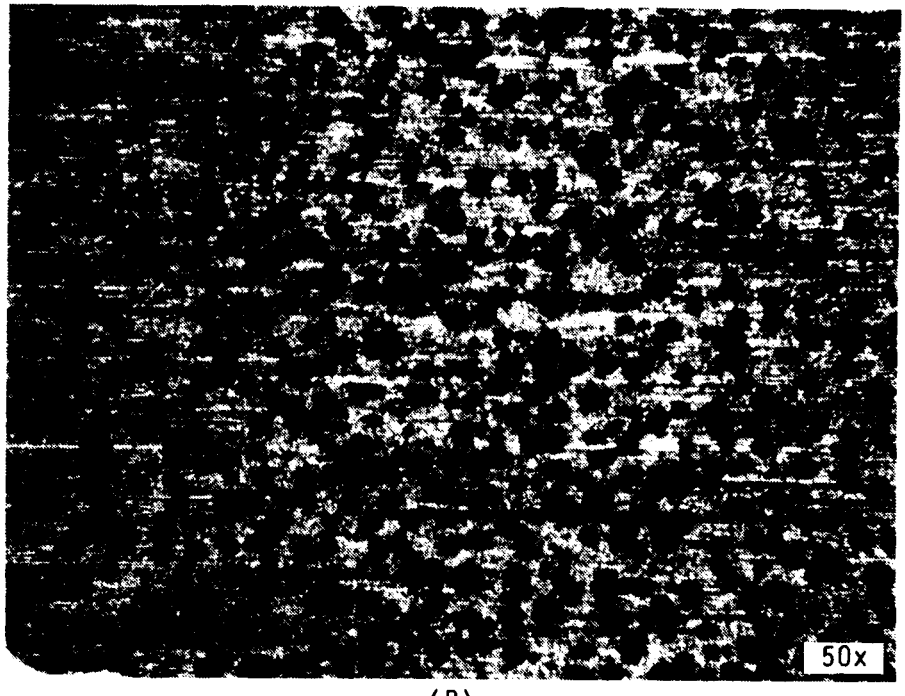

(B)

TE87-2232

Figure 42. (A) Machining marks and white surface area. (B) Scattered surface porosity.

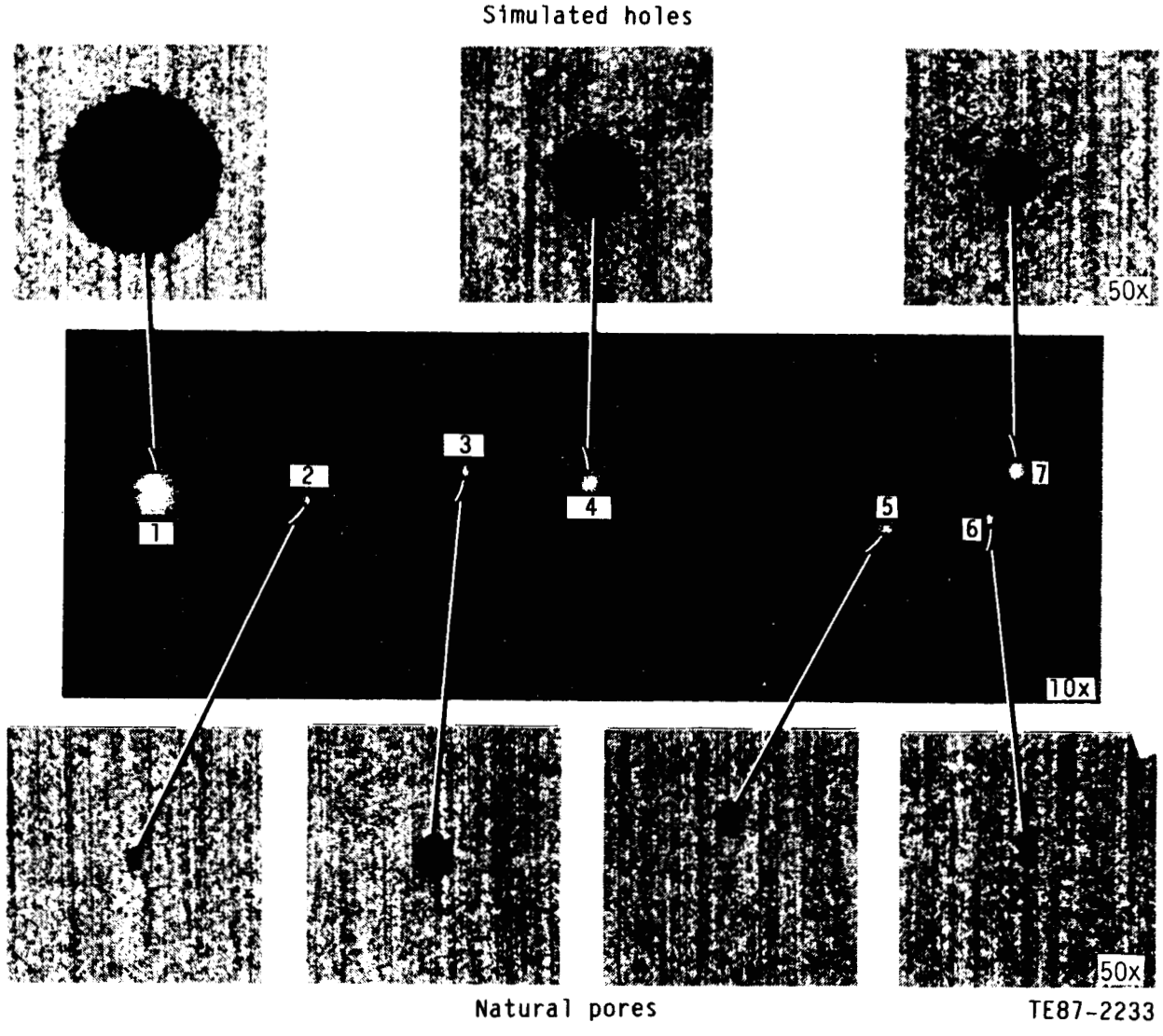

Figure 43. Ultrasonic surface flaw detection in sintered silicon carbide reference standard.

(suppression or subtraction) and magnification of the image. Many flaws of various shapes and dimensions were detected in each specimen; therefore, apriori identification of the failure controlling flaw was not practical.

7.6 MECHANICAL TESTING

Thirty-eight MOR specimens were mechanically tested in a four-point fixture fabricated to NASA-LeRC drawing CF 302763. The specimens were stressed in quarter-point loading with an inner span of 9.5 mm and outer span of 19.0 mm at a cross-head of 0.5 mm/min.

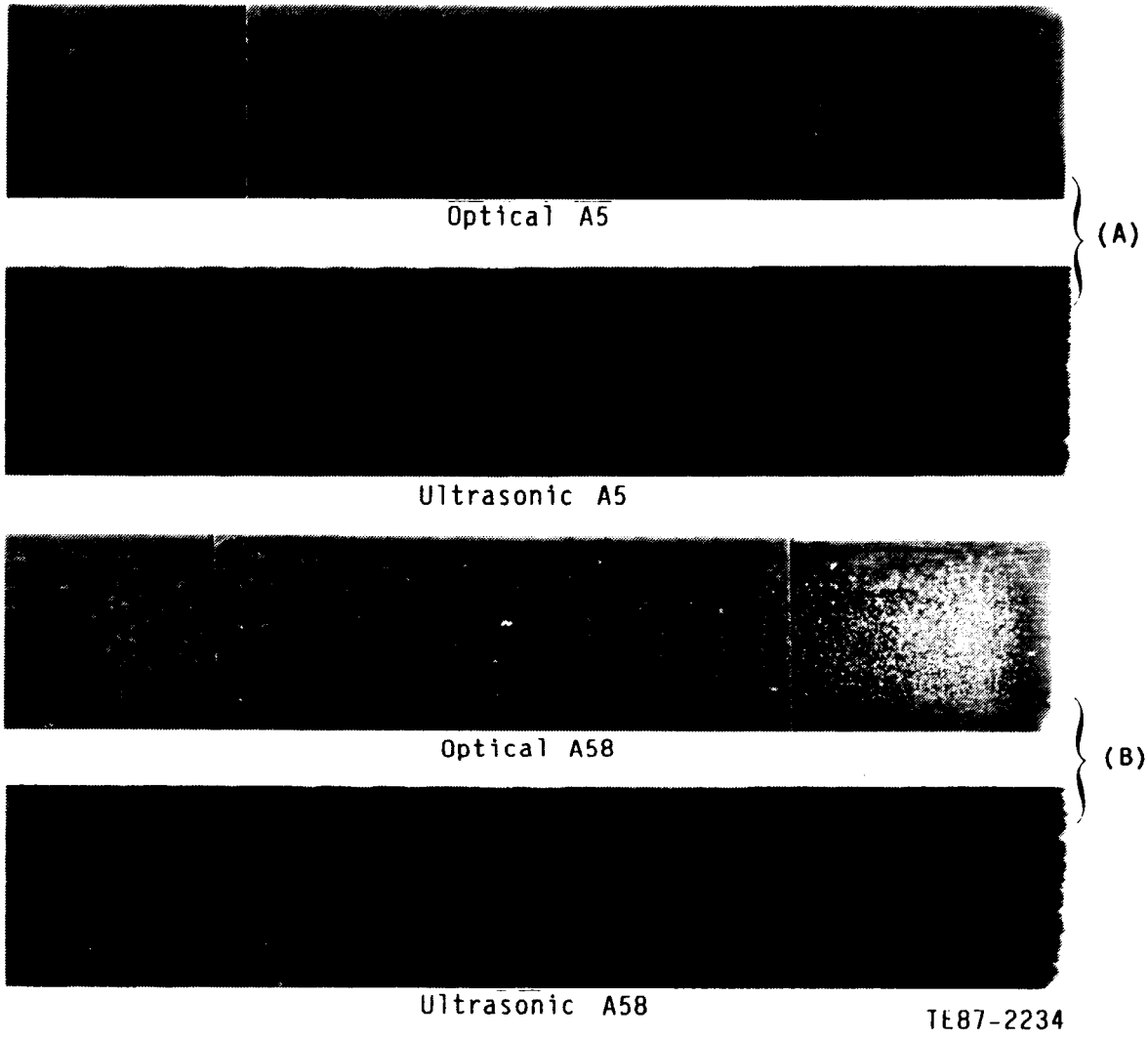

Figure 44. Ultrasonic C-scan grey scale imaging, (A) detection of machining marks (B) detection of surface pores.

The average strength of the material is 685.3 MPa (99.4 ksi) with a standard deviation of 119.2 MPa (17.3 ksi). This strength is in excellent agreement with the measured strength of about 650 MPa (94.3 ksi) and a standard deviation of 95 MPa (13.8 ksi) by Sanders and Baaklini (Ref 12, 13) for the similar generation of sintered silicon nitride. A two-parameter Weibull analysis of the flexural strength data, shown in Figure 45 yielded a Weibull modulus m = 6.5 and characteristic strength σ_0 = 730.9 MPa (106.3 ksi).

7.7 FRACTOGRAPHY

The fracture surface of each broken specimen was visually examined under 30X magnification to establish the nature and location of the failure controlling

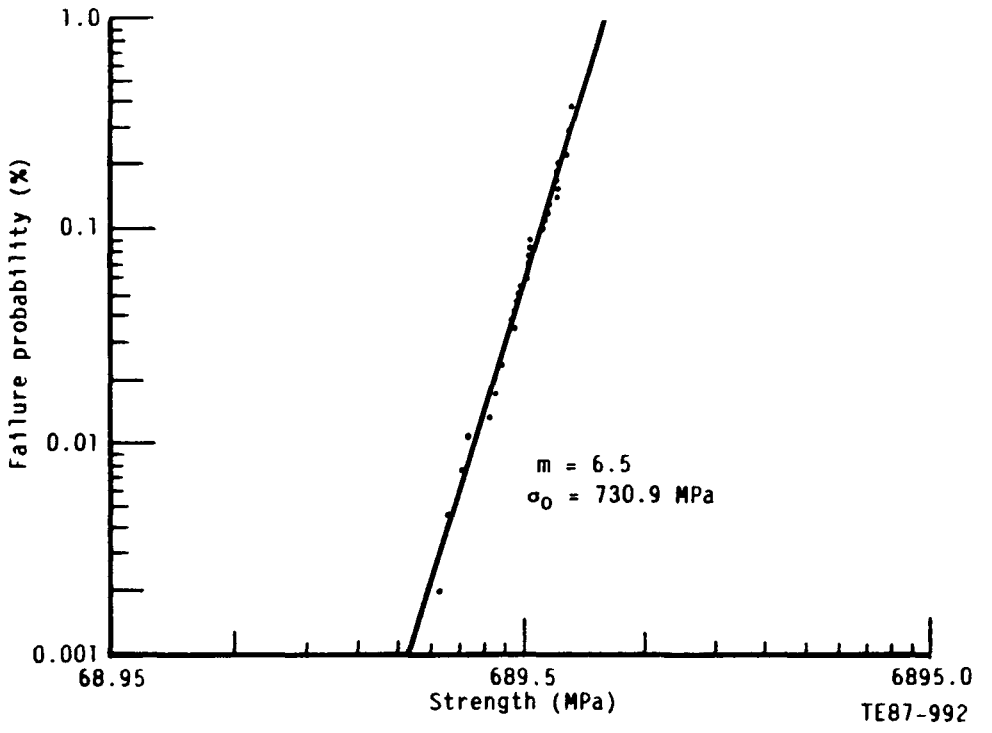

Figure 45. Weibull analysis of batch A sintered silicon nitride.

flaws. Each broken specimen was photographed to determine the x, y, and z coordinates of the failure origins for nondestructive evaluation (NDE) correlation studies. Scanning electron microscope (SEM) fractography of all the specimens was conducted at 500X to measure the flaw depth (a), width (2c), and the location (z) through the thickness. Pores and inclusions were found to control surface and subsurface failures. Table X shows the measured flexural strength, flaw size, and type of failure controlling defects and their location. An analysis of the failure origins, Table XI, shows that 60% of the failures were from surface flaws and 32% from internal defects. The remaining 8% specimen either had damaged origin or failed in the bevel region.

7.8 CORRELATION

Flaw Detection by Various NDE Techniques

Results of nondestructive evaluation (NDE) and detection of failure controlling surface and internal defects (pores and inclusions) in sintered silicon nitride MOR bars are summarized in Table XII. Fracture initiating flaws were detected in (1) one specimen by all four NDE techniques, (2) three specimens by both

Table X.
Flexural strength and failure analysis of batch-A sintered silicon nitride.

Spec no.	Flexural strength		Measured flaw size (μm)		Failure origin
	KSi	MPa	Depth (a)	Width (2c)	
A5	125.6	865.8	-	-	Origin damaged
A6	109.6	755.7	25	40	S, Inc
A7	123.0	848.1	15	27	S, Inc
A8	125.4	864.3	11	10	S, Inc
A10	117.0	806.5	20	12	S, P
A12	125.9	867.0	27	9	S, Inc
A14	92.0	634.6	21	18	S, P
A15	62.4	429.9	44	43	S, P
A16	82.6	569.5	11	66	S, P
A17	118.4	816.5	16	27	S, Inc
A18	123.7	853.0	20	66	I, Inc, 48 μm BTS
A20	99.9	688.8	30	48	S, P
A21	87.8	605.2	31	52	S, P
A22	117.2	808.1	44	44	I, Inc, 42 μm BTS
A23	93.3	643.4	12.5	23	S, P
A26	87.3	601.7	14	40	I, P, 80 μm BTS
A27	71.8	495.2	12.5	25	I, P, 22 μm BTS
A29	89.5	616.8	25	20	S, P
A30	112.4	775.3	37	37	I, P, 71 μm BTS
A31	92.3	636.6	48	66	I, P, 60 μm BTS
A32	70.0	482.5	14	51	I, P, 78 μm BTS
A33	81.2	559.7	-	-	Origin damaged
A34	95.6	658.9	27	44	I, P, 72 μm BTS
A37	106.7	735.6	24	25	S, P
A38	91.4	630.3	27	45	S, P
A39	99.3	684.8	38	47	I, Inc, 70 μm BTS
A41	99.7	687.7	11	21	S, P
A42	98.7	680.7	21	21	I, P, 23 μm BTS
A43	116.3	802.1	31	29	S, P
A46	107.8	743.2	29	49	I, P, 28 μm BTS
A47	94.6	652.0	Undefined flaw Boundary		S, P
A51	65.1	449.1	14	64	I, P, 68 μm BTS
A54	115.8	798.4	8	26	S, P
A55	83.4	574.7	106	105	S, P
A57	100.1	690.2	15	18	S, Machining damage
A58	80.6	555.8	54	83	S, P
A59	100.3	691.7	55	10	S, Inc
A65	113.1	780.0	22	25	S, Inc
Avg.	99.4	685.3			
Std. Dev.	17.3	119.2			

S --surface
P --pore
I --internal
Inc--inclusion
BTS--below tensile surface

Note: The strength of the specimens that failed from internal flaws has been corrected to represent actual stress at the flaw.

Table XI.
Analysis of failure origins in machined Si_3N_4 bars.

Number of test bars	Damaged origin	Number of Specimens failed from Surface		Internal		Bevel Failure
		Pores	Inclusions	Pores	Inclusions	
38	2	16	7	9	3	1
Percentage	5	42	18	24	8	3

PAM and microradiography, and (3) twenty specimens by PAM alone. Fracture controlling flaws were not detected in four specimens by any of the NDE techniques used. No correlation was possible in ten specimens as follows: failure site of seven specimens coincided with PAM signals from the artifacts in the PAM cell window, origin was lost in two specimens, and one specimen failed in the bevel region.

Optical micrography did not reveal small surface defects at the 7X magnification. It was also observed that the anomalies could not be differentiated from each other at higher magnification because of poor contrast and the large number of similar size flaws. Ultrasonic C-scan grey scale imaging (10X) was performed with an incremental scan of 63 μm which is 2 to 3 times larger than the failure initiating defects of 20-30 μm size, and therefore did not possess required line resolution to detect small flaws. Also, a large portion of the incident ultrasonic wave is scattered by the irregular shaped flaws and less energy is received back by the transducer, thereby substantially decreasing the signal-to-noise ratio. It should be noted that a 50 micron nominal diameter surface void was repeatedly detected under the same experimental conditions in the reference specimen as shown in Figure 43. Therefore, it is hypothesized that smaller flaws can be detected by decreasing the scanning increment and increasing the ultrasonic frequency which would result in improved signal-to-noise ratio. Projection microradiography detected flaws in only five specimens because of the low magnification (5X) used and the very small size of the flaws relative to the specimen thickness. PAM digital images were correlated with failure initiating sites of 28 specimens. PAM detected fracture controlling surface and subsurface flaws (pores and inclusions) in 24 of the 28 specimens within ±200 μm of the measured x-y coordinates of the flaws.

Table XII.
Correlation and detectability of failure controlling flaws by various NDE techniques.

Specimen	Failure origin	Optical	UT	PAM	X-ray
A5	Origin damaged	--	--	--	--
A6	S, Inc.	ND	ND	Artifact	ND
A7	S, Inc.	ND	ND	D	ND
A8	S, Inc.	ND	ND	Artifact	ND
A10	S, P	ND	ND	Artifact	ND
A12	S, Inc.	ND	ND	Artifact	ND
A14	S, P	ND	ND	Artifact	ND
A15	S, P	ND	ND	D	ND
A16	S, P	ND	ND	D	ND
A17	S, Inc.	ND	ND	D	ND
A18	I, Inc.	ND	ND	ND	ND
A20	S, P	ND	ND	Artifact	ND
A21	S, P	ND	ND	D	ND
A22	I, Inc.	ND	ND	D	ND
A23	S, P	ND	ND	D	ND
A26	I, P	ND	ND	ND	ND
A27	I, P	ND	ND	D	D
A29	S, P	ND	ND	D	ND
A30	I, P	ND	ND	D	ND
A31	I, P	ND	ND	D	D
A32	I, P	ND	ND	D	ND
A33	Origin damaged	--	--	--	--
A34	I, P	ND	ND	D	D
A37	S, P	ND	ND	D	ND
A38	S, P	ND	ND	D	ND
A39	I, Inc.	ND	ND	D	ND
A41	S, P	ND	ND	D	ND
A42	I, P	ND	ND	D	ND
A43	S, P	ND	ND	D	ND
A46	I, P	ND	ND	D	ND
A47	S, P	ND	ND	ND	ND
A51	I, P	ND	ND	Artifact	D
A54	S, P	ND	ND	ND	ND
A55	S, P	ND	ND	D	ND
A57	S, Machining damage	ND	ND	Bevel fracture	ND
A58	S, P	D	D	D	D
A59	S, Inc.	ND	ND	D	ND
A65	S, Inc.	ND	ND	D	ND

D = detected
ND = not detected
S = surface
I = internal
P = pore
Inc = inclusion
Artifact = handling damage in PAM cell window coincided with failure origins

The ±200 μm error in the measurement of the defect coordinates occurred because the fracture surface of the specimens could not be maintained perpendicular to the optical axis while photographing. PAM images and SEM micrographs of the failure origins are compiled in Appendix II.

The detection of a flaw depends on the properties of the material in the vicinity of the defect. For example, specimen no. A55 failed from the largest fracture controlling surface pore of 105 μm diameter which was detected only by photoacoustic microscopy as shown in Figure 46. Clearly, only the thermal properties of the flaw were different compared with that of the surrounding material. This flaw was not detected by ultrasonic and radiography. Figure 47 reveals that a surface pore, 54 μm x 83 μm, was detected in specimen no. A58 by all the NDE methods used, confirming that flaw characteristics have a significant influence on detectability by a given technique. This shows that a combination of NDE methodologies is required for the reliable detection of the failure initiating defects. Figures 48 and 49 show typical examples of small pores and inclusions detected only by PAM. Similar size seeded spherical voids have been detected as shown in Table III by microradiography. Undoubtedly, further development of both X-ray and ultrasonic technology is essential to routinely characterize structural ceramic materials and components to detect

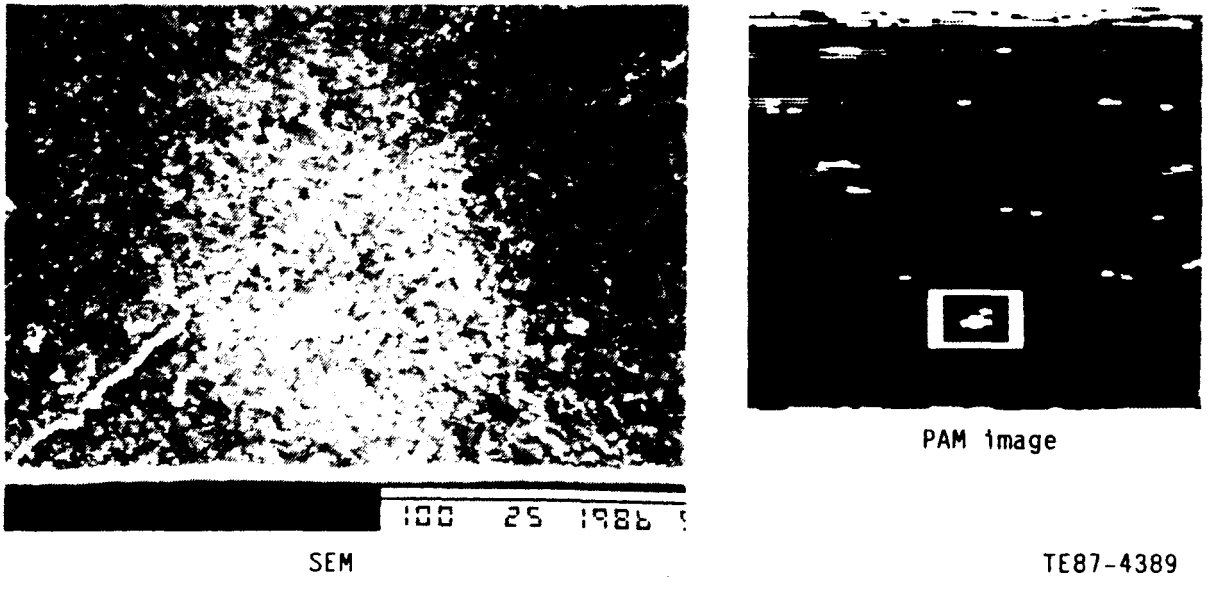

Figure 46. Detection of surface pore by photoacoustic microscopy in specimen no. A55.

Figure 47. Detection of fracture controlling surface pore in machined sintered silicon nitride specimen no. A58.

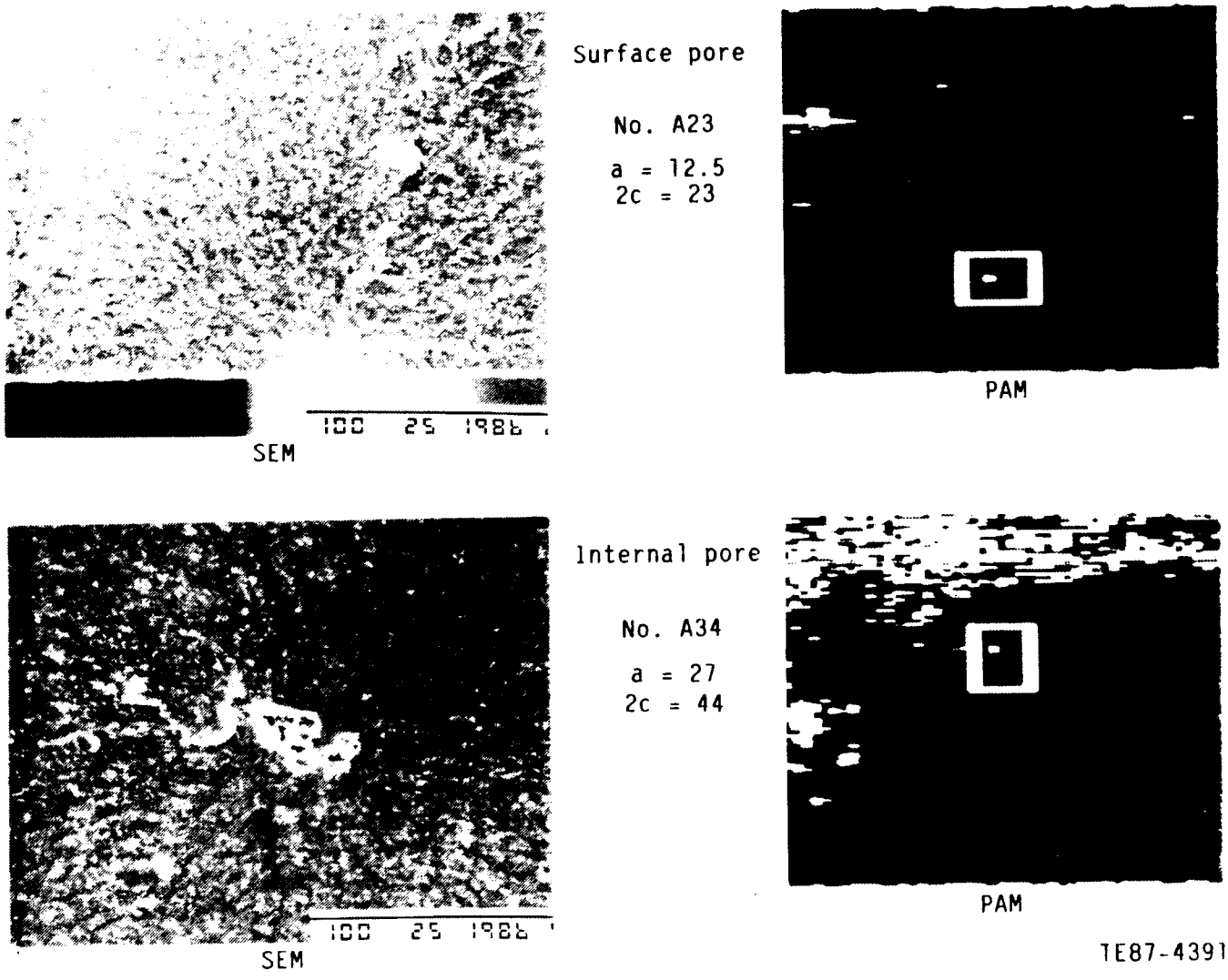

Figure 48. Detection of pores in machined sintered silicon nitride specimen nos. A23 and A34.

10 to 40 micron size natural irregular flaws with large variations in aspect ratio.

Flaw characteristics also have a significant effect on flaw sizing by ultrasonic, microradiography, and photoacoustic microscopy. Table XIII shows the measured size of the failure initiating flaws in four specimens by various NDE techniques. The flaw width, D_x, determined from the PAM images is larger for three specimens and smaller for one specimen compared with the measured size by the X-ray. The flaw length, 2c or D_y, calculated from the SEM micrographs and PAM images are in good agreement, indicating that subsurface pores within

Table XIII.
Comparison of detected flaw sizes by various NDE techniques.

Specimen	Fractography Type	Fractography Size+ 2c*	Optical D_x	Optical D_y	Ultrasonic D_x	Ultrasonic D_y	PAM D_x	PAM D_y	X-ray D_x	X-ray D_y
A27	I, P	25	ND	ND	ND	ND	52	25	100	150
A31	I, P	66	ND	ND	ND	ND	130	75	50	50
A34	I, P	44	ND	ND	ND	ND	78	25	50	100
A58	S, P	83	283	99	320	159	169	75	75	75

+ = all values are in microns
I = internal
S = surface
P = pore
* = the value of 2c is the same as D_y in optical, ultrasonic, PAM, and X-ray. This dimension is perpendicular to the applied stress in flexural testing.

one thermal diffusion length can be detected and sized. The flaw length obtained from the microradiographs agree with the PAM results for the two specimens but are substantially larger for the other two specimens. Evidently, both the experimental parameters and actual flaw type, shape, location, and depth from the interrogating surface affect the PAM image and computed defect size.

Correlation Between PAM and Fractography Measured Flaw Size

Results of PAM and fractography measured flaw dimensions presented in Figure 50 reveal that fracture controlling flaws of 10 to 115 microns are oversized by photoacoustic microscopy with large scatter and offset. The PAM measured dimensions, D_x, of the failure initiating flaws in the x-direction (scanning axis) are depicted in Figure 50 (A) as a function of flaw length (2c) and flaw depth (a), respectively. Each point on the diagonal of both the plots is equidistant from the abscissa and ordinate. The apparent width (D_x) increased with '2c' with a positive offset of about 60 $\pm$ 10 μm from the ideal line. This is in excellent agreement with the offset of 50 μm obtained for the diameter of the top-drilled holes, shown in Figure 27. Therefore, the offset appears to be more affected by the experimental conditions (laser focal

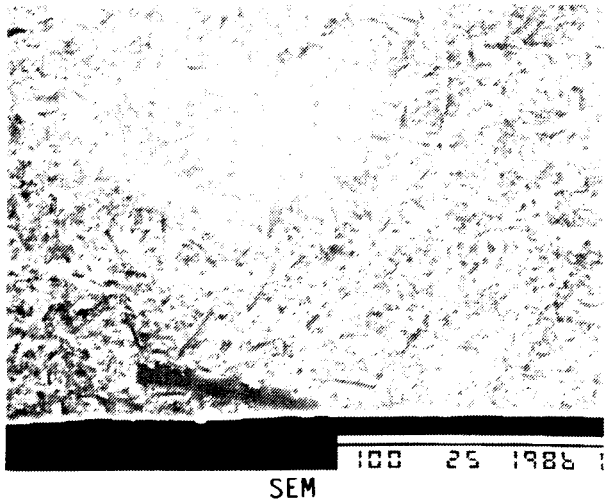

SEM

Surface inclusion

No. A65

a = 22 μm
2c = 25 μm

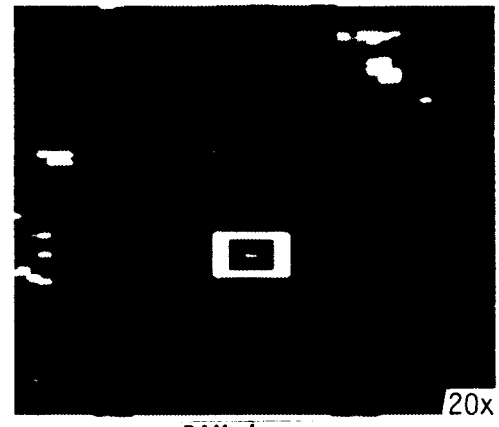

PAM image

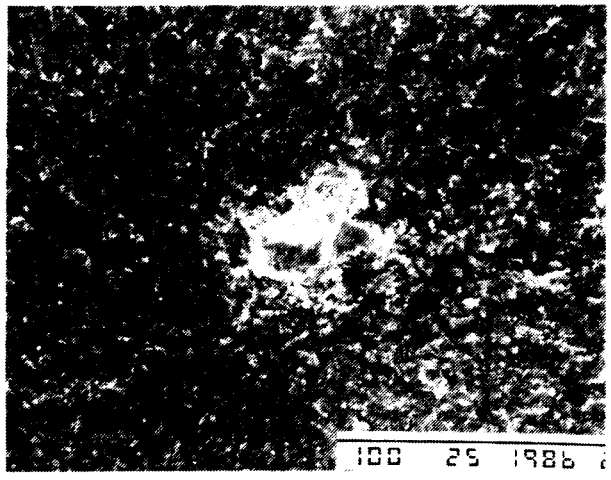

SEM

Internal inclusion

No. A39

a = 38 μm
2c = 47 μm

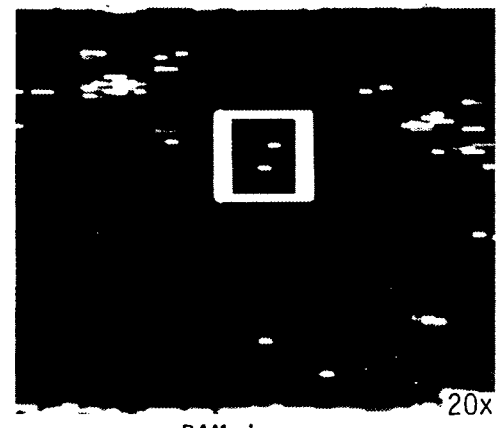

PAM image

TE87-4392

Figure 49. Detection of inclusions in machined silicon nitride specimen nos. A65 and A39.

spot diameter, scan speed, increment, time constant, etc) than the flaw length. The apparent width, D_x, is substantially greater than the actual flaw depth (a). It is hypothesized that D_x is affected by the subsurface nature of the natural flaws. For example, D_x is about 60 μm for all flaws with depth ranging from 12 to 45 μm. Conversely, D_x varies from 50-100 μm for a flaw depth of 15 μm.

Figure 50(B) shows that PAM measured flaw size, D_y, increases with the actual flaw length (2c) which is in excellent agreement with the similar data on top-drilled holes. There are four flaw sizes between 25 to 100 microns as measured from the PAM images. The 25 μm to 50 μm flaw size corresponds to the de-

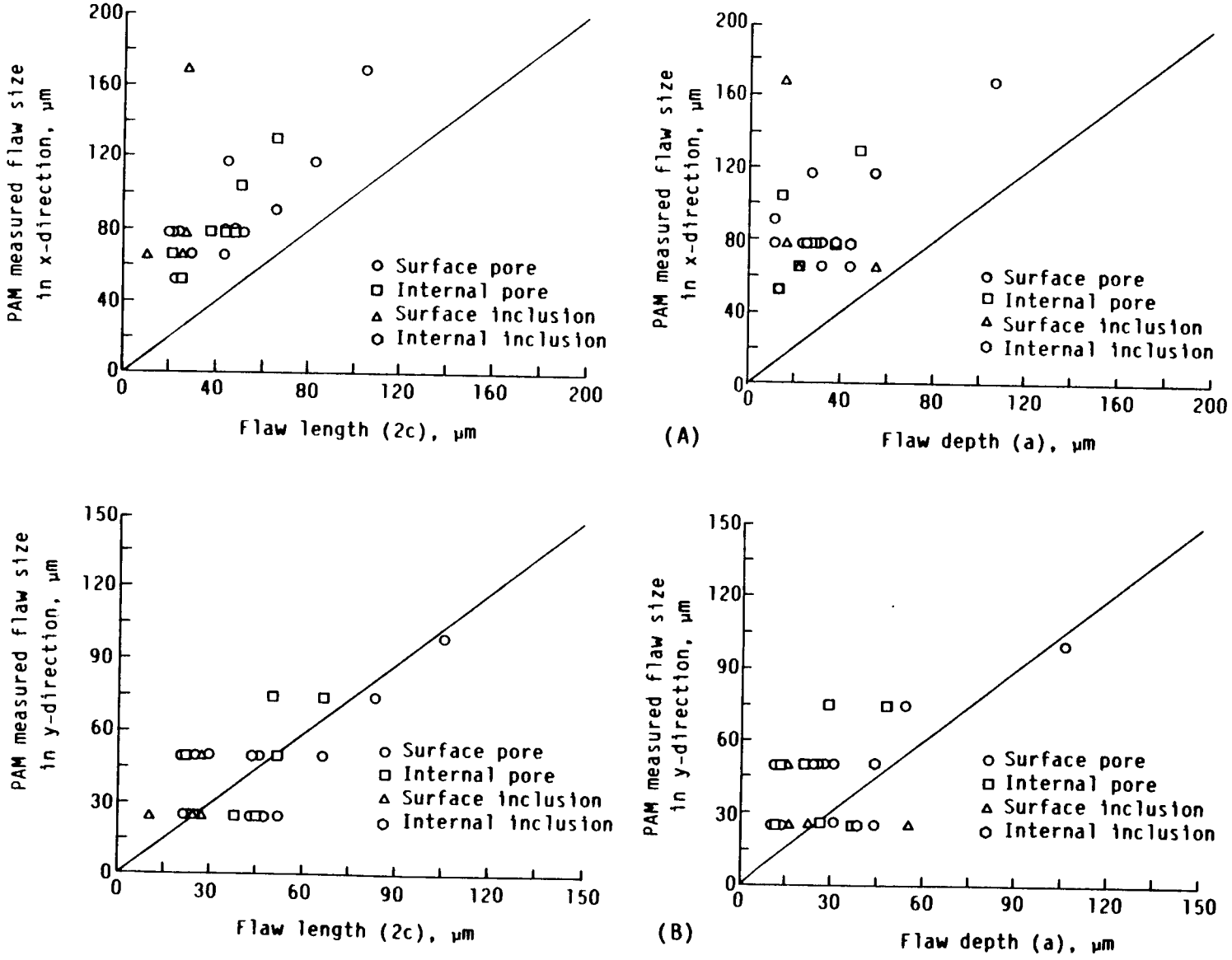

Figure 50. PAM measured flaw dimensions (A) x-direction and

fect length from 10 to 67 μm, the 75 μm size relates to the 52 to 83 μm length, and the 100 μm size corresponds to the 105 μm defect length. It is apparent that on the average, PAM provides larger flaw sizes for flaws ≤ 100 μm in size. As the flaw length increases, PAM measured sizes are more comparable to actual flaw lengths with the decreasing effect of the experimental conditions. The apparent length, D_y, is also greater than the actual flaw depth, shown in Figure 50(B). The value of D_y ranged between 25 to 75 μm for flaws with depths of 12 to 55 μm with large scatter and overlap. This clearly indicates that the large variation is primarily due to the scattering of the thermal waves from the three dimensional characteristics of the natural flaw.

Correlation Between Flexural Strength and Flaw Size

Brittle behavior of ceramics is controlled by both intrinsic and extrinsic flaws. The flaw characteristics and initial flaw distribution affects the final fracture mode and behavior of structural ceramic materials. The combination of all the variables results in large scatter in the strength distribution of brittle ceramics. Figure 51 shows the plot between flexural strength and flaw depth (a). The large scatter in flexural strength is due to variability in crack intensity factor at the flaw tip and interaction between the flaws which modifies the flaw distribution and characteristics. Figure 52 shows that there is a general trend of decreasing flexural strength with increasing flaw length for both pores and inclusions. It is interesting to note that the specimens which failed from the inclusions are in the upper bound while the pore failures are scattered approximately equally on both sides of the regressed line. Baratta, Kirchner, and Munz (ref 14-17) have also shown that failure controlling defects in brittle ceramic materials are generally associated with a crack developed during stressing the specimen in flexural testing. The size of this crack depends on the material microstructure and may be one or more grain size long. Both flaw depth (a) and defect length (2c) may be undersized. Also, the poor contrast between the flaw boundary and the parent material leads to error in the measurement of defect size from the fractographs. Evidently, many variables contribute to the scatter observed in both the flexural strength and defect size.

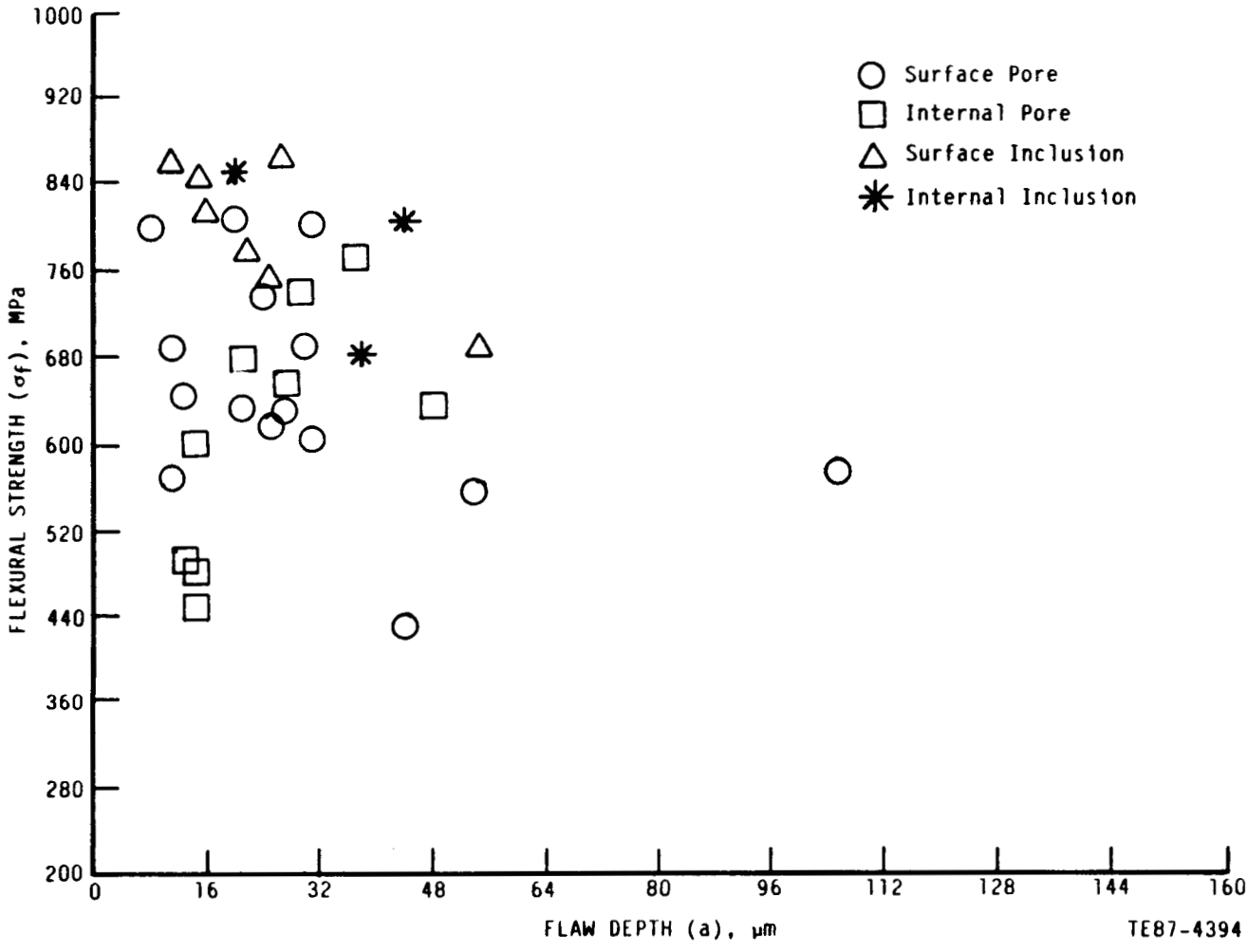

Figure 51. Flexural strength as a function of measured flaw depth (a) in sintered silicon nitride.

Correlation Between PAM Signal, Flexural Strength, and Flaw Size

Photoacoustic signals from failure initiating flaws, as shown in Figure 53, did not correlate with flexural strength, flaw length (2c), and depth (a). The results also indicate that PAM signals vary substantially for a given depth or length for both surface and subsurface pores and inclusions with no trend. Further analysis revealed that PAM signals were also randomly distributed as a function of the aspect ratio of the defects. Therefore, it is believed that three dimensional characteristics of small defects significantly influence the interaction and scattering of the thermal waves which results in large variations in the photoacoustic signal.

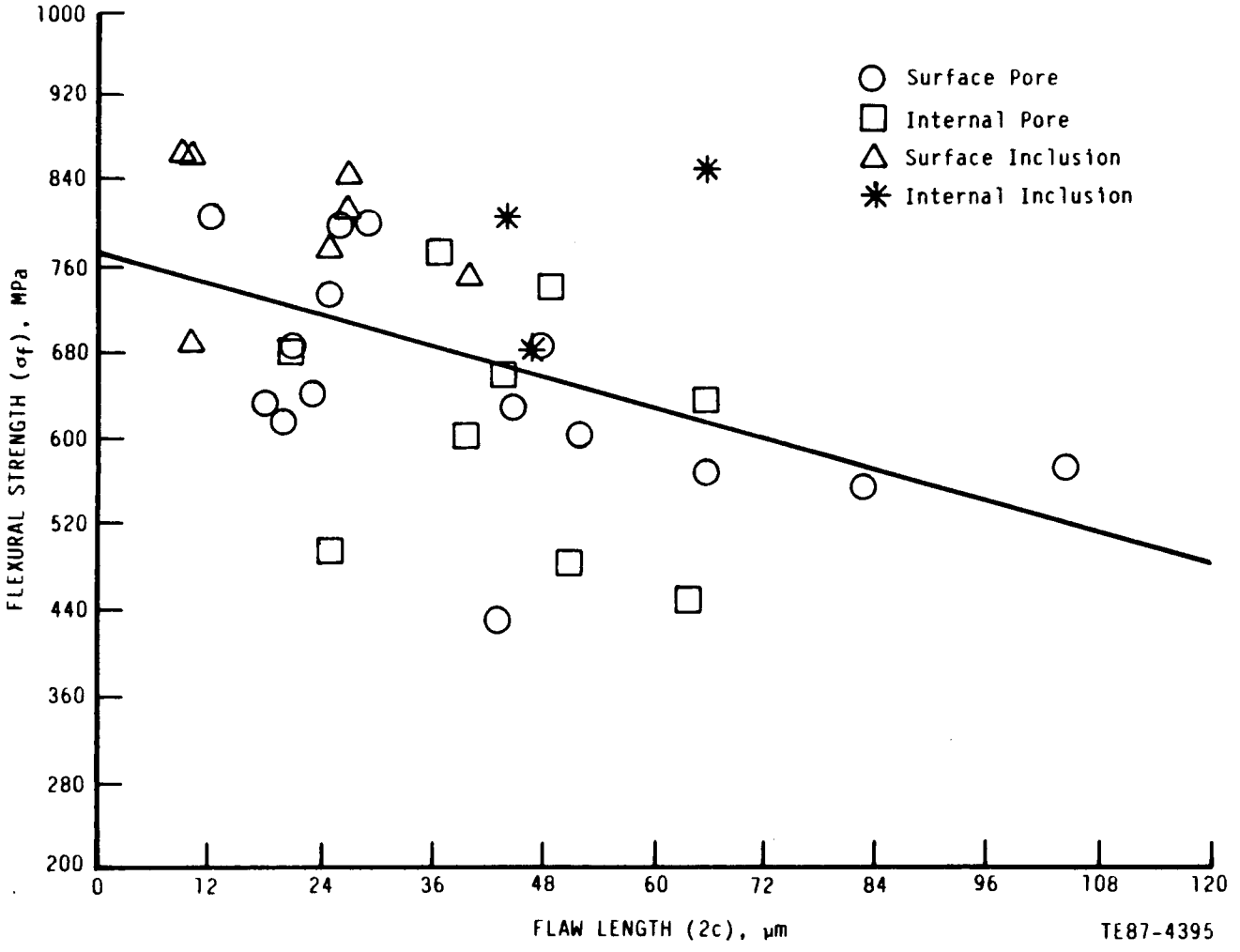

Figure 52. Flexural strength as a function of flaw length (2c) in sintered silicon nitride.

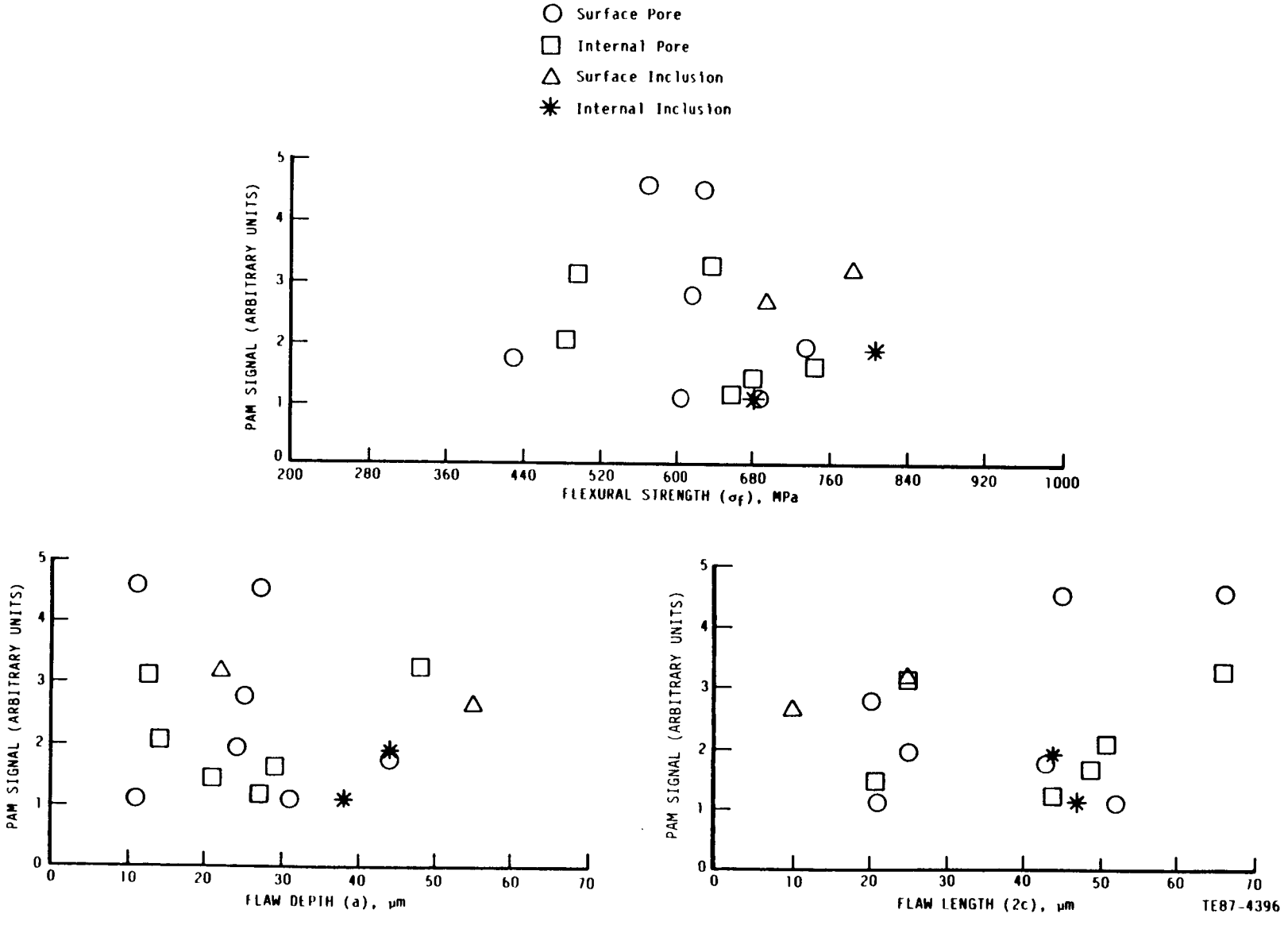

Figure 53. Photoacoustic signal from failure initiating flaws as a function of measured flexural strength, flaw depth, and length.

VIII. SUMMARY OF RESULTS

A real time Photoacoustic Microscopy (PAM) digital data acquisition, imaging, and analysis system was successfully developed and used to detect surface and subsurface material and topographical variations and flaws. Menu driven algorithms were developed in machine language and implemented for rapid data processing to create PAM images, and perform flaw location and sizing. The software is capable of magnifying and scrolling images in all four directions on the CRT screen. The raw data images can be smoothed by subtracting the background signal using the programmable threshold function.

The system was applied, along with microfocus radiography and ultrasonic scanning, to nondestructively evaluate silicon nitride specimens in the green and sintered conditions as well as to sintered silicon carbide. Correlations were obtained between NDE information and failure initiation sites in silicon nitride.

1. Drilled surface holes 130 μm diameter x 28 μm deep and 8 μm apart were resolved in sintered silicon nitride with machined surfaces indicating that surface flaw resolution and sizing is primarily influenced by laser spot size. The magnitude of the PAM signal increased linearly with hole depth up to one thermal diffusion length and remained essentially flat thereafter.

2. Tight 96 μm long surface cracks induced by Knoop hardness indenters were detected at a scan speed of 50 μm/sec but not at 250 μm/sec in hot pressed silicon nitride. Cracks 140 μm length and larger were detected at 250 μm/sec in both hot-pressed and sintered silicon nitride with similar machined surface finish.

3. Subsurface holes equivalent to one thermal diffusion length in diameter, depth, and distance apart were spatially resolved in both as-fired and machined silicon nitride. Side-drilled holes up to 441 μm diameter were detected up to a depth of 573 μm below the interrogating surface. Seeded voids 20 to 50 μm diameter located within 50 μm below the interrogating surface were detected.

4. Seeded voids 450 μm diameter located 270 μm below the interrogating surface were detected in as-fired silicon carbide. Subsurface side-drilled holes of 250 μm diameter and 1000 μm below the surface were detected.

5. Correlation studies revealed the following:
(a) Flaw characteristics have a significant effect on flaw detection by various NDE techniques. Photoacoustic microscopy detected fracture controlling flaws in twenty-four out of thirty-eight machined silicon nitride specimens. This compares with four by microfocus radiography and one by ultrasonics.
(b) Flaw sizes were consistently overestimated by PAM with a large degree of scatter.
(c) The magnitude of the photoacoustic signal varied randomly for a given flaw depth, length, aspect ratio, and flexural strength with no trend. Identification of specific flaw types and sizing requires additional quantitative investigation and theoretical understanding of thermal wave interaction with flaw characteristics.

6. The applicability of the PAM technique was found to be limited as an in-process nondestructive evaluation tool for examination of structural ceramic materials in the green state for the following reasons:
(a) Surface holes 106 microns diameter were detected but 375 micron diameter holes just 50 microns beneath the surface were not detected, indicating that thermal waves were rapidly damped and scattered by the highly porous unsintered compacts, severely limiting the ability of the technique to interrogate the internal structure of these materials.
(b) Laser scanning resulted in volatization of material from and alteration of the specimen surface. Specimens subsequently sintered developed surface microcracks in the photoacoustically scanned regions. The apparent damaging effect of PAM precludes the use of the technique on components intended for use in the as-sintered condition.

7. The room temperature flexural strength of the materials was 685.3 MPa with a standard deviation of 119.2 MPa. The Weibull modulus of the material was 6.5 with a characteristic strength of 730.9 MPa. The majority of specimens failed from surface and subsurface pores and inclusions.

8. Flexural strength of silicon nitride was inversely proportional to flaw length (2c) both for pores and inclusions. Flexural strength for specimens which failed from inclusions was generally higher than for specimens which failed from pores.

9. Microradiography detected (a) Seeded voids of 20 to 50 μm diameter located within 50 μm below the surface.

REFERENCES

1. "Ceramic Applications in Turbine Engines - Final Report," NASA CR-174715, October 1984, pp 106-32.
2. P. K. Khandelwal, "Ultrasonic Imaging of Ceramic Turbine Components," presented at the 87th Annual American Ceramic Society Meeting, Cincinnati, 1985.
3. P. K. Khandelwal and P. W. Heitman, "Correlation Between Ultrasonic Velocity and Density of Ceramic Turbine Blades," presented at the 11th Annual Conference on Composites and Advanced Materials, January 18-21, 1987, Cocoa Beach, Florida.
4. P. K. Khandelwal, P. W. Heitman, A. J. Silversmith, and T. D. Wakefield, "Surface Flaw Detection in Structural Ceramics by Scanning Photoacoustic Microscopy," Applied Physics Letter 37 (9), November 1980, pp 779-81.
5. M. J. Lin, L. J. Inglehart, L. D. Favro, P. K. Kuo, and R. L. Thomas, "Thermal Wave Detection of Vertical Cracks in Opaque Solids," in Review of Progress in Quantitative Nondestructive Evaluation, edited by D. O. Thompson and D. E. Chimenti, Vol 4B, 1985, pp 739-44.
6. P. K. Khandelwal, R. R. Kinnick, and P. W. Heitman, "Photoacoustic Microscopy of Ceramic Turbine Blades," Ceram Bullet, Vol 64, No. 8, 1985, pp 1112-15.
7. A. Rosencwaig, "Thermal Wave Imaging," Science, Vol 218, 15 October, pp 223-28.
8. L. J. Inglehart, D. J. Thomas, M. J. Lin, L. D. Favro, P. K. Kuo, and R. L. Thomas, "Resolution Studies for Thermal Wave Imaging," in Review of Progress in Quantitative Nondestructive Evaluation, edited by D. O. Thompson and D. L. Chimenti, Vol 4B, 1985, pp 753-59.
9. M. G. Mendiratta, "Prediction of Fracture Energy from Microhardness Indentation in Structural Ceramics" J. Mater Sci 11 (1976) pp 973-976.
10. J. Lankford and D. L. Davidson "Indentation Plasticity and Microfracture in Silicon Carbide" J.Mater Sci 14 (1979) pp 1669-1675.
11. W. Arnold, B. Hoffman, and H. Williams, "Crack Depth Estimation by Photoacoustic Microscopy", presented at the 2nd International Symposium on "Ceramic Materials and Components for Engines", Lubeck, W. Germany, April 14-17, 1986.

12. W. A. Sanders and C. Y. Baaklini, "Correlation of Processing and Sintering Variables with the Strength and Radiography of Silicon Nitride," NASA TM87251, February 1986.
13. W. A. Sanders, Private Communications, September 9, 1986.
14. F. I. Baratta, "Comments on Strength of Reaction-bonded Silicon Nitride with Artificial Pores," Comm Amer Ceram Soc 65 (2), C32-C34, 1982.
15. J. Heinrich and D. Munz, "Reply," Comm Amer Ceram Soc 65 (2), C34, 1982.
16. H. P. Kirchner and R. M. Gruver, "A Fractographic Criterion for Subcritical Crack Growth Boundaries in Hot-Pressed Alumina," J Mater Sci 14, pp 2110-18, 1979.
17. H. P. Kirchner, R. M. Gruver, and W. A. Sotter, "Characteristics of Flaws at Fracture Origin and Fracture Stress-Flaw Size Relations in Various Ceramics," Mater Sci Eng 22 (2), pp 147-56, 1976.

APPENDIX I

Optical micrographs of machined sintered silicon nitride specimens, where

T - Top surface
B - Bottom surface

The area between the black lines was examined by photoacoustic microscopy.

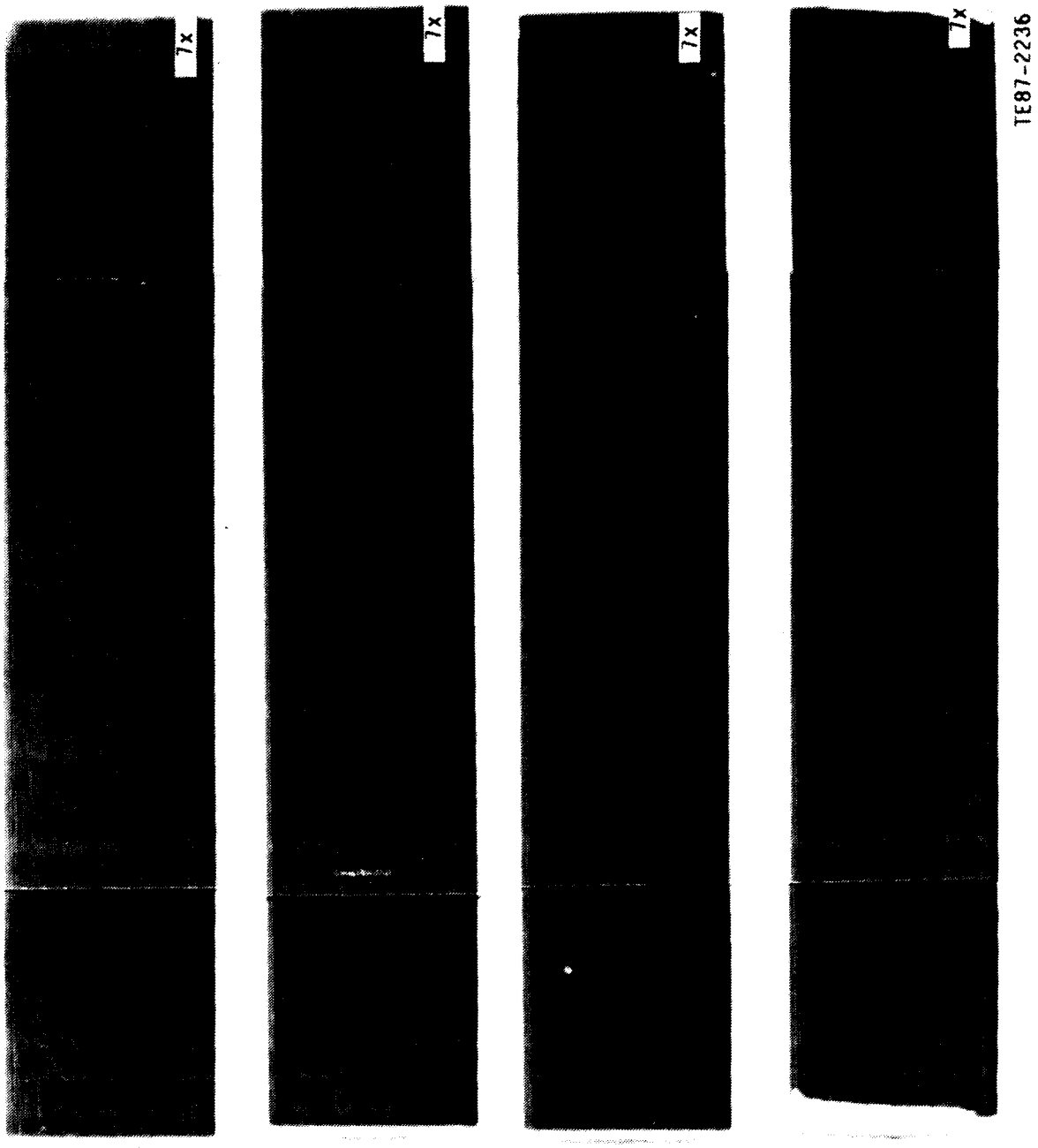

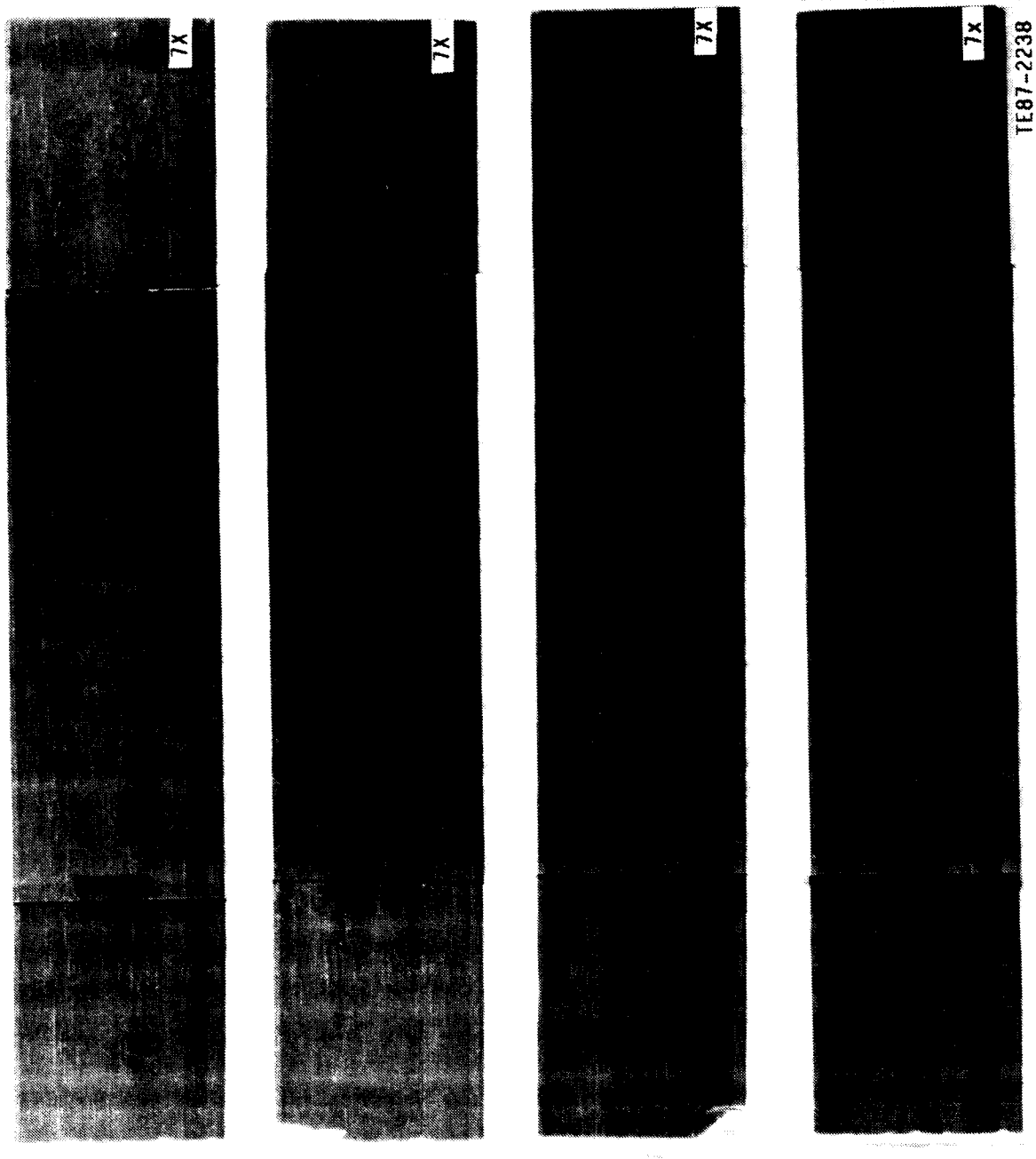

Specimen no.

A15B

A16B

A17T

A18T

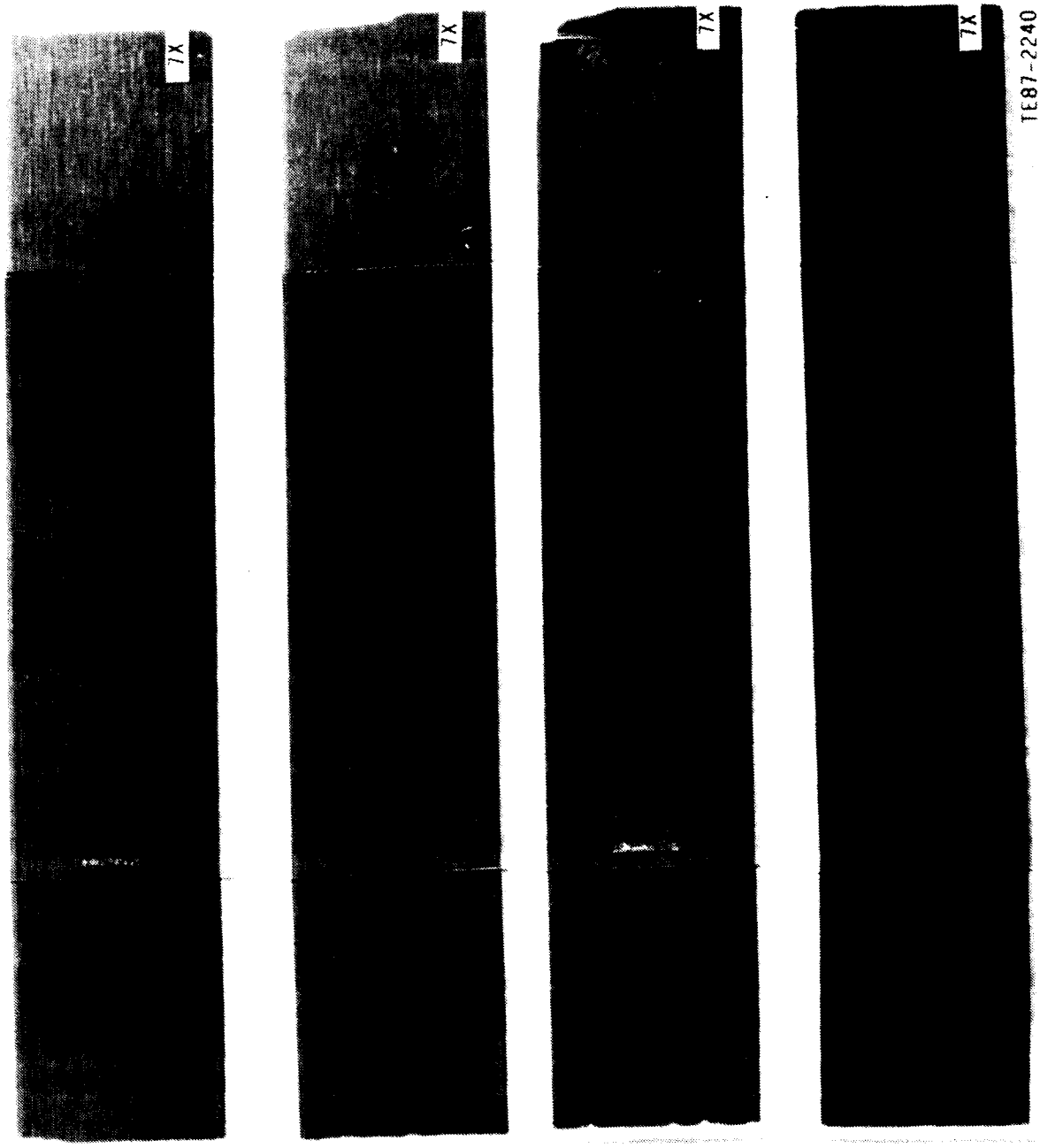

C-2

ORIGINAL PAGE IS
OF POOR QUALITY

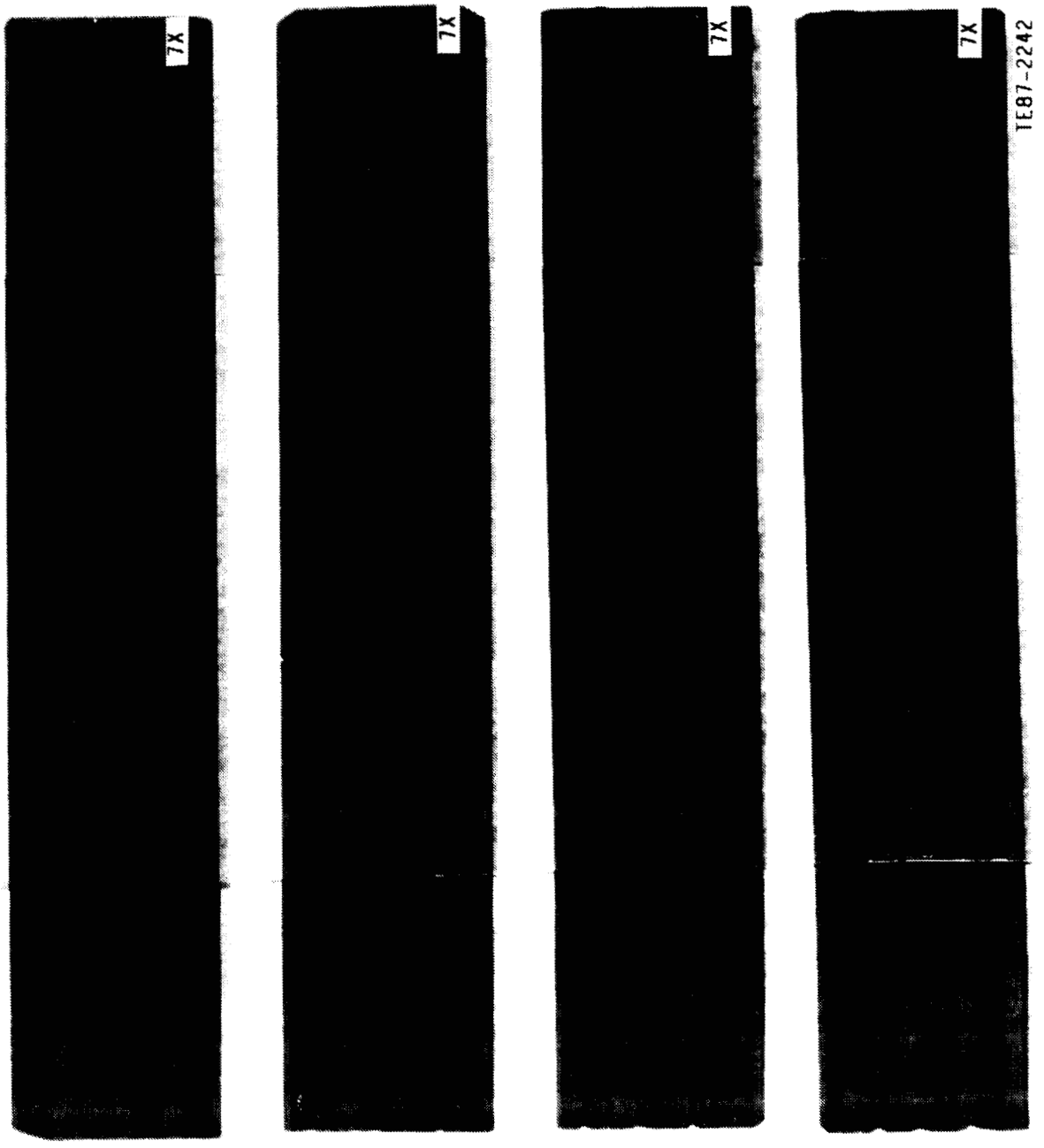

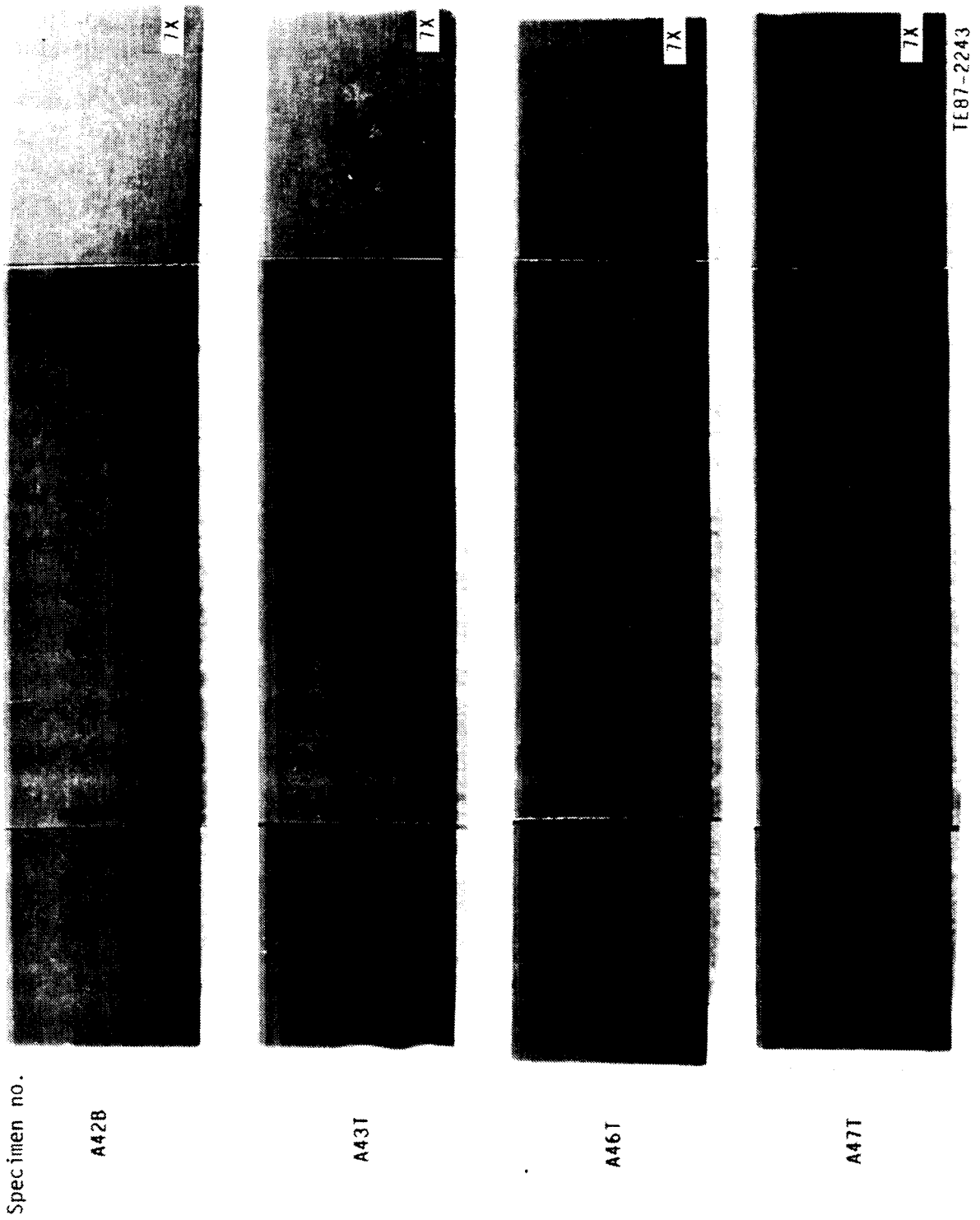

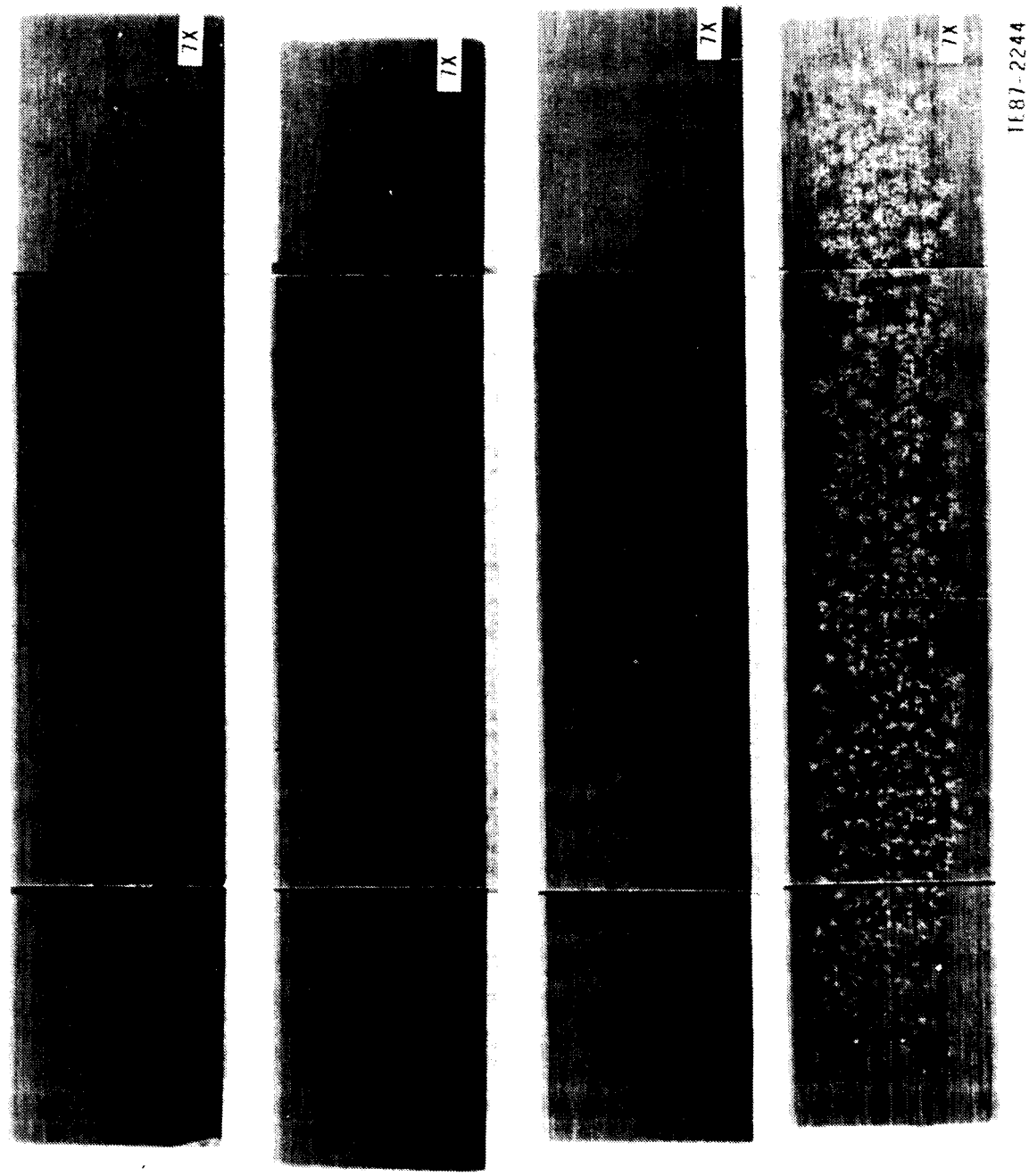

APPENDIX II

Scanning electron micrographs and photoacoustic microscopy digital images of failure initiating defects in machined sintered silicon nitride.

ORIGINAL PAGE IS
OF POOR QUALITY

Specimen No.	SEM	PAM
A7	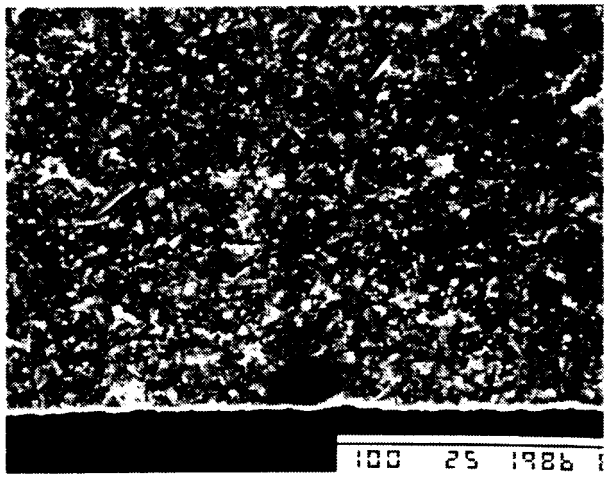	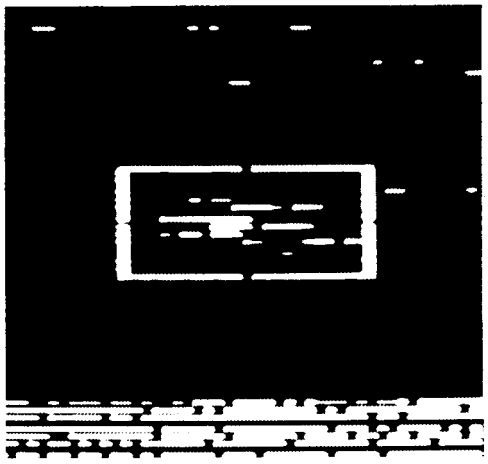
A15	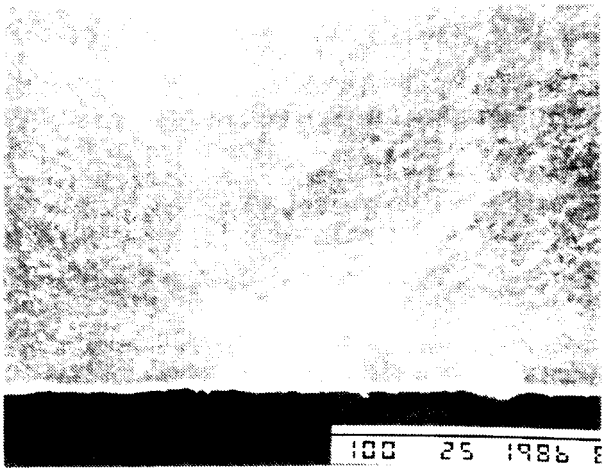	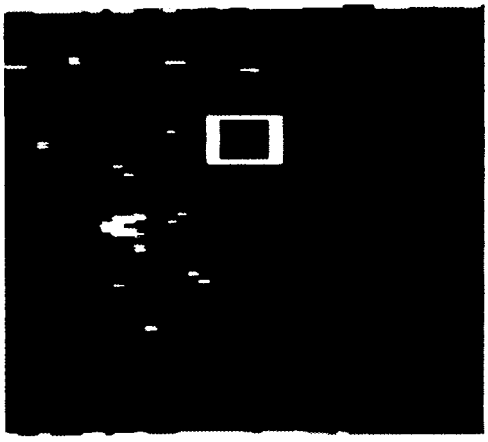
A16	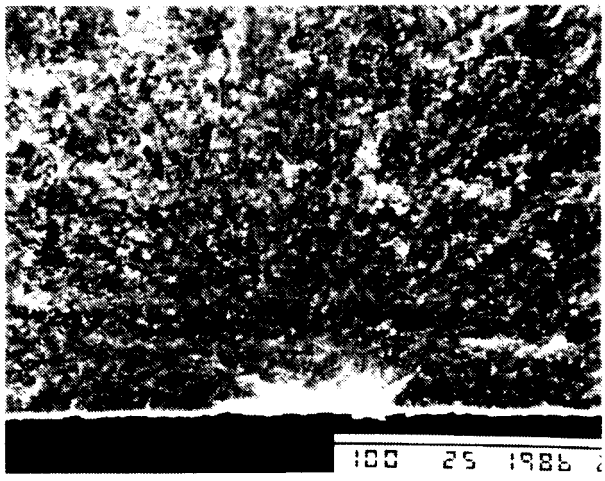	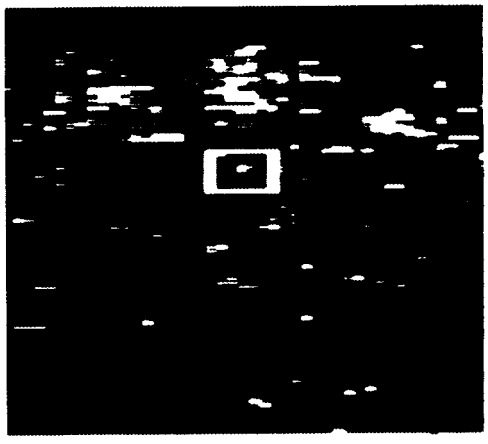

TE87-4379

ORIGINAL PAGE IS
OF POOR QUALITY

Specimen No.	SEM	PAM
A17	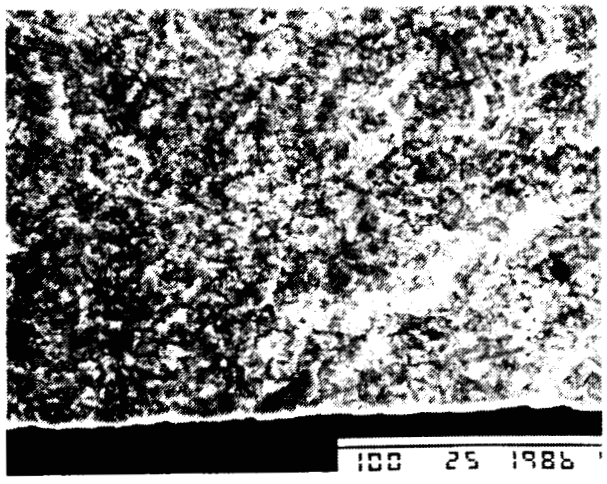	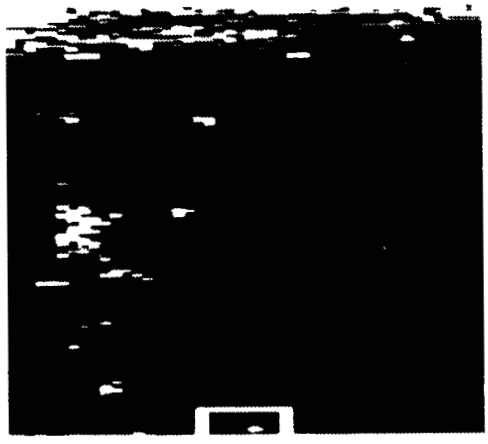
A21	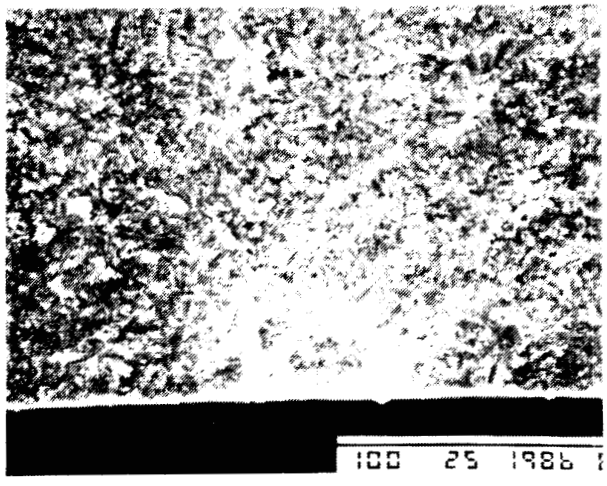	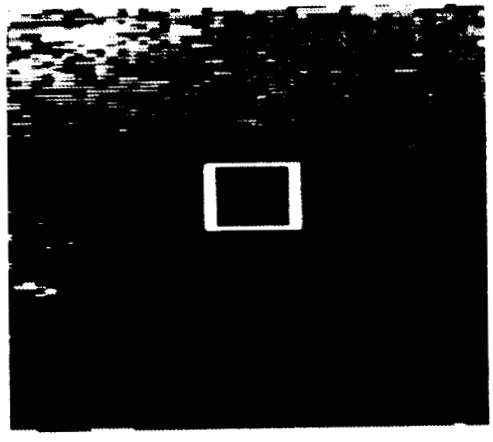
A22	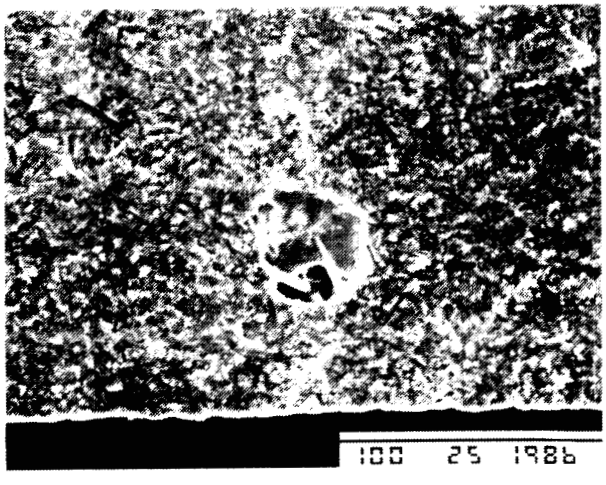	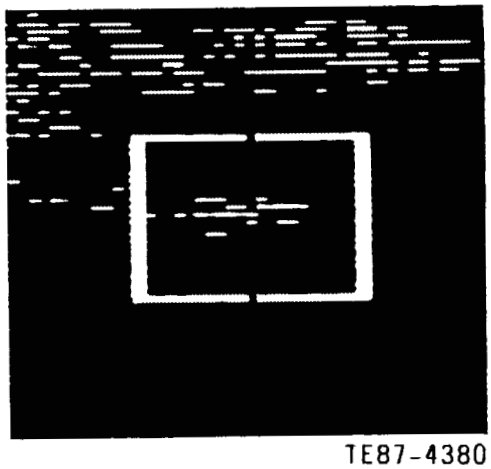

TE87-4380

ORIGINAL PAGE IS
OF POOR QUALITY

Specimen No.	SEM	PAM
A27	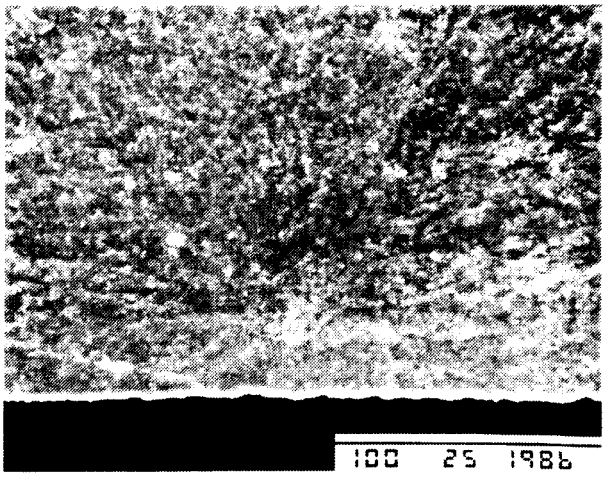	
A29	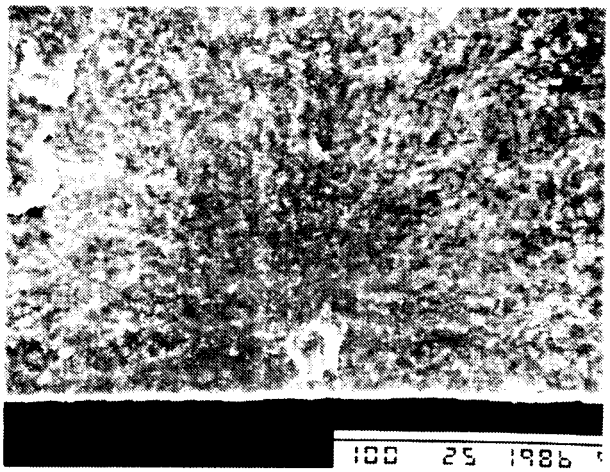	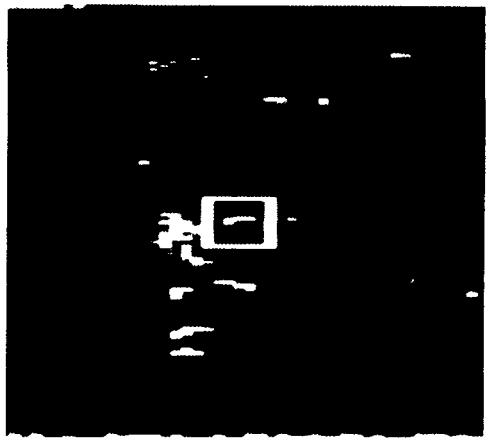
A30	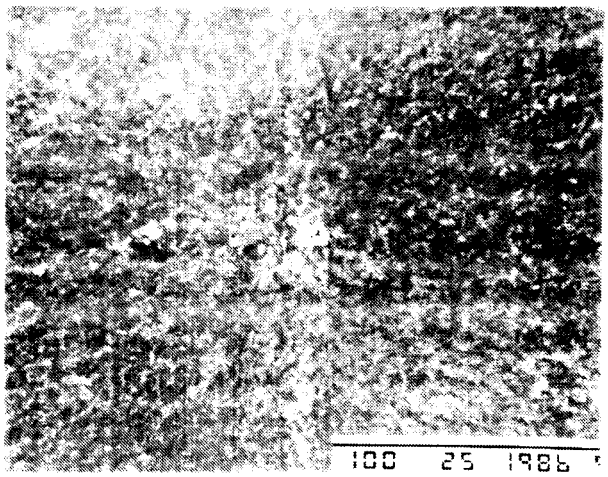	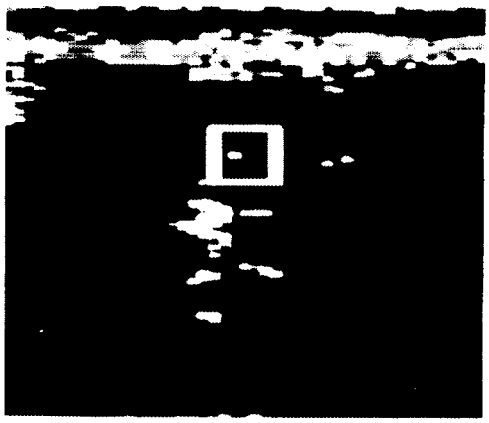

TE87-4381

Specimen No.	SEM	PAM
A31	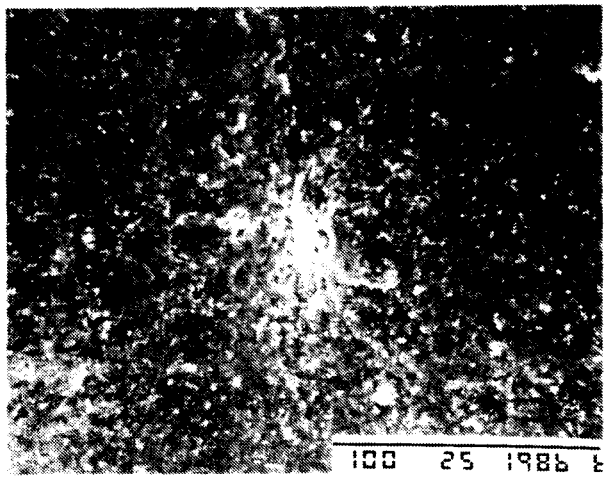	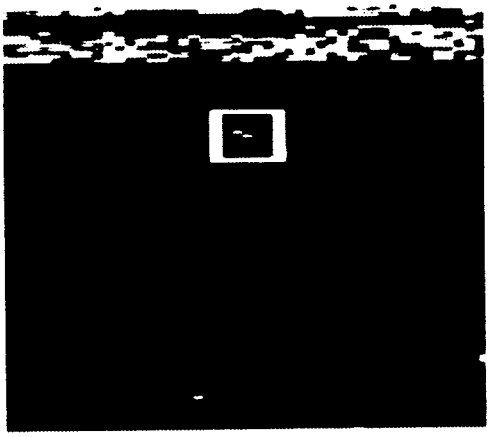
A32	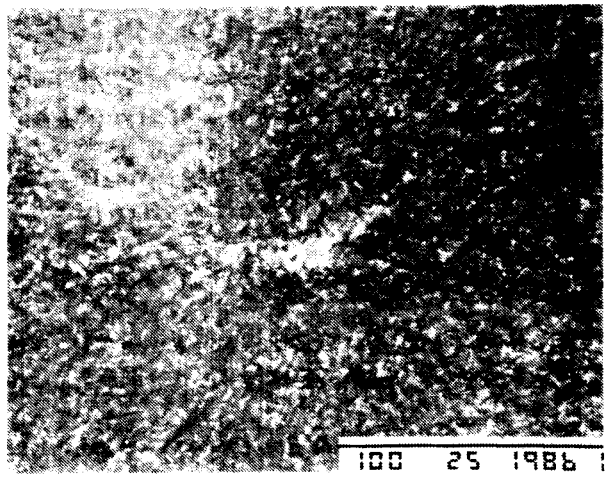	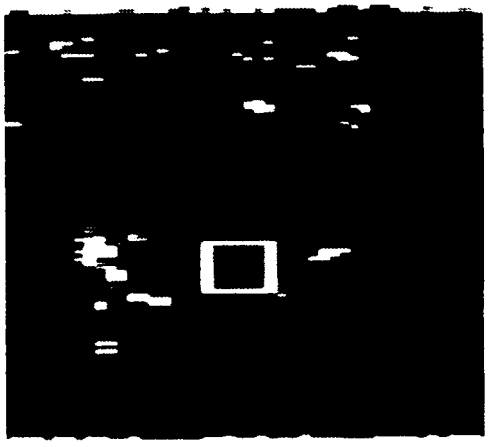
A37	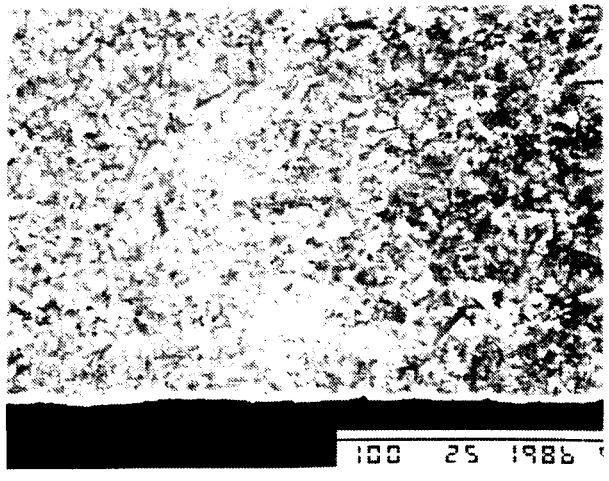	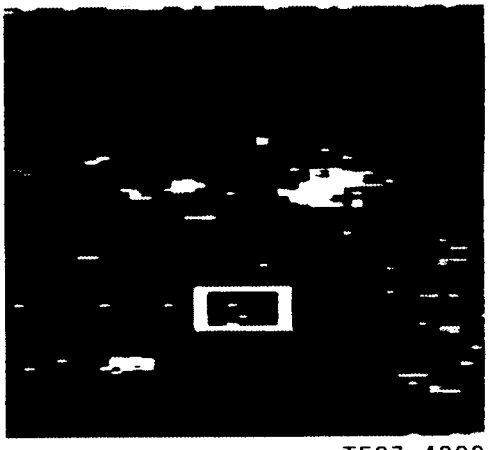

TE87-4382

Specimen No.

SEM

PAM

A38

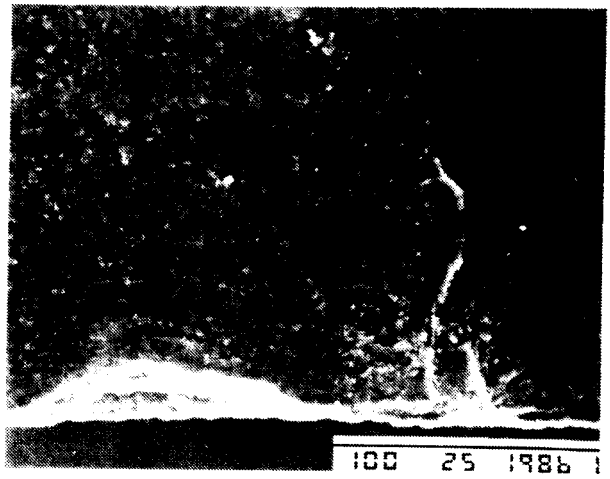

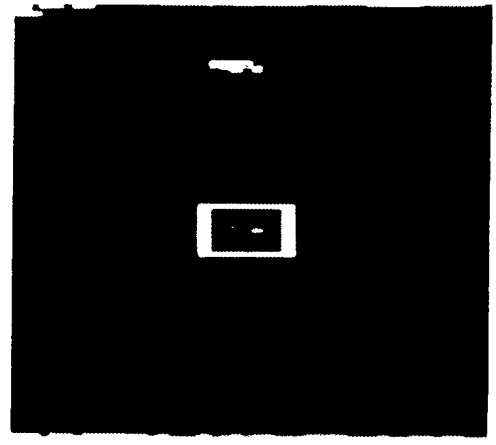

A41

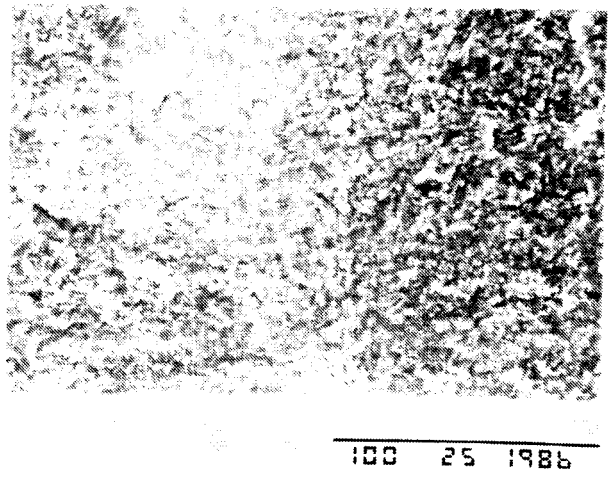

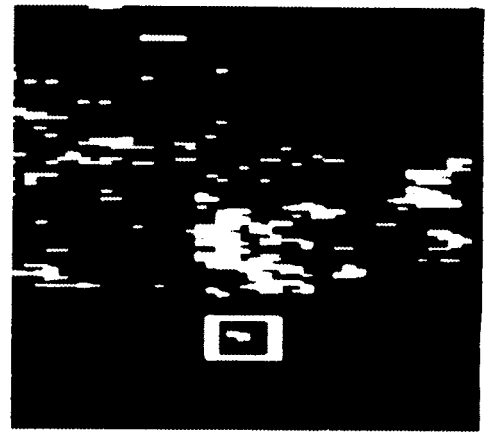

A42

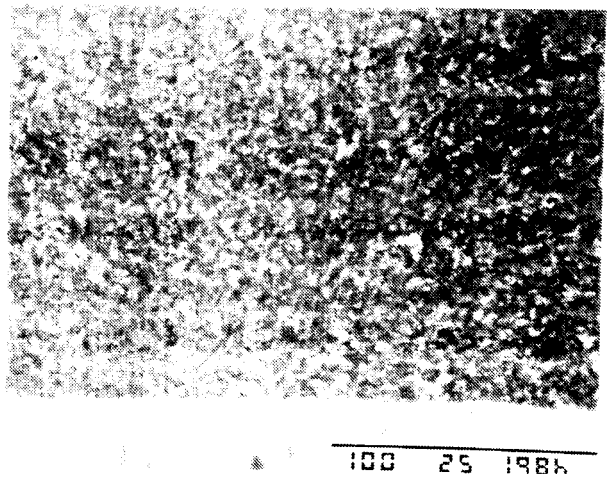

TE87-4383

ORIGINAL PAGE IS
OE POOR QUALITY

Specimen No.	SEM	PAM
A43	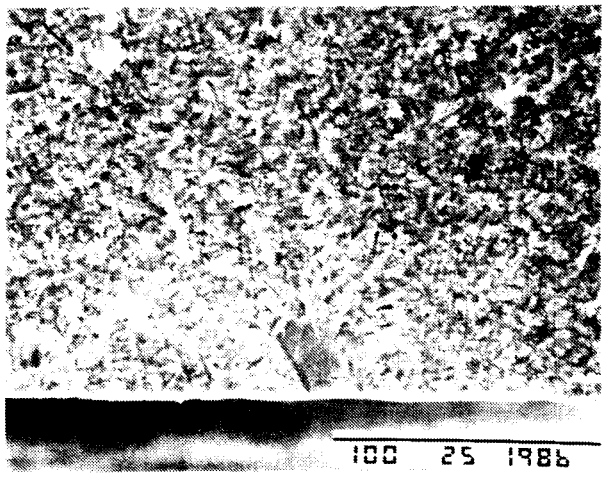	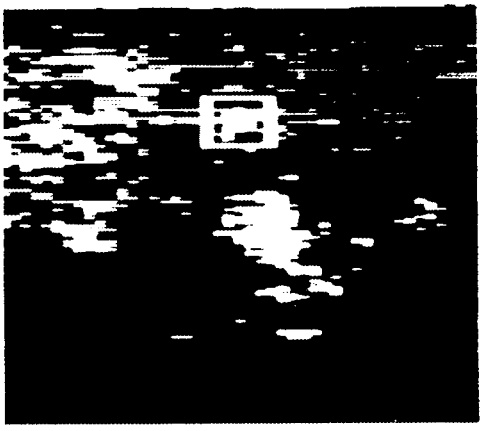
A46	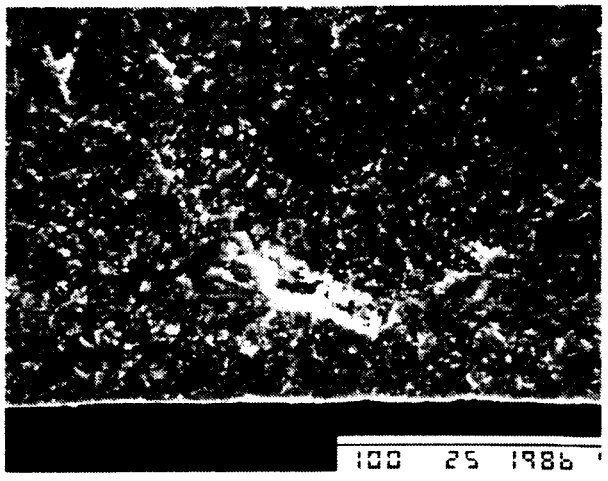	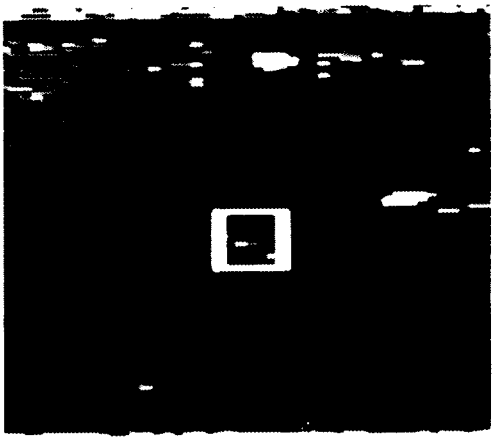
A59	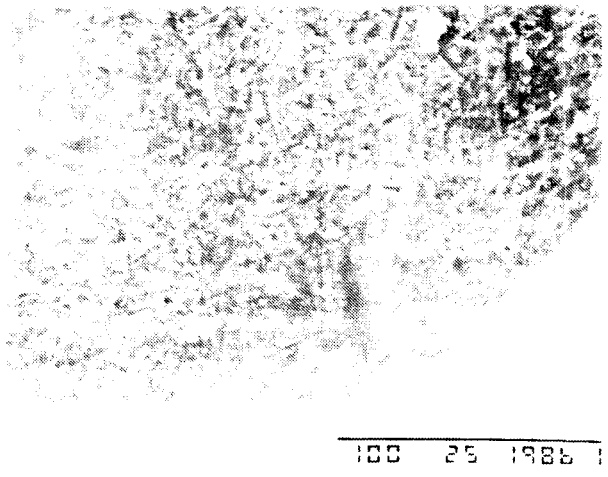	

TE87-4384

DISTRIBUTION LIST

NASA Lewis Research Center
21000 Brookpark Road
Cleveland OH 44135
Attn: A. Vary, MS 6-1
J.P. Gyekenyesi, MS 6-1
S.J. Klima, MS 6-1 (100 copies)
H.E. Kautz, MS 6-1
M.H. Hirschberg, MS 49-7
S.R. Levine, MS 49-3
C.E. Lowell, MS 49-1
H.B. Probst, MS 49-1
R.C. Evans, MS 77-6
R.L. Firestone, MS 500-305
Library, MS 60-3 (2 copies)
Report Control, MS 60-1
Technology Utilization, MS 7-3
Office of Patent Council, MS 301-6

National Aeronautics and Space Administration
Washington DC 20546
Attn: RM/S.L. Venneri
R/L.A. Harris
QP/N.R. Schulze
Library

National Aeronautics and Space Administration
George C. Marshal Space Flight Center
Huntsville AL
Attn: EH13/J.M. Knadler
Library

National Aeronautics and Space Administration
Lyndon B. Johnson Space Center
Houston TX 77058
Attn: Library

National Aeronautics and Space Administration
Langley Research Center
Hampton VA 23365
Attn: J.S. Heyman, MS 231
Library

National Aeronautics and Space Administration
John F. Kennedy Space Center
Kennedy Space Center FL 32899
Attn: SI-PEI-3A/J. Larson
Library

National Aeronautics and Space Administration
Goddard Space Flight Center
Greenbelt MD 20771
Attn: Library

Jet Propulsion Laboratory
4800 Oak Grove Drive
Pasadena CA 91103
Attn: Library

Ames Research Center
Moffett Field CA 94035
Attn: Library

U.S. Air Force
Wright Patterson AFB OH 45433
Attn: D.M. Forney, AFWAL/MLLP
T.D. Cooper, AFWAL/MLSA

Scientific and Technical Information Facility
Box 8757
Baltimore MD 21240
Attn: NASA Representative (6 copies)

EX-Cello-O Compressor Components Corporation
23555 Euclid Avenue
Cleveland OH 44117
Attn: T. Derkacs

U.S. Army Materials Technology Laboratory
Watertown MA 02172-0001
Attn: J.W. McCauley

Oak Ridge National Laboratory
Metals and Ceramics Division
P.O. Box X
Oak Ridge TN 37831
Attn: D.R. Johnson
R.W.McClung

National Bureau of Standards
Gaithersburg MD 29899
Attn: H.T. Yolken

Argonne National Laboratory
Materials and Components Division
9700 South Cass Avenue
Argonne IL 60439
Attn: W.A. Ellingson

Allied-Signal Engineered Materials
50 East Algonquin Road
Des Plaines IL 60017-5016
Attn: D. Yuhas

Norton Company
Advanced Ceramics
Northboro MA 01532-1545
Attn: K.E. Amin

Standard Oil Engineered Materials Company
4440 Warrensiville Center Road
Cleveland OH 44128
Attn: W.D. Friedman

Idaho National Engineering Laboratory
Idaho Falls ID 83415
Attn: L.A. Lott

The Johns Hopkins University
Materials Science and Engineering
Baltimore MD 21218
Attn: R.E. Green, Jr.

GTE Labs., Inc.
40 Sylvan Rd.
Waltham MA 02254
Attn: A. Pasto
Bill Koenigsberg

University of Bridgeport
Dept. of Mechanical Engineering
Bridgeport CT 06602
Attn: M.A. Mahmoud

Massachusetts Institute of Technology
Cambridge MA 02139
Attn: J.H. Williams, Jr.

Martin Mariette Corporation
P.O. Box 179
Denver CO 80201
Attn: W.D. Rummel

Garrett Turbine Engine Company
P.O. Box 5217
111 S. 34th Street
Phoenix AZ 85010
Attn: V.E. Panhuise MS 93-393/503-4Y

Ford Motor Company
Room S2023 Scientific
Dearborn MI 48121
Attn: T. Whalen

Department of Energy
Office of Transportation Systems
Forrestal Bldg.
Washington D.C. 20585
Attn: A.A. Chesnes
R. Schultz

General Electric Company
199 Container Place
Cincinnati OH 45246
Attn: C. Wojciechowski

United Technologies Research Center
Silver Lane
East Hartford CT 06108
Attn: H.I. Ringermacher

Ultran Laboratories Inc.
139R North Gill Street
State College PA 16801
Attn: M.C. Bhardwaj

U.S.Army, AMSTA-RGRT
Warren, MI 48397-5000
Attn: Douglas Rose

Sohio Engineered Materials Co.
Niagara Fall R & D Center
P.O.Box 832
Niagara Falls, N.Y. 14302
Attn: M. Srinivasan